Preparation and Characterization of Cuprous Oxide for Improved Photoelectrochemical Performance

DISSERTATION

zur Erlangung des akademischen Grades
Doktor der Ingenieurwissenschaften
(Dr.-Ing.)

vorgelegt der Fakultät für Elektrotechnik und Informationstechnik
der Technischen Universität Ilmenau

von
M.Sc. Mario Kurniawan

Gutachter:	Herr Univ.-Prof. Dr. rer. nat. habil. Dr. h.c. Andreas Bund *Technische Universität Ilmenau*
	Herr Dr. Joo Yul Lee *Korean Institute of Material Science*
	Herr Univ.-Prof. Dr. rer. nat. habil. Dr. h.c. Peter Schaaf *Technische Universität Ilmenau*

Tag der Einreichung:	03. 09.2021
Tag der wissenschaftlichen Aussprache:	19.04.2022

DOI: 10.22032/dbt.51881
URN: urn:nbn:de:gbv:ilm1-2022000128

Abstract

Photoelectrochemical (PEC) water splitting offers a sustainable and clean alternative method to produce hydrogen without relying on fossil fuels. P-type Cu_2O semiconductor is a promising candidate to be used as a photocathode material with respect to cost, abundance, light absorption, and energy band position. A novel and inexpensive fabrication procedure using solely electrodeposition as presented here to produce a highly porous structure (55 – 80 pores/mm^2) of Cu_2O photocathodes with improved PEC performance. A Three-step procedure was implemented to produce a stable and highly porous Cu metal framework as a substrate to then be coated with the Cu_2O film. In the first step, a dynamic hydrogen-bubble-assisted Cu electrodeposition process was employed to prepare porous Cu structures with delicate pore networks. The porous Cu structures were mechanically reinforced by electrodepositing homogenous and compact Cu layers on the delicate ramified pore walls. As the porous Cu structure was not entirely reinforced, in a third step the reinforced porous layer was detached from the planar Cu substrate using ultrasonication to obtain a stable free-standing porous Cu framework with tubular through-pores networks. The pore size can be easily tuned by changing the deposition time during the first electrodeposition step for the Cu deposition.

Cu_2O films with various thicknesses between ~0.5 and ~3 µm were electrodeposited on the free-standing porous Cu frameworks by varying the deposition time. The PEC water splitting evaluation of the Cu_2O photocathodes was performed under chopped simulated AM 1.5 illumination in an aqueous electrolyte of 0.5 M Na_2SO_4 (pH 6). It was found that the samples with smaller pores exhibited the highest photocurrent of -2.75 mA cm^{-2} at 0 V vs. RHE, followed by -2.25 mA cm $^{-2}$ for large pores samples while maintaining a low dark current. These photocurrents are 120% and 80% higher than the PEC performance of the Cu_2O film on planar Cu substrate that was deposited using the same electrodeposition parameters. The high performance is attributed to the increased surface area from the porous structure, thin and homogenous coverage of the Cu_2O film with small grain size, and higher hole concentrations as was shown by Mott-Schottky analysis.

Further evaluation of the free-standing porous Cu_2O samples reveals that they possess direct optical transmittance between 14% and 23% (λ=400-800 nm) for the small-pores samples and the large-pores samples, respectively. The fabrication of the translucent metal framework using the electrodeposition process has not been reported elsewhere, which can unfold new innovations for different applications, especially in the field of energy materials.

Kurzfassung

Die Photoelektrochemische (PEC) Wasserspaltung stellter eine nachhaltige und saubere Methode dar, um Wasserstoff zu erzeugen, ohne auf fossile Brennstoffe angewiesen zu sein. Der P-Typ Cu_2O-Halbleiter ist ein vielversprechender Kandidat für die Verwendung als Photokathodenmaterial in Bezug auf Kosten, Verfügbarkeit, Lichtabsorption und Energiebandposition. Ein neuartiges und kostengünstiges Herstellungsverfahren für hochporöse Strukturen (55-80 Poren/mm^2) von Cu_2O-Photokathoden mit verbesserter PEC-Leistung unter ausschließlicher Verwendung der elektrochemischen Abscheidung wird vorgestellt. Dieses Verfahren beinhaltet drei Schritte, um ein stabiles und hochporöses Cu-Metallgerüst als Substrat für die Cu_2O-Schichten herzustellen. Im ersten Schritt wurde ein Abscheideprozess unterstützt durch die dynamische Entwicklung von Wasserstoff-Blasen entwickelt, um poröse Cu-Strukturen mit feinen Porennetzwerken herzustellen. Die porösen Cu-Strukturen wurden durch Abscheidung homogener und kompakter Cu-Schichten auf den fein verästelten Porenwänden mechanisch verstärkt. Da die poröse Cu-Struktur nicht vollständig verstärkt war, wurde in einem dritten Schritt die teilweise verstärkte Struktur mit Hilfe von Ultraschall vom planaren Cu-Substrat abgelöst, um ein stabiles freistehendes poröses Netzwerk mit röhrenförmigen Durchgangsporen zu erhalten. Die Porengröße kann durch Veränderung der Abscheidezeit während des ersten Herstellungsschrittes leicht eingestellt werden.

Cu_2O-Schichten mit Dicken zwischen ~0,5 und ~3 µm wurden auf den freistehenden porösen Cu-Schichten durch Variation der Abscheidezeit elektrochemisch hergestellt. Die PEC-Wasserspaltung der Cu_2O-Photokathoden wurde unter gepulser simulierter AM 1,5-Beleuchtung in einem wässrigen Elektrolyten aus 0,5 M Na_2SO_4 (pH 6) untersucht. Es wurde festgestellt, dass die Proben mit kleineren Poren den höchsten Photostrom von -2,75 mA cm^{-2} bei 0 V vs. RHE aufwiesen, gefolgt von -2,25 mA cm^{-2} für die Proben mit großen Poren, während ein niedriger Dunkelstrom beibehalten wurde. Diese Photoströme sind 120 % bzw. 80 % höher als die PEC-Leistung einer Cu_2O-Schicht auf planarem Cu-Substrat, die mit den gleichen Abscheideparametern hergestellt wurde. Die hohe Leistung wird auf die vergrößerte Oberfläche durch die poröse Struktur, die dünne und homogene Bedeckung der Cu_2O-Schicht mit kleiner Korngröße und die höheren Lochkonzentrationen zurückgeführt, wie die Mott-Schottky-Analyse zeigte.

Die weitere Auswertung der freistehenden porösen Cu_2O-Proben zeigte, dass sie eine direkte optische Durchlässigkeit von 14 % für die feinporigen Proben bzw. 23 % für die grobporigen Proben besitzen (λ = 400-800 nm). Die Herstellung des transluzenten Metallgerüsts mit Hilfe des elektrochemischen Abscheidungsprozesses wurde bisher nicht berichtet, sodass neue Innovationen für verschiedene Anwendungen, insbesondere im Bereich der Energiematerialien, ermöglicht werden.

Acknowledgment

During my PhD course, I have the pleasure and opportunity to meet and work with amazing people from different institutes for various research activities and projects. Here, I would like to give my sincere appreciation for their assistance, shared knowledge, and ideas that help me progress in this work. First and foremost, I would like to express my highest gratitude to my supervisor, Prof. Dr. Andreas Bund for allowing me to join his group and permitting me to pursue my PhD on the proposed research topic of photoelectrochemical water splitting. It is a great honor to work in his group and I am really grateful for his guidance and continuous support to make my PhD more pleasant and productive. I am extremely thankful for his precious time to share his expertise and knowledge on the field of electrochemistry which helps me to progress on my PhD topic as well as his valuable assistance to make electronic devices such as a control unit for modulated poor-man LED light source, solar simulator shutter control unit, temperature sensor, and many more. I would like to express my appreciation to Prof. Dr. Peter Schaaf and Dr. Jooyul Lee for reviewing my dissertation and also to all of my doctoral commission committee members.

I would like to give special gratitude to Dr. Michael Stich for providing me with a meaningful and valuable discussion on my PhD topic. His guidance, support, constructive comments, and brilliant ideas help me to progress exponentially with my work, especially for the publications. Next, I would also like to give special gratitude to Mrs. Magali Camargo and Dr. Rolf Grieseler for sharing their expertise and assistance on the material synthesis and characterization as well as their encouraging support and collaboration. I would also like to thank Dr. Ralf Peipmann and Dr. Codruta Vlaic for their time for a meaningful discussion on the topic. I want to express my gratitude to Prof. Dr. Thomas Hannappel for sharing his expertise on semiconductors, and photovoltaic. I would like to give special gratitude to Miss Mayra Marimon, and Mr. Rembert White for their assistance and contribution to this work. I would like to thank all my colleagues, Dr. Adriana Ispas, Dr. Svetlozar Ivanov, Dr. Steffen Link, Dr. Henry Romanus, Dr. Andrea Knauer, Mr. Martin Leimbach, Mr. Mathias Fritz, Dr. Rene Bottcher, Dr. Udo Schmidt, Miss Gisela Lucero, Mrs. Sri Mulyaningsih, Miss Nurul Amanina binti Omar, Mrs. Karin Keller, Mrs. Susan Kiesewetter, Miss Lara Eggert, Mr. David Ostheimer Mr. Thomas Engemann, Miss Anna Endrikat, Mrs. Anke Kais and Mr. Sebastian Mai for their endless encouragement and warm hospitality.

I would also like to give a special thanks to Miss Ardita Erlangga for the emotional support. And most importantly, I would like to give my deepest gratitude to my loving parents, and I would like to dedicate this work to my wonderful deeply missed mother who had always supported me. I also thank the state of Thuringia and TU Ilmenau for the graduate fellowship during my PhD course.

Table of Contents

ABSTRACT I

KURZFASSUNG II

ACKNOWLEDGMENT III

TABLE OF CONTENTS IV

ABBREVIATIONS VI

1 INTRODUCTION 1

2 FUNDAMENTALS AND STATE OF THE ART 5
2.1 ELECTROCHEMICAL CELL 5
2.1.1 WATER ELECTROLYSIS 7
2.2 PHOTOELECTROCHEMICAL CELL FOR WATER SPLITTING. 8
2.3 CUPROUS OXIDE AS PHOTOCATHODE FOR PHOTOELECTROCHEMICAL WATER SPLITTING 15
2.4 ELECTRODEPOSITION OF METAL OXIDES 19
2.5 HYDROGEN-BUBBLES TEMPLATED METAL FOAM 20

3 EXPERIMENTAL PROCEDURE 23
3.1 ELECTROCHEMICAL DEPOSITION OF COPPER 23
3.1.1 FABRICATION OF POROUS CU FRAMEWORK 23
3.1.2 REINFORCEMENT AND SEPARATION PROCEDURE OF THE POROUS CU FRAMEWORK 26
3.2 ELECTRODEPOSITION OF CUPROUS OXIDE IN AN ALKALINE BATH 26
3.2.1 SURFACE FACETS MODIFICATION USING HEXAMETHYLENETETRAMINE AS A CAPPING AGENT. 28
3.3 MATERIAL CHARACTERIZATION 28
3.3.1 MORPHOLOGICAL ANALYSIS 28
3.3.2 COMPOSITION AND STRUCTURAL ANALYSIS 29
3.3.3 OPTICAL CHARACTERIZATION 31
3.3.4 MOTT-SCHOTTKY ANALYSIS 32
3.4 PHOTOELECTROCHEMICAL CHARACTERIZATION 34
3.4.1 PHOTOELECTROCHEMICAL CELL AND SOLAR SIMULATOR CONFIGURATION 34
3.4.2 PHOTOELECTROCHEMICAL ANALYSIS 36

4 RESULTS AND DISCUSSION 37
4.1 DENDRITIC POROUS CU FRAMEWORK 37
4.2 REINFORCED POROUS CU AND FREE-STANDING POROUS CU FRAMEWORK. 42
4.3 ELECTRODEPOSITION OF CU_2O FILM 45
4.3.1 DEPOSITION OF CU_2O FILM ON PLANAR SUBSTRATES 47
4.3.1.1 GROWTH MECHANISM OF THE CU_2O 47
4.3.1.2 THICKNESS EVALUATION OF THE CU_2O FILM 49
4.3.2 CU_2O ON POROUS CU FRAMEWORKS 51
4.4 OPTICAL CHARACTERIZATION OF THE CU_2O ON THE POROUS CU FRAMEWORKS. 59

4.5 DETERMINATION OF FLAT BAND POTENTIAL AND CHARGE CARRIER DENSITY BY MOTT-SCHOTTKY ANALYSIS. 63
4.6 PHOTOELECTROCHEMICAL PERFORMANCES OF THE Cu_2O SAMPLES 65
4.6.1 Cu_2O ON FLAT CU SUBSTRATES 65
4.6.2 Cu_2O ON POROUS CU SUBSTRATES 67

5 CONCLUSION AND PERSPECTIVE 74

REFERENCES 78

LIST OF FIGURES 86

SCIENTIFIC PUBLICATIONS 90

APPENDIX 92

Abbreviations

AFM	Atomic force microscopy
ALD	Atomic layer deposition
AM	Air mass
AZO	Aluminum doped zinc oxide
CB	Conduction band
CV	Cyclic voltammetry
EIS	Electrochemical impedance spectroscopy
FESEM	Field emission scanning electron microscope
FTO	Fluorine doped tin oxide
FWHM	Full width at half maximum
HER	Hydrogen evolution reaction
HMT	Hexamethylenetetramine
IR	Infrared
LSV	Linear sweep voltammetry
MS	Mott-Schottky
NHE	Normal hydrogen electrode
OER	Oxygen evolution reaction
PEC	Photoelectrochemical
PMMA	Poly(methyl methacrylate) or Plexiglass
PV	Photovoltaic
PVDF	Polyvinylidene fluoride
Redox	Reduction and oxidation
RHE	Reversible hydrogen electrode
RTC	Relative texture coefficient
SPEIS	Staircase potentio electrochemical impedance spectroscopy
STH	Solar-to-Hydrogen
TC	Texture coefficient
UV	Ultraviolet
UV-Vis	Ultraviolet-visible spectroscopy
VB	Valence band
XRD	X-ray diffraction

1 Introduction

In today's society, electricity is an essential requirement to meet a variety of daily needs. Most of the global energy supplies come from the burning of fossil fuels such as coal, crude oil, and natural gas to produce electricity. Furthermore, the burning of fossil fuels produces greenhouse gases which are harmful to the environment. This situation has triggered a global challenge to find an alternative energy production that is clean and sustainable.

In recent years, renewable energies have been extensively studied and utilized to reduce the usage of fossil fuels. Among the renewable energies, direct solar energy has the most considerable potential to supply global primary energy demand, which is estimated to be about 1000 EJ per year (2.8×10^{14} kWh) [1]. Solar energy is estimated to have a global energy potential of 1500 – 50000 EJ per year ($4.2 \times 10^{14} - 1.4 \times 10^{16}$ kWh) depending on the insolation (incident solar radiation per unit area over a certain period of time), cloud cover, and land-use constraints including topographic limitations [2]. In general, most solar radiation that reaches the earth's surface is converted into other forms of energy such as thermal energy, electrical energy, and chemical energy. For instance, photovoltaic (PV) cells allow the direct conversion of solar energy into electricity. However, the low conversion efficiency of the commercially available PV cells (14-19% for multi-crystalline silicon solar cells) [3, 4] and the non-continuous supply of sunlight make it difficult to be used as a primary energy source. The converted energy needs to be stored as chemical fuel or electrical charge in a battery to address this issue.

One attractive approach is the use of a photoelectrochemical (PEC) cell for water splitting. In this case, the solar energy is converted directly into a chemical fuel as hydrogen by utilizing semiconductor materials as photo-absorbers and photocatalysts [5]. The light energy is absorbed by the semiconductor and is used to convert water molecules into hydrogen and oxygen. Hydrogen is an energy carrier that can store and deliver a tremendous amount of energy (specific energy density of 33.6 kWh/kg or 120 MJ/kg) which plays a vital role in a clean and sustainable energy system[6]. It is used in a fuel cell to produce electricity, heat, and water. Currently, hydrogen is produced mainly by steam reforming of fossil fuels, specifically natural gas [7]. This process generates an enormous amount of CO_2 (7 kg per 1 kg of H_2)[8] which contributes to greenhouse emissions and causes global warming. Combining an electrochemical process and solar energy to split the water molecules, the PEC cell offers promising potential to produce green hydrogen with zero emission.

The PEC cell for water splitting was first introduced by Fujishima and Honda in 1972 [9]. They used a TiO_2 n-type semiconductor as a photoanode and Pt as a counter electrode. Upon irradiation with UV light, electrons and hole pairs are generated. The photogenerated electrons are driven to the Pt counter electrode to reduce water and form hydrogen. At the same time, the holes are used to oxidize water and produce oxygen at the TiO_2 surface. An additional external bias is applied to compensate for the potential deficiency of the cell which needs to reach more than 1.23 V to generate water splitting. Due to the large bandgap of the TiO_2 semiconductor, the solar-to-hydrogen (STH) efficiency is relatively low and could not go beyond 1%. Since then, extensive studies have been similarly conducted on other semiconductor materials to achieve higher efficiency [10–12]. However, the development of stable and highly efficient materials for PEC water splitting is still very challenging. Several factors such as the cost of the materials, and ease of fabrication to produce at a large industrial scale limit the material selection. However, copper-based semiconductors such as copper oxide fit these criteria for the PEC water splitting. It is abundant and can be synthesized by industrially scalable low-cost production methods such as electrodeposition.

Among the different copper oxides, cuprous oxide (Cu_2O) shows promising potential to be used as a photocathode to generate hydrogen. It is a p-type semiconductor with a direct band gap of ~2 eV, which provides good light absorption in the visible range, and possesses a favorable band position that straddles the hydrogen and oxygen redox potential. Based on its band gap, the theoretical value for the STH conversion efficiency can reach a maximum of ~18 % with a photocurrent of about -14.7 mA cm^{-2} [13, 14]. However, in practical application, this value is far from being realized. There are two main challenges such as inadequate diffusion length of the minority charge carriers toward its absorption coefficient [15, 16] and poor chemical stability in the aqueous solutions due to the reduction potential of the Cu_2O to Cu that lies at 0.46 V vs. RHE [17, 18]. The issue on the chemical stability was effectively resolved by adding a homogenous and thin (<100 nm) protective layer (e.g., TiO_2, ZnO, Al_2O_3, graphite, graphitic carbon nitride, etc.) using atomic layer deposition (ALD) [19–24].

However, the other challenge, which involves an inefficient collection of the photogenerated carriers, still has much room for improvement. One approach to address this issue is by modifying the morphology of the Cu_2O photocathodes. The surface of the Cu_2O can be structured so that the thin Cu_2O layer is positioned at a more beneficial angle towards the incoming light or the photon pathway to significantly increase the light absorption while still maintaining a short electron diffusion length to the electrolyte. This can be practically achieved by synthesizing vertically aligned nanowire structures or by the approach pursued in this thesis, Cu_2O coated pore walls (Figure 1–1). Furthermore, the modified structure increases the surface area tremendously, leading to a higher exposure of the photoactive sites, accelerating the chemical reactions [25, 26].

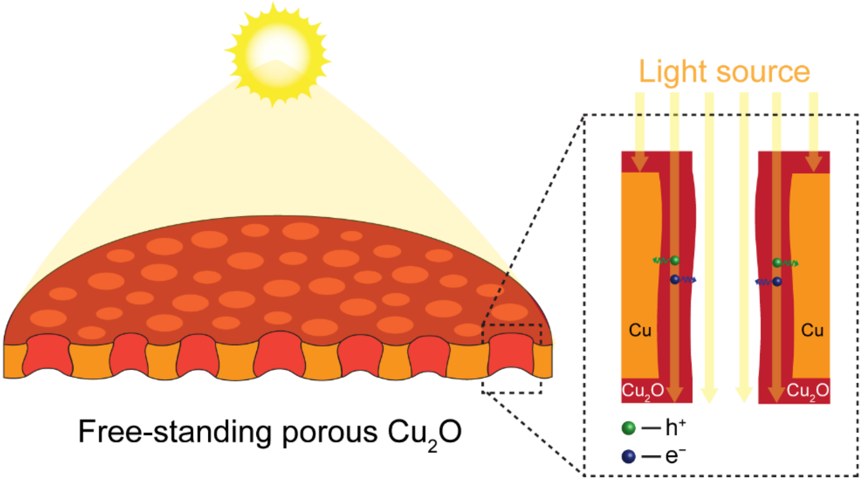

Figure 1–1 Schematic representation of the enhanced light absorption with the short electron diffusion length to the surface of the Cu_2O coated pore wall structure.

Though the Cu_2O nanowire structure shows a promising concept to enhance the efficiency, several attempts using the nanowire structure [22, 27, 28] have failed to deliver higher PEC performance than the compact planar film, as was reported by Paracchino et al. [17]. The low PEC performance of the nanowire structure is caused by some challenges such as maintaining material quality and inhomogeneous Cu_2O coating which exposes the metallic substrate to the electrolyte. A report by Luo et al. [29] shows that the Cu_2O made by using wet chemistry and thermal annealing process on Cu substrate has low PEC performance due to the inhomogeneous Cu_2O layer and the exposed underlying Cu metal. This problem was resolved by coating a thin Cu_2O film on the exposed Cu metal using the electrodeposition method, which significantly improved the PEC performance. The electrochemical deposition method, an inexpensive and easily scalable fabrication process, can produce a more homogenous Cu_2O film with reliably high PEC performance. Moreover, it can also be implemented on rough or 3D porous substrates with easily controllable film thickness by adjusting the deposition parameters.

The main objective of this thesis is to achieve high PEC performance of the Cu_2O photocathodes by enhancing the active surface area using a highly porous Cu framework. Several reports suggest that various materials can be deposited on the Cu_2O film as a buffer layer, a protective layer, and metal electrocatalysts such as Pt [17] or Ru[29] to enhance the PEC performance as well as the chemical stability. However, the plethora of these different materials and processes makes a fair comparison of the underlying Cu_2O performance very difficult. The bare Cu_2O itself plays a significant role as the light absorber and must be adequately optimized to improve the PEC performance which will be discussed in section 4.6.

2 Fundamentals and State of the Art

2.1 Electrochemical cell

An electrochemical cell consists of two metallic electrodes immersed in an electrolyte where an electric current is being generated or used to drive a chemical reaction. Electrochemical cells are classified into two types, a galvanic cell[1] , and an electrolytic cell[2]. Two main reactions are occurring in an electrochemical cell, the oxidation and reduction reactions. The oxidation reaction refers to the process where a species loses electrons, whereas the reduction reaction corresponds to the opposite: the gaining of electrons. Redox reactions occur when there is a transfer of an electron between chemical species where one species go through an oxidation reaction while another species undergoes a reduction reaction. In an electrolytic cell, the oxidation reaction occurs at the anode, while the reduction reaction occurs at the cathode.

The standard cell potential (E^o_{cell}) can be derived from the difference between the reduction potential of the cathode (E^o_{red}) and the oxidation potential of the anode (E^o_{oxid}) performed at standard conditions (all species in their standard states), shown in Eq. 1.

$$E^o_{cell} = E^o_{red} - E^o_{oxid} \tag{1}$$

The cell potential at non-standard conditions can be determined by using the Nernst equation (Eq. 4). The Nernst equation is derived from the change of the Gibbs free energy (ΔG) as a function of the electrochemical cell potential (Eq.2).

$$\Delta G = -nFE \tag{2}$$

In this case, n is the number of electrons transferred in the reaction, F is the Faraday constant (96500 C mol^{-1}), and E is the cell potential. The Gibbs free energy is a measure of the maximum reversible work that may be performed by a thermodynamic system during a chemical process at constant temperature and pressure. It can be used to determine the nature of chemical reactions occurring in the electrochemical cell. When the $\Delta G < 0$, the cell trigger a spontaneous reaction (exergonic) which means that the chemical energy is converted into electrical energy. In contrast, when the $\Delta G > 0$, the cell reactions are classified as non-spontaneous (endergonic). In this case, the reaction

---

[1] A device which generates an electric current due to the difference in the electrochemical potentials of the electrode

[2] A device which uses externally supplied electric current to drive a chemical reaction that otherwise would not occur spontaneously.

consumes work which means that the cell requires an external energy source to trigger the chemical reactions. Under the standard conditions, the cell potential (E) is replaced by the standard potential (E^{o}_{cell}) and ΔG becomes ΔG^{o}. From thermodynamics, the relation between ΔG^{o} and ΔG is written as in Eq. 3.

$$\Delta G = \Delta G^{o} + RT \ln Q \qquad 3$$

Then by substituting Eq. 2 to Eq. 3, the Nernst equation can be written as follows:

$$E = E^{o} - \frac{RT}{nF} \ln Q \qquad 4$$

Where R is the gas constant, T is the absolute temperature in Kelvin and Q is the reaction quotient which is defined as the ratio of the activities or the molar concentration of the product species (reduced species) over the reactant's species (oxidized species) with relation to the power of its stoichiometric constant. The Nernst equation can be used to determine the reaction equilibrium constants and the concentration potentials.

In the electrochemical cell, the energy losses due to the energy conversion process need to be considered. The energy losses are described as follows:

- Ohmic losses; this is caused by the internal resistance of the cell (R_{ohm}), which includes the ionic resistance of the electrolyte, the electronic resistance of the active material, the internal resistance of the current collector, and lastly, the contact resistance between the active material and the current collector.
- Polarization losses; The polarization losses are classified into two types which are activation and concentration polarizations. The activation polarization is a voltage overpotential that is required to overcome the activation energy of the electrochemical reaction on the electrode surface. The concentration polarization involves depletion of the charge carriers or concentration differences between the reactants and products at the electrode surface. The losses due to the concentration polarization can also be influenced by the gas bubble formations.

These losses can then be accumulated, which contribute to the overall overpotential of the system.

2.1.1 Water electrolysis

Water electrolysis is the process where two metal electrodes are immersed in an aqueous electrolyte to split water molecules into hydrogen and oxygen by using electricity as an external energy source. The chemical reaction is depicted in Eq. 5:

$$H_2O \rightarrow H_2 + \frac{1}{2}O_2 \tag{5}$$

When the electricity is applied across the cell, the water is oxidized at the anode, producing oxygen, electrons, and protons. The protons then migrate to the cathode, where they will be reduced to hydrogen. At standard conditions, 237.22 kJ mol^{-1} of the Gibbs free energy is required for the water electrolysis[30]. Using Eq. 2 with n = 2 (the number of electrons exchanged during the process), the thermodynamic cell potential for water electrolysis is calculated to be 1.23 V. This cell potential is independent of the pH. The pH influences only the half-reaction potentials at each electrode (E_{ox} or E_{red}) which according to the Nernst equation at 298 K, are shifted by 0.059 mV for one pH change. In acidic media (pH 0), the chemical reactions at the anode and cathode are described in Eqs 6 and 7.

Anode: $H_2O \rightarrow \frac{1}{2}O_2 + 2H^+ + 2e^-$ $\quad E^o_{ox} = 1.23\ \text{V vs. NHE}$ (6)

Cathode: $2H^+ + 2e^- \rightarrow H_2$ $\quad E^o_{red} = 0\ \text{V vs. NHE}$ (7)

While in the alkaline media (pH 14), the reaction is written in Eqs 8 and 9.

Anode: $2OH^- \rightarrow H_2O + \frac{1}{2}O_2 + 2e^-$ $\quad E^o_{ox} = 0.39\ \text{V vs. NHE}$ (8)

Cathode: $2H_2O + 2e^- \rightarrow 2OH^- + H_2$ $\quad E^o_{red} = -0.84\ \text{V vs. NHE}$ (9)

The HER process can be further elaborated in three main steps (Volmer, Heyrovsky, and Tafel). In acidic media, based on the Volmer electrochemical reaction, HER activity is triggered by the formation of hydrogen adsorption (H_{ad}) from the reduction of protons (Eq 10).

Volmer step (acidic): $H^+ + e^- \rightarrow H_{ad}$ (10)

Heyrovsky step (acidic): $H^+ + e^- + H_{ad} \rightarrow H_2(g)$ (11)

Tafel step (acidic or alkaline): $2H_{ad} \rightarrow H_2(g)$ (12)

In alkaline solution, due to the lack of the protons the electrochemical reaction is mainly based on the reduction of the water molecules (Eq. 13).

Volmer step (alkaline): $$H_2O + e^- \rightarrow OH^- + H_{ad} \tag{13}$$

Heyrovsky step (alkaline): $$H_2O + e^- + H_{ad} \rightarrow OH^- + H_2(g) \tag{14}$$

It has been reported that the reaction rate for the HER in acidic solution is two or three orders of magnitude times higher than that in alkaline solutions [31]. Some factors such as large mass variation between protons and water molecules as well as their different molecular charge can influence the mass transport to the electrode surface and thus contribute to the different reaction rates for the HER.

Although it is preferable to use an acidic solution to generate more hydrogen bubbles due to higher kinetics, the chemical stability of the electrode needs to be also considered. For instance, metal oxides based electrode like copper oxide will be dissolved in a low pH solution range from 0 to 3 [32]. This shows that selecting a suitable pH is important to sustain the chemical stability of the electrode in the electrolyte. In this work, the electrolyte for the PEC water splitting experiment is set at pH 6 to ensure decent electrochemical kinetics and at the same time to maintain good chemical stability of the Cu_2O photoelectrode.

2.2 Photoelectrochemical cell for water splitting.

A photoelectrochemical (PEC) cell is a special case of an electrochemical cell that utilizes a photoactive material for at least one of its working electrodes[30]. It is a device to convert solar energy into chemical fuel such as hydrogen through an electrochemical process. P-type and n-type semiconductors can be used as photocathodes and photoanodes, respectively[33]. One essential requirement for a semiconductor material to be used efficiently for the solar water splitting application is its band energy position. The bandgap of a single junction semiconductor must overlap the potential for water oxidation and water reduction. In other words, the conduction band (CB) edge of the semiconductor must be more negative than the water reduction potential of 0V vs. NHE at pH 0, and the valence band (VB) edge must be more positive than the water oxidation potential of 1.23 V vs. NHE at pH 0.

The semiconductor/electrolyte junction interface significantly influences the PEC water splitting reaction activity[34]. The Fermi level energy in semiconductors corresponds to the electrochemical potential of electrons. On the other hand, the Fermi level of the electrolytes is represented by the redox potential of the redox couples. For an n-type semiconductor, the Fermi level is normally located near the conduction band due to the excess of electrons. In contrast, for the p-type semiconductor, the Fermi level is located near the valence band because of the fewer electrons and higher number of holes. When a semiconductor is immersed in the electrolyte, charge transfer will occur at the semiconductor/electrolyte interface until the Fermi level of the semiconductor has reached an equilibrium with the redox potential of the electrolyte [5]. During this process, the majority charge carrier at the space charge region of the semiconductor will be depleted and thus causes band bending at the semiconductor/electrolyte junction interface (Figure 2–1). Depending on the majority charge carrier (electrons or holes), the semiconductor band energy can have either an upward or downward bending at the semiconductor/electrolyte junction [35].

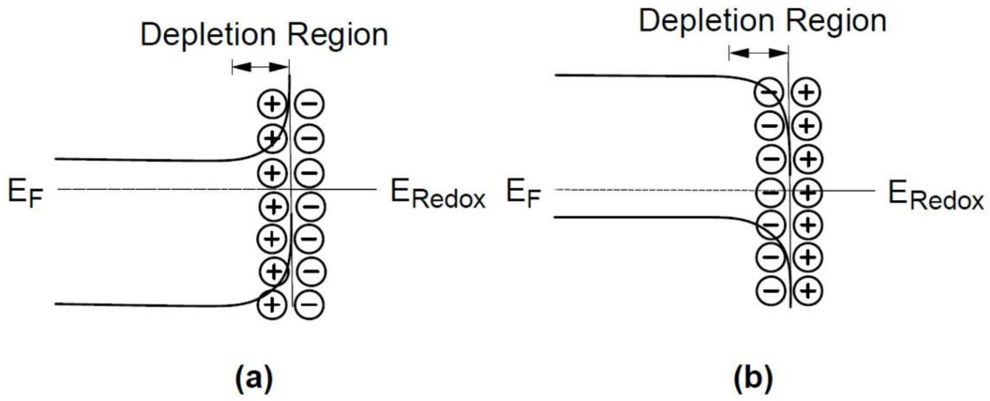

Figure 2–1 Upward band bending of a) n-type semiconductor and downward band bending of b) p-type semiconductor in equilibrium with electrolyte without illumination[36].

For the n-type semiconductor, the depletion of the electrons as the majority charge carrier leaves behind holes at the space charge region and thus creates an upward band bending at the semiconductor/electrolyte interface (Figure 2–1a). In contrast, the p-type semiconductor with positively charged holes as the majority charge carrier will have a downward band bending at the interface (Figure 2–1b). The different charges at the space charge region influence the attraction of the ions in the electrolyte to the surface and the attraction of the ionic layers (Figure 2–1). These ionic layers or so-called electrical double layers are usually formed by the absorbed ions on the surface via chemical interaction, or surface charge called the Helmholtz layer and followed by the ions attracted via coulomb force to make a diffuse layer known as the Gouy-Chapman layer. The positively charged surface of the n-type semiconductor will attract mostly the negatively charged hydroxide ions, which are used to facilitate the water oxidation reaction. In contrast, the negatively charged surface of the p-type semiconductor attracts more positively charged protons that will drive the water reduction at the surface [36–38].

When the semiconductor is illuminated, separation of the charge carriers occurs and causes a change in the Fermi level of the semiconductor. Photon energy that exceeds the semiconductor's band gap excites the electron (e^-) from the VB to a higher energy state or CB, leaving behind an electron vacancy that is positively charged, called hole (h^+). In the case of the n-type semiconductor or photoanode, the increasing number of photogenerated holes due to the incident light oxidizes the water and produces oxygen and electrons. The electrons can be transferred to the counter electrode with a small external bias and trigger the hydrogen evolution reaction (HER). This reaction is reversed for the p-type semiconductor or photocathode. The photogenerated electrons are used to trigger the HER, and at the same time, the holes are transferred to the counter electrode to drive the oxygen evolution reaction (OER).

The PEC cell typically belongs to one of the three configuration categories (Figure 2–2). The cell can be arranged with a single photoanode, a single photocathode, or a tandem system that utilizes both the photoanode and photocathode in the so-called Z-scheme, which is inspired by the mechanism of the natural photosynthesis in green plants [39]. In a single photoelectrode system, a photoanode or photocathode is typically coupled with a noble metal counter electrode. An additional external bias must be applied to reach the thermodynamic potential and, at the same time, create the charge separation between the working and counter electrode.

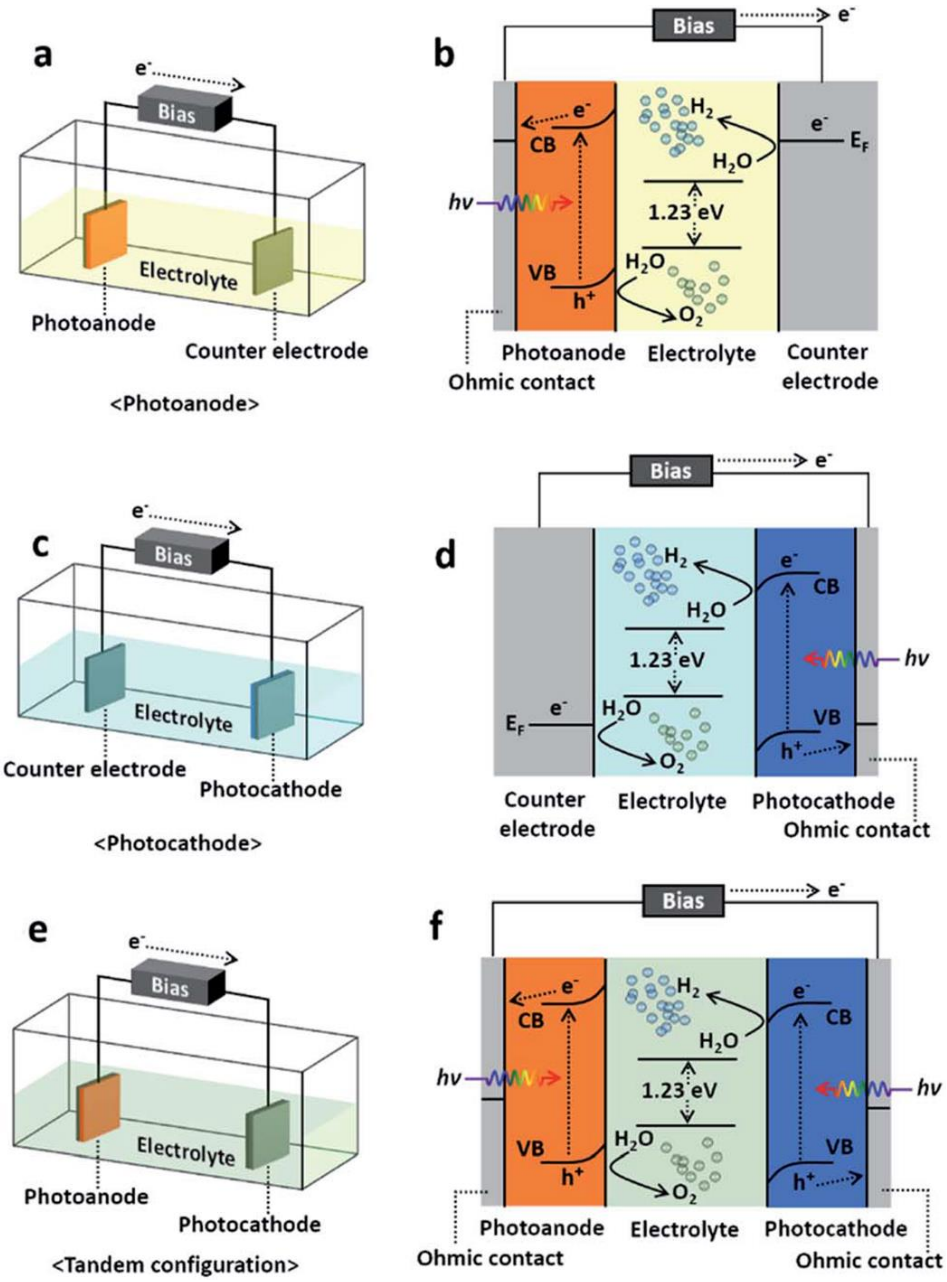

Figure 2–2 Illustration of PEC cell configuration using a) a single photoanode, c) a single photocathode, and e) tandem configuration (Z-scheme). The energy band diagram with the detailed mechanism of each configuration is presented in b), d), and f). [40]

In general, the photovoltage in a semiconductor is generated due to the separation of the electron and holes during illumination, which causes the initial Fermi level of the semiconductor to split into two separate quasi-Fermi levels with different charges (Figure 2–3). The achievable maximum photovoltage is determined by the size of the bandgap and the efficiency of the charge separation [41]. In theory, the maximum photovoltage that a single semiconductor can produce is approximately 400 mV less than its optical bandgap [42]. It means that to perform water electrolysis efficiently, a semiconductor must theoretically possess a bandgap of more than ~1.6 eV to overcome the energy losses in the semiconductor and split water.

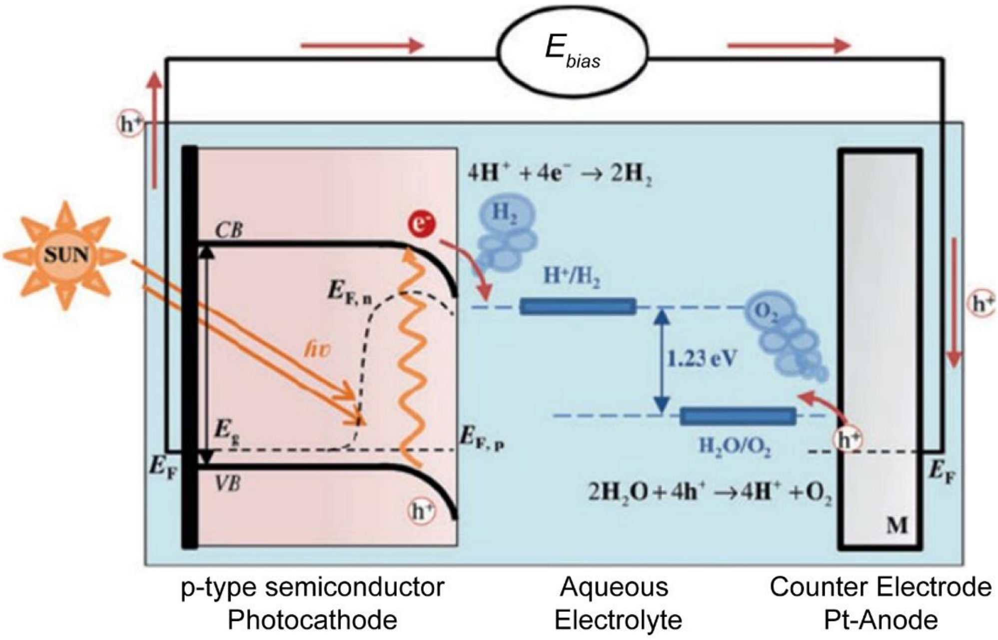

Figure 2–3 Illustration of the PEC cell based on a p-type semiconductor as a photocathode and a metal Pt anode under light illumination. $E_{f,p}$, *and* $E_{f,n}$ *represent the quasi-Fermi level of holes and electrons, respectively. This image is taken from reference*[43].

The theoretical maximum photocurrent density and the solar-to-hydrogen (STH) efficiency is constrained by the size of the optical bandgap of the semiconductor, as presented in Figure 2–4. Based on the data from the National renewable energy laboratory, natural sunlight consists of ~52% of infrared radiation (0.5-1.77 eV), ~43% of the visible spectrum (1.77-3.1 eV), and 5% of UV (3.1-4.13 eV). The semiconductors with a narrower bandgap (<1.5 eV) absorb more photons from the solar spectrum but the photovoltage may not be sufficient to split water efficiently. On the other hand, the wider bandgap semiconductors can generate large photovoltage to split water efficiently but have a lower maximal theoretical STH[44] due to the low absorption of the photons. For instance, well-studied semiconductors, such as TiO_2 and WO_3, have relatively wide bandgap energies of ~3 and ~2.7 eV (Figure 2–5), respectively, which can only absorb a small amount of UV light from the solar spectrum, thus limiting the maximum achievable STH efficiency to 1% and 6% (Figure 2–4).

Some reports suggest that the STH efficiency must reach at least 10% by the PEC cell to meet the technical and economic feasibility for the practical industrial application, which corresponds to a photocurrent density of 8.1 mA cm^{-2} and a bandgap of 2.36 eV[45]. This condition makes selecting an appropriate semiconductor material with a suitable bandgap and band position even more crucial to achieve the 10% STH efficiency for the PEC water splitting application. Another key factor that needs to be considered is the cost for the synthesis and material of the semiconductor. Complex fabrication processes via high-end technology methods and expensive materials can significantly drive up the PEC cell production cost.

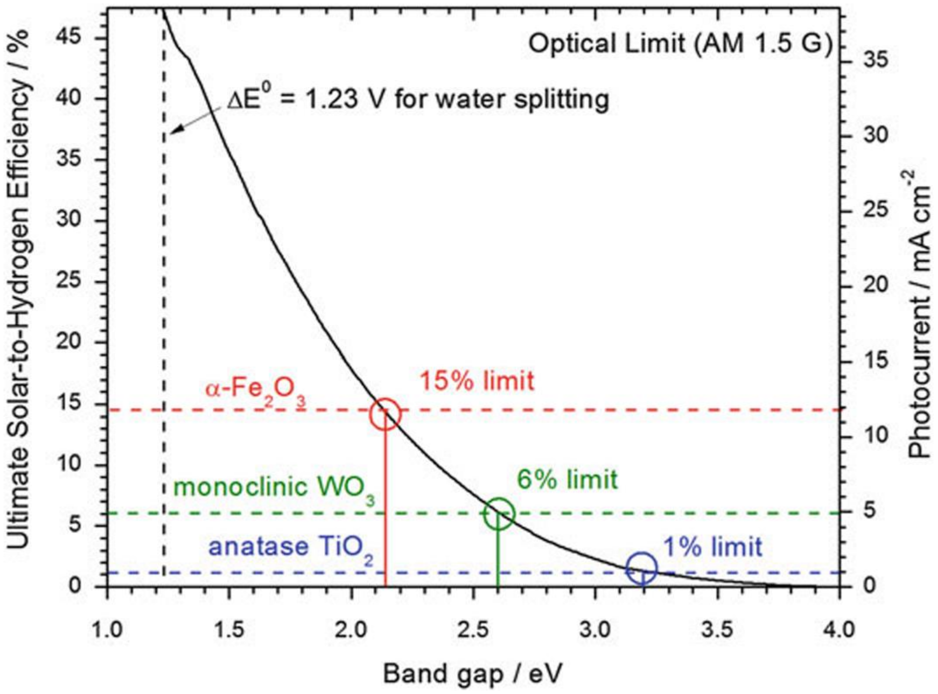

Figure 2–4 Theoretical value of the maximum achievable solar-to-hydrogen (STH) efficiency and the photocurrent as a function of the semiconductor bandgap[46]*. The photocurrent was calculated under the assumption that the solar conversion has no additional efficiency loss.*

Several metal-oxide semiconductors (Figure 2–5) show promising potential because they satisfy most of the requirements mentioned above, such as low cost, and have an appropriate bandgap energy to produce a theoretical photocurrent density of >10 mA cm^{-2}. One of the potential candidates is hematite Fe_2O_3 (n-type, bandgap: ~2.2 eV). It is extensively used as a photoanode because it is cheap, chemically stable, and has a suitable bandgap for visible light absorption. However, the Fermi level of Fe_2O_3 is located near the water redox potential, which influences the degree of the band bending and the absorbed ions on the surface at different pH. Moreover, the conduction band edge is positioned more positive than the water reduction potential of 0 V vs. NHE, making it difficult to trigger complete water splitting reaction without applying a large cathodic potential at the counter electrode to assist the HER[47]. This limitation inhibits the further development of the hematite Fe_2O_3 material to improve the PEC water splitting performance.

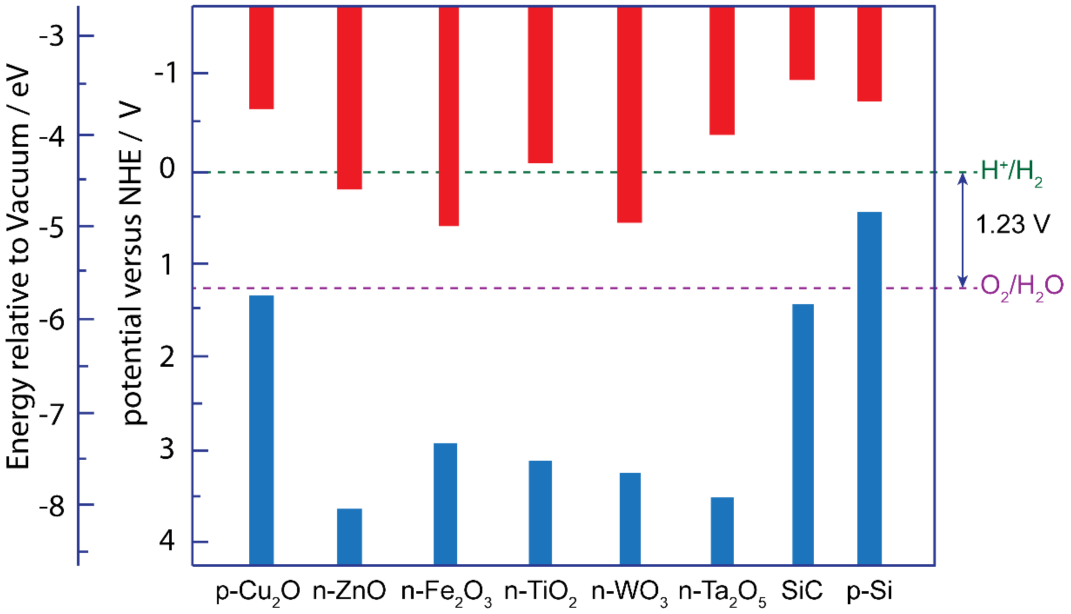

Figure 2–5 Band edge positions of various semiconductors for PEC water splitting application at pH 0. The blue and red bar represents the VB and the CB of the semiconductor, respectively. The data was adapted from reference[48].

Another promising candidate is Cu_2O (p-type, ~2 eV)[49] which has a proper bandgap for visible light absorption and a suitable band edge position for the PEC water splitting application. The theoretical photocurrent for Cu_2O was estimated to reach 14.7 mA cm^{-2} with an STH efficiency of 18 % for an AM1.5 G solar spectrum. One of the drawbacks of Cu_2O as a photocathode is its limited chemical stability under cathodic potential in an aqueous electrolyte. The reduction potential of Cu_2O to Cu metal lies within the bandgap at 0.46 V vs. NHE at pH 0, which causes the Cu_2O to be reduced to Cu metal in the presence of hydrogen evolution. To overcome this drawback, the Cu_2O is usually coated with a thin layer of a highly stable n-type semiconductor (typically TiO_2) to prevent direct contact of the Cu_2O surface to the electrolyte and at the same time facilitate the transport of the minority charge carriers to the semiconductor/ electrolyte interface.

In general, even with an appropriate bandgap and band position, the semiconductors mentioned above could not achieve the maximal theoretical STH efficiency and photocurrent density in a practical application. The metal-oxide-based semiconductors typically are prone to crystallographic disorder, which can influence the electronic properties and causes limitations such as low-charge carrier mobility, short diffusion length with low charge carrier lifetime, and high recombination states. An attempt to solve this issue is by producing nanostructured or highly oriented layers with high crystalline quality.

The use of vertically oriented nanowire structures, for instance, can overcome the short charge diffusion length by utilizing the thin diameter of the nanowire to bring the electron quickly to the electrode surface and thus avoid the non-radiative recombination in the bulk. Moreover, the geometry of the vertically aligned nanowire structure can also increase the light absorption by aligning the angle of the incident light in parallel to the nanowire. A nanowire structure with consistent crystalline quality has been reported to have improved the PEC performance [50, 51]. Another approach to enhance the PEC performance involves tuning the crystalline facet to make it more favorable for the absorption of the ionic species. Hence, the highly oriented crystalline film layer can lower the overpotential and improve the overall kinetics of the system [52]. The impact of the structural modification and the crystal facets of the semiconductor on the PEC performance will be further discussed in chapter 4.6.

Besides the semiconductors mentioned above, recently mixed metal oxides semiconductors such as $BiVO_4$ (n-type, bandgap:~2.4 eV)[53], $CuWO_4$ (n-type, bandgap:~2.2 eV)[54], $CaFe_2O_4$(p-type, bandgap:~1.9 eV)[55], $ZnFe_2O_4$ (n-type, bandgap:~2 eV)[56], $CuFeO_2$ (p-type, bandgap:~1.5 eV)[57] also have gained much attention and interest due to the size of their bandgap, which is mostly around ~2 eV, high chemical stability and their low material costs. The bandgaps of these mixed metal oxide semiconductors are located in a favorable position to be used as either a photocathode or a photoanode. However, these materials have high processing costs, and maintaining high crystalline quality with desired surface morphology is rather challenging [44].

2.3 Cuprous oxide as photocathode for photoelectrochemical water splitting

Cu_2O semiconductor has attracted much attention in recent years due to their low cost, abundance, and advantageous bandgap energy for optoelectronic applications. Cu_2O has a cubic crystalline structure with a lattice constant of ~4.27 Å. In a unit cell, the oxygen atoms are positioned at the center and the corners of the cubic lattice, whereas the four copper atoms lie in a tetrahedron position at the center of the cubic, (Figure 2–6a). The Cu_2O lattice belongs to the space group of Pn3m, incorporating a full octahedral symmetry[58].

Cu_2O is a p-type semiconductor with a direct theoretical bandgap of 2.17 eV. The p-type conduction comes from the presence of excess holes in the valence band due to cation deficiencies which are accommodated mostly by Cu vacancies[59–61]. Cu_2O possesses hole mobility of ~100 $cm^2\ V^{-1}\ s^{-1}$ in a high-quality single crystal[62], which is higher than the other metal oxide semiconductors. The mobility and the hole concentration vary depending on the fabrication process and the crystalline quality. Depending on the crystalline quality, the conduction band edge of Cu_2O is located between -0.7 and -1.1 V vs. NHE at pH 0 [13, 63, 64]. Moreover, the bandgap of Cu_2O varies between 1.9 eV and 2.2 eV, which allows for visible light absorption ranging between ~600 nm and above [65, 66].

Cu_2O can be synthesized using sputtering[67], atomic layer deposition (ALD)[68], sol-gel[69], chemical vapor deposition[70], thermal oxidation of copper[71], wet chemical synthesis[72], and electrodeposition[73, 74]. Electrodeposition stood up as one of the most attractive techniques among these methods due to its cost-effectiveness and scalability for industrial purposes. Furthermore, the electrodeposition techniques can be implemented to homogenously coat a thin layer of active material on complex or 3D substrates and easily tune the surface morphology, such as the crystallite size and shape, by varying the deposition parameters like pH, temperature, and the applied current or voltage. So far, the best result for Cu_2O films on planar substrates for PEC water splitting was fabricated using electrodeposition methods. Paracchino et al. show that electrodeposited Cu_2O on an Au coated FTO substrate in an alkaline bath can generate a photocurrent of -2.4 mA cm^{-2} at 0 V vs. NHE under solar AM 1.5 illumination (100 mW cm^{-2})[17]. One of the reasons for this high achievement is the crystalline orientation of the Cu_2O, which is dominated by the [111] crystal orientation exposing highly catalytic polar {100} facets[17, 75].

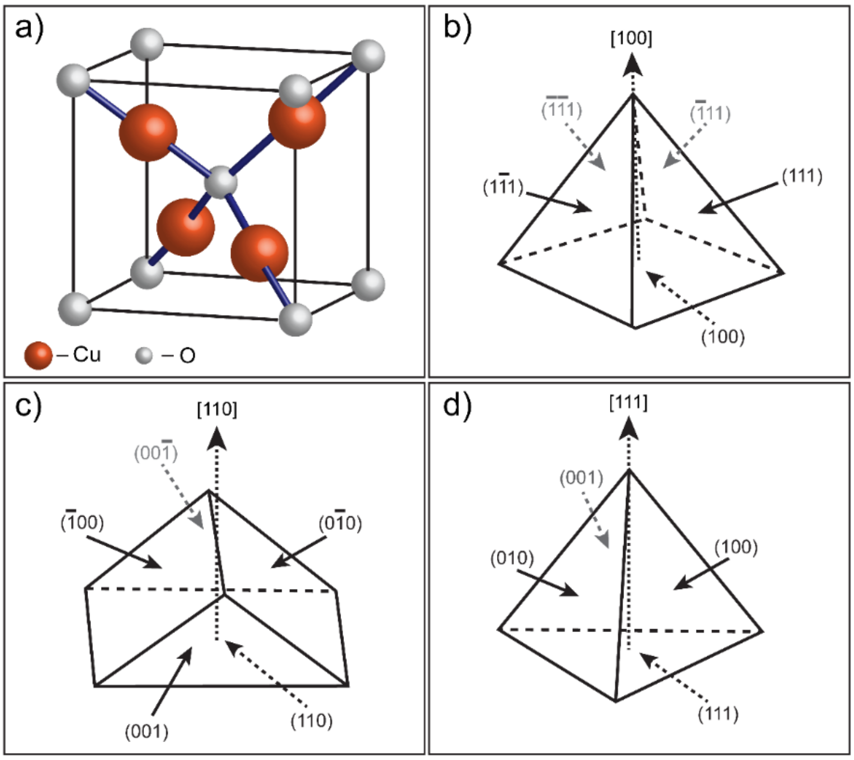

Figure 2–6 a) Crystal structure of Cu_2O in a single unit cell. Various crystalline shapes of the electrodeposited Cu_2O with different crystal orientations: b) [100]-oriented, c) [110]-oriented, and d) [111]-oriented. The figures were reconstructed according to the reference [76]*.*

The growth direction and crystalline shape of the Cu_2O can be controlled by changing the pH. It has been reported that at pH 9, crystal growth is strongly dominated by the [100] orientations. As the pH increases, starting from pH 10, the crystal orientation started to change toward [110] and [111] directions [75, 76]. The [100] oriented crystal consists of a four-sided pyramidal shape with four-fold symmetry, (Figure 2–6b). This crystal exposes mainly (111) surfaces, which is considered a non-polar surface. The non-polar surface is equally terminated with oxygen and copper atoms, resulting in neutral surface charges, thus lowering the proton absorption on the surface. On the other hand, the crystal oriented with [110] and [111] which have a triangular prism shape (Figure 2–6c) and a three-sided pyramidal shape (Figure 2–6d), respectively, possess polar surfaces. The crystal is primarily dominated by {100} facets, which can have either oxygen terminated or copper terminated surfaces. The oxygen-rich surfaces provide higher proton absorption than the copper-rich surface[77].

Besides the alteration of the crystal facets and orientation due to the pH change, the crystalline quality is also greatly affected. The Cu_2O film deposited at pH 9 has oxygen vacancies due to the lack of hydroxide ions in the electrolyte that act as electron donors, lowering the hole concentrations. In contrast, the Cu_2O electrodeposited at higher pH has primarily copper vacancies that act as acceptors, increasing the hole concentrations significantly[75, 78]. Further investigation reveals that the semiconductor's Fermi level shifts towards more negative values or higher vacuum energy when the Cu_2O film is deposited at high pH and thus placed the conduction band edge in a more favorable position for HER[76].

$$Cu_2O + 2e^- + 2H^+ \rightarrow 2Cu + H_2O \qquad E^o = 0.47\ \text{V vs. NHE} \qquad (15)$$

One limiting factor of Cu_2O is its chemical stability in an aqueous solution under certain cathodic potential (<0.46 V vs NHE). The Cu_2O is reduced to Cu metal (Eq 15). This decomposition reaction is further enhanced during illumination due to the photogenerated charge carriers, contributing to a significant portion of the photocurrent density. In this case, the crystal facets play an important role in the reduction process of the Cu_2O. The oxygen-rich {100} facet attracts more protons and facilitates the reduction of Cu_2O to copper metal more favorably than the {111} facet. As an outcome, the Cu_2O with (111) crystal plane surfaces are more chemically stable than the oxygen-terminated (100) surfaces.

A thin protective layer with certain criteria is often used to improve the chemical stability of the Cu_2O photocathodes. Firstly, it must allow the photogenerated electrons to flow effortlessly from the Cu_2O to the electrolyte. Secondly, the protective coating should not have reductive decomposition reactions in the presence of HER. Thirdly, it should also have beneficial surface charges that can promote the attraction of the protons, which improves the reaction kinetics for water reduction. Lastly, homogenous coverage should be achieved to prevent localized corrosion, which degrades the long-term stability. TiO_2 fits some of these criteria and is frequently investigated as a protective coating to stabilize Cu_2O. However, the deposition of a homogenous TiO_2 layer directly on Cu_2O is still challenging. A report by Paracchino et al. reveals that a thin TiO_2 layer deposited by ALD from titanium isopropoxide, and H_2O is inhomogeneous, which is demonstrated by the decay of the photocurrent after 20 min. This issue is then resolved by adding a buffer layer of Al-doped ZnO (AZO) which not only improves the TiO_2 layer coverage but also forms a rectifying p-n junction with the Cu_2O and enhances the photovoltage of the photocathode. The photocurrent can reach up to -5.7 mA cm^{-2} at 0 V vs. RHE and retain good stability of 78% after 20 min. Pt catalysts were also added to enhance the kinetics of the HER, which increases the photocurrent even higher to -7.6 mA cm^{-2} [17].

Further improvement on the stability and PEC performance was presented by Luo et al.[29]and Pan et al. [79], who utilized the high surface area nanowire structure to increase the photocurrent. The nanowire Cu_2O with AZO as a buffer layer, TiO_2 as a protective coating, and RuO_x as decorated catalyst improves the photocurrent up to -8 mA cm^{-2} at 0 V vs. RHE and retains its stability for 55 hours with 100 % faradaic efficiency of hydrogen [29]. By replacing the AZO buffer layer with Ga_2O_3, the photocurrent increases up to -10 mA cm^{-2} at 0 V vs. RHE with a stable operation for more than 100 hours [79]. This enhancement is due to the bandgap of the Ga_2O_3, which is wider than the AZO and thus creates better band alignment with the Cu_2O, resulting in a higher photovoltage. So far, these coatings on the Cu_2O are deposited with ALD, which is known to have excellent thickness control at the atomic level. However, this method is costly, and hence alternatives should be further explored.

The bare Cu_2O film plays an important role as an absorber to collect photons from sunlight and convert it into electrical energy to split water. The influence of the film thickness of the bare Cu_2O to obtained optimal photocurrent for water splitting has not been thoroughly reported. In this work, the deposition procedure to produce Cu_2O films with various thicknesses and their impact on the PEC performance will be discussed and presented in sections 4.3.1 and 4.6.

2.4 Electrodeposition of metal oxides

The electrodeposition process of metal oxides in aqueous solutions is usually performed in an alkaline environment containing metal ion complexes. The positively charged metal ions form stable complexes with some organic molecules in which oxygen or nitrogen atoms act as electron donors[80]. Stable complexes enable the deposition of a smooth and reproducible oxide layer. A solution based on metal ion complexes is often used to deposit metal alloys by bringing the Nernst potentials of two metal ions closer together[81]. In the case of the Cu ions, the complex agent is used to prevent direct precipitation of copper hydroxide in a high alkaline solution.

In general, metal oxides can be deposited in either oxidizing or reducing conditions from the alkaline solutions. In both cases, the metal ions dissociate from the complex form and precipitate as the metal oxides. The quality and stability of the oxides depend on the deposition parameters such as the applied potential, bath temperature, and pH. In this case, the metal complexes are oxidized into metal ions at the electrode surface, which then reacts with the available hydroxide ions in the electrolyte and produces the oxide film. This oxide film is relatively stable because it was not stripped even though an anodic polarization was applied. Some of the metal oxides that can be synthesized using anodic polarization are CuO [82], AgO [83], Bi_2O_3 [84], and CeO_2 [85].

Deposition of metal oxides can also be performed using cathodic polarization. In this case, the metal ions and hydroxide are reduced at the electrode surface to produce a stable metal oxide film. The ligand of the metal ions complexes based on lactic, tartaric, and citric acid is liberated when applied with cathodic potential due to the protonation process and thus generates hydroxide ions [86, 87]. The Cu_2O is one of the metal oxides that can be deposited using cathodic polarization. Citrate and lactate are commonly used as complexing agents to electrodeposit Cu_2O [74, 88].

2.5 Hydrogen-bubbles templated metal foam

In recent years, a convenient method was developed to produce a highly porous metal structure using a one-step electrodeposition process[89]. The use of hydrogen bubbles as a dynamic template allows the formation of a microporous structure. For most electroplating processes in an aqueous solution, hydrogen evolution is often suppressed and avoided to obtain smooth and compact metal deposits. The reduction of metal ions into a metal film can be accompanied by the hydrogen evolution at a certain cathodic potential range. For example, Cu ions reduce into Cu metal (Eq. 16) at an electrochemical potential of 0.34 V vs. NHE whereas the hydrogen evolution reaction (Eq. 17) only appears at an electrochemical potential of 0 V vs. NHE. This implies that when the electrode is applied at high cathodic potential, both of the electrochemical reactions (Eq. 16 and 17) can occur at the same time but at a different reaction rate. The rate of HER can be controlled by adjusting the cathodic overpotential and monitor the faradaic current efficiency with respect to the metal electrodeposition which quantifies the amount of the metal deposits. At a higher current density, the cathodic overpotential increases greatly (Figure A. 5 in appendix), and the faradaic current efficiency of the metal deposition (Eq. 29 and Figure 4–3) is significantly reduced due to increasing HER, which disrupts the growth mechanism of the metal deposits (see section 4.1).

Hydrogen bubbles have insulating properties and can prevent the electrolyte from directly contacting the cathode surface. This condition causes the metal to be electrodeposited only on the conductive surface between the hydrogen bubbles, leading to the formation of the porous structure. Constant generation and detachment of the hydrogen bubbles create a hydrodynamic effect near the electrode surface and thus influence the surface morphology of the metal deposits. Dendrites and foam structure are the consequence of both the copious hydrogen evolution and the accelerated electrodeposition process due to the high current densities. This method is straightforward, clean, and efficient, which allows the production of a highly porous structure without any additional organic or inorganic template.

The rate of the hydrogen evolution varies with the substrates due to the different activation and adsorption energy of the bubble at the surface. A traditional volcano plot based on the current densities as a function of the hydrogen absorption energy can describe the metal's catalytic behavior toward the hydrogen evolution[90]. Pt and Pd, for instance, have an excellent catalytic property toward hydrogen and can generate a high volume with a fast detachment rate of the hydrogen bubbles[91]. Therefore, the morphology of the porous structure, such as porosity, pore size, and thickness can vary significantly depending on the substrate.

Various metals with porous structure via the hydrogen bubbles template, such as Cu[92], CuSn[93], Au[94], Ni[95], and NiAg[96], have been successfully synthesized. Furthermore, these 3D porous metal structures have also shown promising potentials as electrode material in various applications such as fuel cells[97], batteries[98], sensors[99], and electrocatalysis[100] due to their large surface area and high electrical conductivities. However, the pore walls of these porous structures often grow in ramified dendritic structure, which is fragile and thus limits their application in compact devices.

The investigation and the progress regarding the mechanical stability of these porous structures have not been found in the literature. Some approaches were performed to control the size of the dendritic branch in the pore walls by adding chemical additives to the electrodeposition bath to make the structure more compact. For instance, in the case of porous Cu, a small amount of chloride ions was added to the bath to accelerate the deposition of Cu, thus making the pore walls denser [89]. However, even with this approach, the pore walls are still comprised of the dendritic structure, which suggests that there was no improvement in the mechanical stability of the porous structure.

In this work, the mechanical stability of the porous structure, especially toward hydrogen evolution, will be discussed and presented in sections 4.1 and 4.2. Furthermore, a novel approach is proposed to enhance the porous structure's mechanical stability, which provides promising prospects to be implemented for different applications, especially as energy materials such as batteries, fuel cells, electrolyzers, etc.

3 Experimental procedure

3.1 Electrochemical deposition of copper

The Cu electrodeposition was carried out galvanostatically using a potentiostat (Bio-Logic science instruments SP-240) equipped with a ±4 A booster kit in an acidic Cu bath (pH ~0). The bath contains 0.2 M $CuSO_4$ and 1 M H_2SO_4 in double-distilled water. The high acidity of the bath can prevent the formation of an oxide layer and produced a stable Cu deposit. The bath provides high faradaic efficiency (>90%) for a copper deposition at a low current density (<-20 mA cm^{-2}). However, as the current density increases, the efficiency of the copper deposition decreases due to the increased hydrogen evolution. The electrodeposition process was carried out in a three-electrode configuration where a 27 mm flat Cu coin (99.9%) is used as a working electrode, a Pt foil as a counter electrode, and an Ag/AgCl (sat. KCl) as a reference electrode. The change of the voltage during the electrodeposition process. The two main chemical reactions during the electrodeposition process are in Eqs. 16 and 17.

$$\mathrm{Cu}^{2+} + 2\mathrm{e}^- \rightarrow \mathrm{Cu} \tag{16}$$

$$2\mathrm{H}^+ + 2\mathrm{e}^- \rightarrow \mathrm{H}_2 \tag{17}$$

3.1.1 Fabrication of porous Cu framework

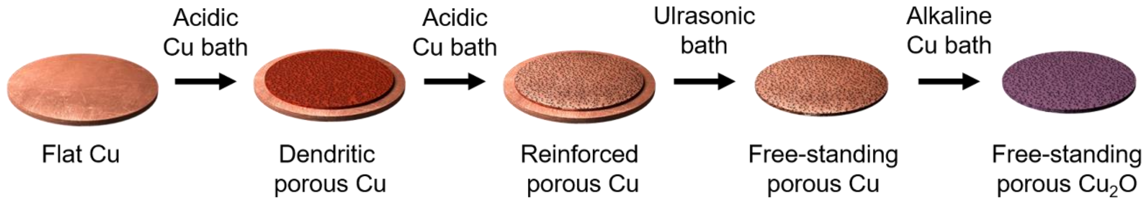

Figure 3–1 Schematic representation of the electrochemical procedure to synthesize porous Cu_2O photocathode

A stable and compact porous Cu framework was synthesized in two electrodeposition steps (Figure 3–1). In the first step, a dendritic porous Cu framework was synthesized by utilizing hydrogen bubbles as a dynamic soft template to create the microporous structure. In this case, the acidic bath plays a vital role in ensuring a steady production of a copious amount of hydrogen bubbles. A custom cell was constructed to place the working electrode (flat Cu coin) at the bottom of the cell so that the hydrogen bubbles can detach quickly. The cell consists of a PVDF sample adapter and a PMMA cell container which can hold a maximum of 45 mL of electrolyte (Figure 3–3).

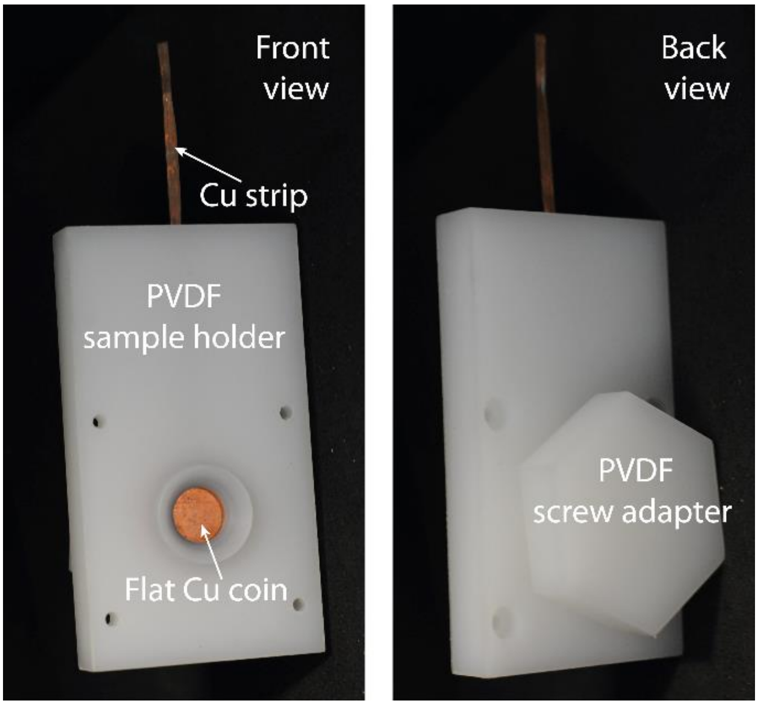

Figure 3–2 Photographs of the custom-made PVDF sample holder and adapter.

The sample adapter has a circular hole with a diameter of 1.13 cm that exposes the Cu coin with a specific geometric surface area of 1 cm^2 to the electrolyte (Figure 3–2). The cell container was then attached on top of the sample holder, and 25 ml of the electrolyte was applied. Prior to the electrodeposition process, the Cu coin was mechanically polished using 4000 grit sandpaper and then electropolished in 30 vol. % H_3PO_4 for 1 min at 2 V vs. Cu to smoothen the surface (root mean squared surface roughness (Sq) of ~3 nm). The Cu coin was then dipped in 0.1 M H_2SO_4 for about 30 s to activate the surface. The Pt foil counter electrode and Ag/AgCl (sat. KCl) reference electrode were placed from the top in an upright position (Figure 3–4). To ensure a homogenous porous structure, the Pt foil was placed away from the direct path of the hydrogen bubbles. For safety purposes, the experiment was performed under a fume exhaust hood.

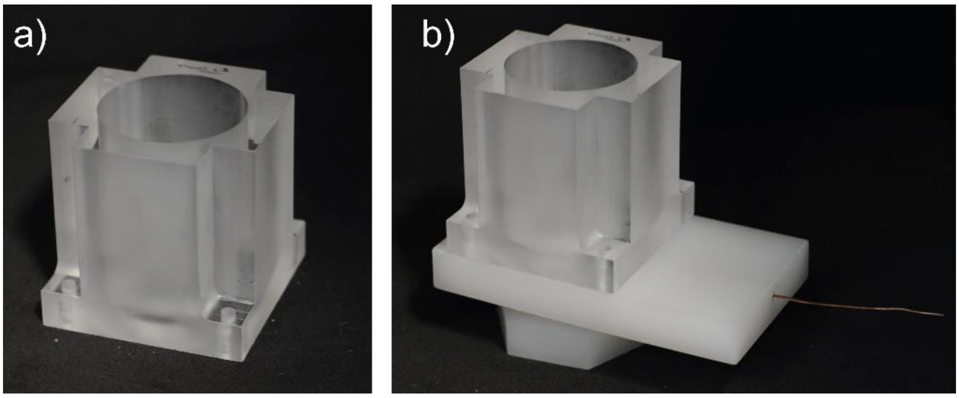

Figure 3–3 Photograph of a) a PMMA cell container and b) an assembled cell with the sample adapter

Two sets of experiments were conducted to study the porous structure:

- Different high current densities were applied between -0.075 A cm^{-2} and -2.25 A cm^{-2} at various duration times to investigate the porosity and morphology of the porous structure.
- The current density was fixed at a high current density (-1.5 A cm^{-2}, -2 A cm^{-2}, etc.), and the electrodeposition time was varied between 2 s to 60 s to investigate the influence of the hydrogen formation role on the porous structure.

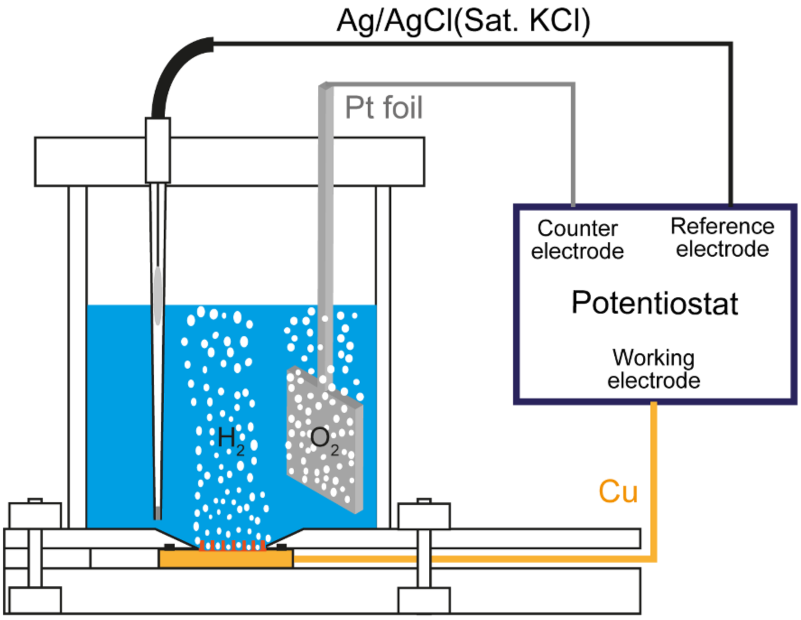

Figure 3–4 Electrochemical deposition process of dendritic porous Cu in an acidic bath containing 0.2 M CuSO4 and 1 M H_2SO_4 at pH ~0

3.1.2 Reinforcement and separation procedure of the porous Cu

A second electrodeposition step was implemented to improve the mechanical stability of the dendritic porous Cu. This procedure was performed in the same bath after the first electrodeposition step. Prior to the electrodeposition process, the trapped hydrogen bubbles inside the pores must first be released to ensure homogenous deposition of Cu. The removal of the bubbles can be achieved by slightly tapping and shaking the cell a few times. Intense mechanical agitation or using an ultrasonic bath can destroy the delicate and fragile structure of the dendritic porous Cu easily. Next, a small current density of -20 mA cm^{-2} (calculated with a geometric surface area of 1 cm^2) was applied to the working electrode to limit the hydrogen evolution and ensure a compact deposition of the Cu layer. The electrodeposition duration (reinforcement time) was varied from 5 to 120 min to study the change in the morphological structure.

The reinforced porous Cu samples can easily be separated entirely from the Cu coin to obtain a free-standing porous Cu framework. The separation was done by placing the sample in an ultrasonic bath (35 kHz/160 W, Bandelin Sonorex Super RK 510 H) for at least 5 min, and it was repeated at least three times. The Cu coin can then be reused for the next batch of the porous Cu samples.

3.2 Electrodeposition of cuprous oxide in an alkaline bath

The Cu_2O was electrodeposited on various substrates, including an Au coated Si substrate, a flat Cu coin, and porous Cu frameworks (dendritic porous Cu, reinforced porous Cu, and free-standing porous Cu). Different from the electrodeposition of Cu metal, the Cu_2O was electrodeposited using a potentiostatic electrodeposition method. The current was recorded over the electrodeposition time with a fixed voltage applied to the working electrode.

The electrodeposition of Cu_2O was carried out at -0.4 V vs. Ag/AgCl (sat. KCl) in a three-electrode configuration where a flat Cu coin or the porous Cu frameworks is used as the working electrode, Pt foil as a counter electrode, and Ag/AgCl (sat. KCl) as the reference electrode. In this case, an alkaline copper bath containing 0.2 M $CuSO_4$ (>99.8% copper sulfate, Honeywell Fluka) and 1 M $Na_3C_6H_5O_7$ $2H_2O$ (>99% trisodium citrate dihydrate, Sigma-Aldrich) as a complexing agent in double-distilled water was used. The pH was adjusted to ~12 by slowly adding a decent amount of 6 M NaOH (>97% sodium hydroxide, Sigma-Aldrich) solution. The Cu ions react with the trisodium citrate and form copper(II)-citrate complexes [88, 101]. During the formation of these complexes, a chemical reaction occurs, and protons are produced which thus decreases the pH of the bath as was reported by Daniele et al. [102]. Adding a high concentration of the NaOH solution is necessary to increase the pH and obtained a stable predominant dimer $[Cu_2H_{-2}Cit_2]^{4-}$ which is only available at pH higher than 7 [88]. The high alkalinity of the electrolyte also plays an important role to ensure the good quality of p-type Cu_2O crystal and stabilize the Cu_2O layer. The reduction process to Cu_2O in alkaline solution is shown in Eq. 18. The equation is simplified to better define the role of hydroxide ions in the formation of the Cu_2O film. The citrate ligand is expected to be liberated due to protonation from the cathodic potential. It is expected that the decrease of the hydroxide ions due to the chemical reaction lowered the pH of the bath. This behavior was observed after the electrodeposition of the Cu_2O film at -0.4 V vs. Ag/AgCl for 2 hours.

$$2\mathrm{Cu}^{2+}_{(\text{in a complex form})} + 2\mathrm{OH}^- + 2\mathrm{e}^- \rightarrow \mathrm{Cu_2O} + \mathrm{H_2O} \tag{18}$$

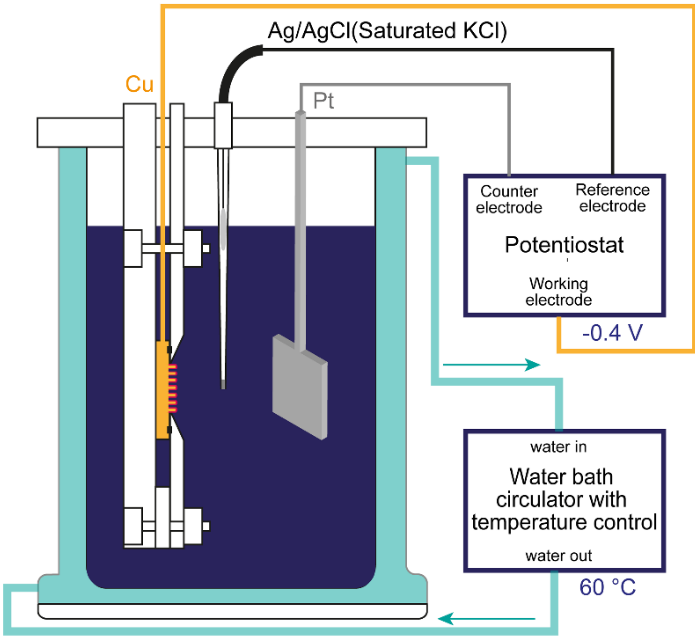

Figure 3–5 Electrodeposition process of Cu_2O in an alkaline copper bath at 60°C.

A double-wall glass cell containing 150 mL of the electrolyte is used for the experiment (Figure 3–5). A thermostat was attached to the glass cell to control the cell's bath temperature uniformly. The electrolyte was kept at 60°C and magnetically stirred at 400 rpm. The electrodes, including the working electrode, were inserted from the top and were held by a custom-made electrode holder, which covers the entire lid of the cell and prevents water evaporation. The evaporation can influence the pH and alter the electrodeposited layer. For this section, the duration of the electrodeposition time was varied between 5 min to 60 min, and the grain size, thickness, and PEC performance were analyzed. Fresh electrolyte was used for each deposition.

3.2.1 Surface facets modification using hexamethylenetetramine as a capping agent.

The crystal orientation and the surface facets of the Cu_2O have a significant impact on the PEC performance. To tailor the crystal orientation of the Cu_2O grains, a capping agent, hexamethylenetetramine (>99% HMT, Merck KGaA), was added to the alkaline electrolyte. At pH 12, the positively charged HMT molecules are absorbed on the negatively charged surfaces of the Cu_2O and affect the growth mechanism resulting in different crystal shapes and orientations. The crystal orientation of the substrates affects the growth mechanism of the Cu_2O. For instance, the Cu_2O electrodeposited on a sputtered gold surface with [111] orientation tend to grow epitaxially [103]. The HMT capping agent is used to change the crystal orientation of the Cu_2O grains without altering the crystalline properties of the substrate.

A polycrystalline flat copper coin and free-standing porous Cu framework were used to investigate the relation between the concentration of the HMT and the crystal orientation of the Cu_2O to the PEC performance. The HMT concentration was gradually increased from 0 to 1126 mM, and a fresh alkaline electrolyte is used for each electrodeposition process. XRD analysis using Bragg-Brentano geometry was carried out to extract the crystalline properties of the deposited Cu_2O layer. Part of this work was performed in the Master thesis of Mayra Marimon[104].

3.3 Material characterization

3.3.1 Morphological analysis

The surface morphology of the samples was investigated by using field-emission scanning electron microscopy (FESEM, Hitachi S-4800). In this case, secondary electron imaging was used to reveal the sample's features, and a low acceleration voltage of 5 kV was applied to minimize charging. The samples were taped using conductive carbon tape onto an aluminum sample holder and were transported into an ultra-vacuum chamber (1

$\times 10^{-9}$ —1×10^{-12} Torr). The measurement was done with the same sets of magnification. For the cross-section analysis, the samples were cut using a sharp hand lever scissor. They were taped vertically on an L-shaped sample holder to reveal the cross-sectional part of the deposited film or porous layer. The layer thickness was evaluated from the cross-sectional SEM image. The porous Cu SEM micrograph was converted into a binary image using ImageJ free software (search for color threshold under the images tab menu, adjust the pop-up slider to get the right contrast of the processed image), which enhanced the contrast between the dark pore holes and the bright wall of the porous structure. Using the analysis tools from the same software, the porosity of the porous Cu samples can be estimated.

The surface roughness was evaluated using an atomic force microscopy (AFM) device from Bruker (Dimension ICON), placed in an Ar-filled glove box. The AFM was mainly used to investigate the surface roughness of the deposited Cu_2O film. Unfortunately, due to the limitation of the depth measurement, the AFM device could not provide information regarding the height profile of the porous Cu structure. The AFM measurement was performed using PeakForce tapping mode with a ScanAsyst air probe to obtained high-resolution images and accurate height measurement. The scan rate was fixed at 1Hz for all measurements, and the scan size was set at 5 x 5 and 2 x 2 μm^2. All the AFM images underwent third order polynomial flattening procedure to remove the tilt and bow errors.

3.3.2 Composition and structural analysis

X-ray diffraction (XRD, Siemens D5000) is used to determine the crystalline structure, and crystal orientation of the Cu_2O film and Cu substrates. The measurement was performed using Bragg-Brentano θ-2θ geometry with Cu Kα radiation at 40 kV in a parallel beam optic. This geometry is used to identify the crystal plane that is parallel to the substrate. The 2θ scan range was set from 20° to 90° with a scan rate of $0.02° s^{-1}$. The texture analysis developed by Berube et al.[105] was implemented by calculating the relative texture coefficient from the XRD data to determine the preferred crystal orientation of the Cu_2O film. This method involves several steps:

- From the X-ray diffractogram of the sample, the intensity ratio R1(hkl) is calculated from the relation between the peak intensity at individual detected (hkl) reflection and the sum of the peak intensities of all (hkl) reflections that were observed (Eq. 19).

$$R1(hkl) = \frac{I(hkl)_s}{\sum_i^n I(h_i k_i l_i)_s} \times 100\% \tag{19}$$

- The intensity ratio R2(hkl) is obtained from the reference powder X-ray diffractogram, which is available in the crystallography XRD database and was calculated according to Eq (20).

$$R2(hkl) = \frac{I(hkl)_p}{\sum_i^n I(h_i k_i l_i)_p} \times 100\% \tag{20}$$

  The subscripts s and p represent the analyzed Cu_2O sample and the reference powder sample, respectively, and n is the total number of the detected peaks.

- The texture coefficient (TC) at individual (hkl) reflection is defined by calculating the ratio between R1(hkl) and R2(hkl), (Eq. 21). If the TC is greater than one, it indicates a preferred orientation of the (hkl) reflection. However, the acquired preferred orientation is an absolute value and independent from the other (hkl) reflections of the sample.

$$TC(hkl) = \frac{R1(hkl)}{R2(hkl)} \tag{21}$$

- The relative texture coefficient (RTC) establishes the relationship of the texture coefficient for individual (hkl) reflection with the other observed reflections (Eq.22). As a result, the preferred crystal orientation investigated by this method is relative to all crystal orientations of the analyzed sample.

$$RTC(hkl) = \frac{TC(hkl)_s}{\sum_i^n TC(h_i k_i l_i)_s} \times 100\% \tag{22}$$

  The crystal orientation at specific (hkl) reflection is defined to have a preferred crystal orientation if the value of the RTC is above the threshold value (100 % divided by the total number of (hkl) reflections obtained from the sample). The RTC analysis was performed on planar samples (Cu_2O on flat Cu coin) to understand the influence of HMT on the crystal orientation (see section 3.2.1 for detail experimental) of the Cu_2O film.

For further characterization techniques, the sample composition and the crystal quality of the deposited Cu_2O film are analyzed by using Raman spectroscopy. The measurement was carried out using a Renishaw In-Via Raman spectrometer with a 514 nm incident laser with a 100x objective lens. Photoluminescence spectroscopy was also performed using the same device but with a 488 nm incident laser to determine the type of defects such as oxygen vacancies and copper vacancies of the Cu_2O film.

3.3.3 Optical Characterization

The optical measurement of the free-standing porous Cu_2O was carried out using an Ultraviolet-visible (UV-Vis) spectrometer (Varian Inc., Cary 5000). Two configurations were used to obtain the transmittance and diffuse reflectance spectra of the samples separately. For the transmittance spectroscopy, a sample holder that exposes a square of 1 cm^2 was used. The holder was placed in between the direct pathway of the incident light to the detector. A Zero/baseline correction was performed. The 100%T baseline was obtained by first allowing the incident light to pass through the hole of the sample holder towards the detector. The intensity of the transmitted light at different wavelengths was recorded. Next, the 0%T baseline was acquired by placing a metal plate on the sample holder to block all the incident lights. A transmittance reference can be obtained by subtracting the intensity of the 100%T baseline with the 0%T baseline. The sample can then be placed onto the sample holder, and the measurement was performed with a spectral range between 400 – 800 nm. The transmittance measurement was done to estimate the porosity of the free-standing porous Cu_2O.

The diffuse reflectance measurement requires an integrating sphere to collect all the light to the detector. The wall of the integrating sphere is made of a highly reflective fluoropolymer (spectralon). The measurement calibration was done by placing a spectralon sample to obtain 100%Reflectance (100%R) and then removing it to get the 0%Reflectance. Like the transmittance measurement, the zero/baseline correction was required. The measurement was also performed in the same spectral range between 400 – 800 nm.

The Tauc method is used to determine the bandgap energy of semiconductor material. This method is based on the energy-dependent absorption coefficient (α) (Eq. 23).

$$(\alpha h\nu)^{1/\Upsilon} = B(h\nu - E_g) \tag{23}$$

In (Eq. 23) h is the Planck constant, ν is the photon's frequency, B is a constant, E_g is the bandgap energy of the semiconductor, and the Υ factor depends on the nature of electron transition and is set to either 0.5 or 2 for direct or indirect transition band gaps, respectively. The absorption coefficient can be transformed from the diffuse reflectance spectra using the Kubelka-Munk function ($F(R_\infty)$)(Eq. 24).

$$F(R_\infty) = \frac{K}{S} = \frac{(1 - R_\infty)^2}{2R_\infty} \tag{24}$$

In (Eq. 24), K and S are the absorption and scattering coefficients, respectively and R_∞ is the diffuse reflectance of an infinitely thick specimen. By substituting the α in Eq. 23 with the $F(R_\infty)$, the $(F(R_\infty)h\nu)^{1/2}$ (Cu_2O has direct bandgaps, so the ϒ is set to 2) can be plotted against the photon energy ($h\nu$), which reveals the properties of the semiconductor material. The linear region of the curve can then be fitted with (Eq. 23), and the x-axis intersection of the linear fit provides an estimate of the band gap.

3.3.4 Mott-Schottky analysis

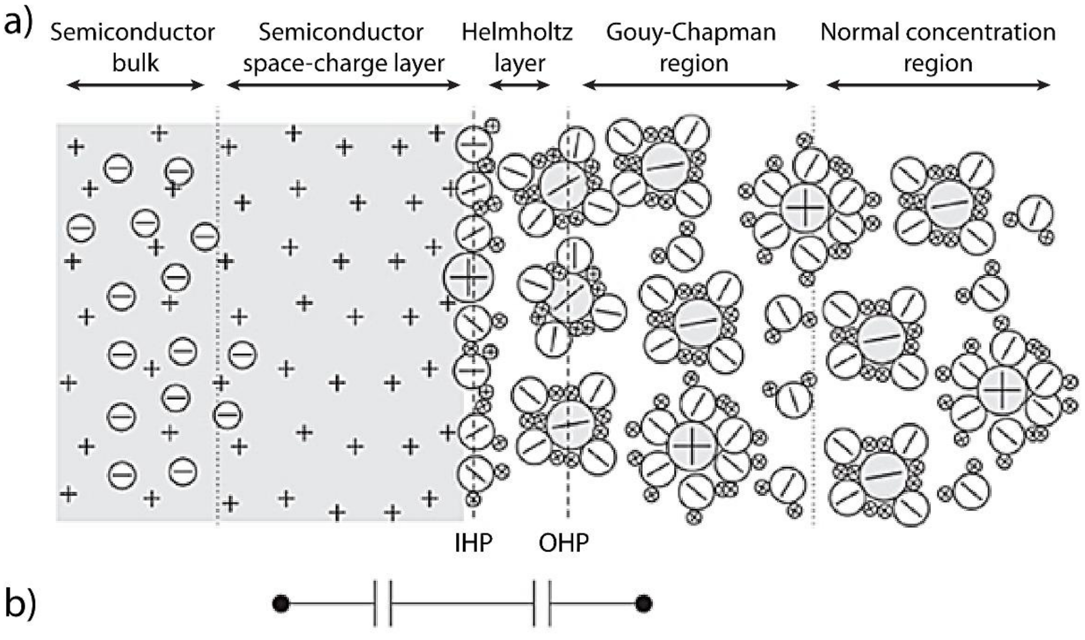

Figure 3–6 Schematic diagram of a) electrical double layer at the interface between the n-type semiconductor and the electrolyte and b) an equivalent circuit consisting of a space charge capacitance of the semiconductor and double layer capacitance connected in series. IHP and OHP are the inner and outer Helmholtz planes, respectively. This diagram is adapted from the reference [106].

When a semiconductor is immersed in an electrolyte, two regions of charge separation are found at the interface, the space charge region of the semiconductor and the electrical double layer (Figure 3–6). The space-charge capacitance determines the properties of the semiconductor and can be extracted using Mott-Schottky analysis. The space charge capacitance is much smaller than the double layer capacitance in the electrolyte. Since both capacitances are connected in series at the interface, the reciprocal value of the small space charge capacitance has a more significant impact on the overall measured capacitance. Experimentally, this capacitance (C) can be obtained by extracting the imaginary part of impedance (Z") (Eq.25), using electrochemical impedance spectroscopy (EIS). A small sinusoidal voltage of 15 mV with varying range frequency (f, 30 kHz - 63 kHz) is applied to the working electrode (Cu_2O photocathodes) during the EIS process. The measurement was performed in 0.5 M Na_2SO_4 (>99% sodium sulfate, Sigma-Aldrich) electrolyte with the same three-electrode configurations and potentiostat as discussed in sections 3.1 and 3.2.

$$C = \frac{1}{\omega Z''} \tag{25}$$

The space charge capacitance of the semiconductor changes at different potential biases, depending on whether the charge carrier at the interface is accumulated or depleted. Therefore, to determine this behavior for the Cu_2O samples, the potential was scanned from -0.1 to 0.15 V vs. Ag/AgCl (sat. KCL) with a 6-mV potential step using the staircase potentio electrochemical impedance spectroscopy (SPEIS) mode. The Mott-Schottky plot can be obtained by selecting a specific impedance frequency and plotting the reciprocal of the square of capacitance (C^{-2}) against the applied voltage. The plot can then be used to determine the semiconductor's flat band potential and charge carrier density. The type of the semiconductor can also be identified by examining the sign of the slope between the charge accumulation plateau and charge depletion plateau, which is influenced by the minority charge carrier of the semiconductor.

A negative slope indicates a p-type semiconductor, while a positive slope indicates an n-type semiconductor. When the charge carriers are accumulated in the space charge region, the capacitance increases, and thus C^{-2} becomes small. Opposite behavior occurs for the depletion of the charge carrier. For a p-type semiconductor, when the applied voltage is more positive than the flat band potential[3], charge accumulation occurs while more negative potentials lead to charge depletion. The linear part of the curves between the accumulation and depletion region was fitted with Eq. 26 and extrapolated to the x-axis. The potential at the x-axis intersection represents the flat-band potential (where $C^{-2} = 0$), and the slope is used to estimate the charge carrier density based on the Mott-Schottky equation in Eq. 26.

$$\frac{1}{C^2} = \frac{-2}{\varepsilon_r \varepsilon_0 A^2 e N_a}\left(E - E_{fb} - \frac{k_B T}{e}\right) \tag{26}$$

In Eq 26, C is the space charge capacitance, ε_r is the relative dielectric constant of Cu_2O (7.6)[107], ε_0 is vacuum permittivity, A is the surface area of the electrode, e is the elementary charge, N_a is the acceptor charge carrier density, E is the applied potential, E_{fb} is the flat band potential, k_B is Boltzmann constant, and T is the absolute temperature.

3.4 Photoelectrochemical characterization

3.4.1 Photoelectrochemical cell and solar simulator configuration

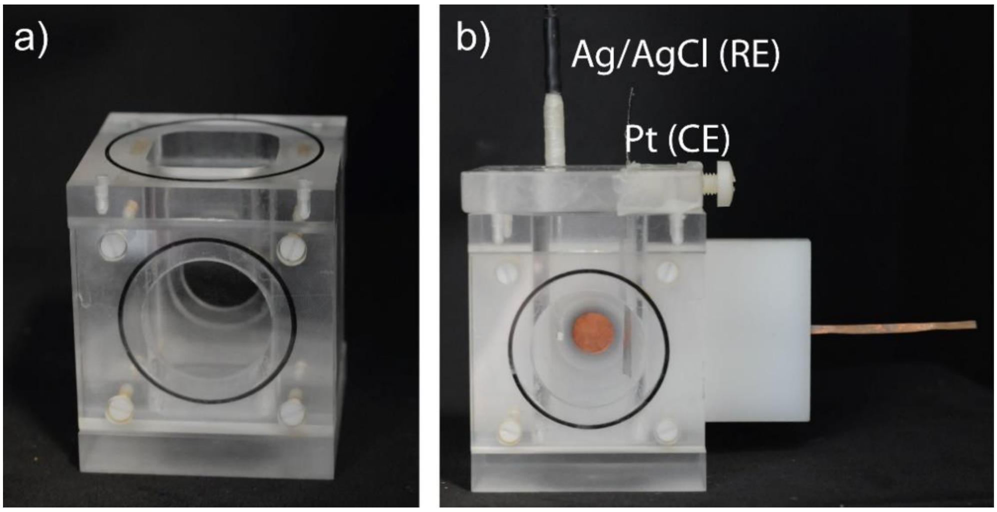

Figure 3–7 Photograph of a) PMMA PEC cell with a transparent front window and b) fully assembled PEC cell with sample adapter and electrodes holder. The reference electrode (RE) and counter electrode (CE) is placed on the left and right sides, respectively, of the copper working electrode (WE).

The PEC cell used in this work consists of three main components, a 5 mm thick PMMA transparent window, a PMMA container that can hold ~40 ml of the electrolyte, and a sample holder (Figure 3–7). The sample holder is similar to the one that was described

---

[3] The potential at which there is no depletion or accumulation of the charge carrier at the junction between the semiconductor and electrolyte resulting in no band bending at interface.

in section 3.1.1(Figure 3–2). It was constructed to be implemented for the preparation and characterization procedure. The same three-electrode configuration and a potentiostat described in sections 3.1 and 3.2 were used for the PEC experiments. An electrode holder made of PMMA was used to position the counter and the reference electrodes from the top of the cell. These electrodes need to be carefully positioned not to block the light beam (Figure 3–7b). The PEC cell was placed on an adjustable laboratory lifting platform to align it with the light beam from the solar simulator.

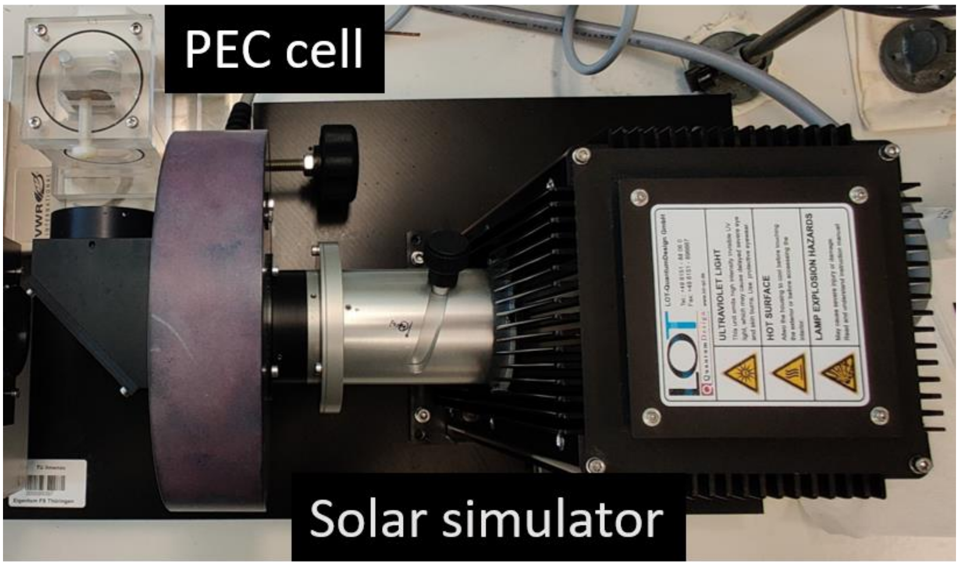

Figure 3–8 Solar simulator configuration for the PEC experiment (top view).

A solar simulator equipped with a 150 W xenon lamp (LOT-Quantum Design LS0108/15G) an AM 1.5 filter and a mechanical shutter (Figure 3–8) is utilized as a light source. The mechanical shutter can be modulated to provide information on the semiconductor with the light off and on. The shutter controller is connected to the potentiostat, allowing a synchronized control of the light source during the electrochemical experiments. Prior to the measurement, the solar simulator was operated continuously for about 15 min to reduce the xenon lamp's flickering and reach optimum power. The light intensity was calibrated using a reference solar cell (ReRa solution), and the custom-made PEC cell (without the sample adapter). The reference solar cell was placed at the back of the PEC cell, and the position of the cell was adjusted to provide the light intensity of 100 mW cm^{-2} or 1 sun at the sample surface. The PMMA window has ~85 % transparency, and thus it is crucial to tune the light intensity with the PEC cell presence to give an accurate measurement.

3.4.2 Photoelectrochemical analysis

The photoactivity of the Cu_2O photocathode for the PEC water splitting performance was investigated using linear sweep voltammetry (LSV). The voltage was scanned from -0.1 to -0.7 V vs. Ag/AgCl (sat. KCl), and the current density was recorded using a Biologic potentiostat SP-240 under chopped light illumination with an on-off duration of 5 s consecutively. The current density is divided into two categories, the measured current under light illumination (photocurrent) and the measured current when the light is turned off (dark current). The photocurrent provides the analysis regarding the photoactivity and the PEC performance of the sample. The dark current provides information regarding the electrochemical stability of the photoelectrode. The measurement was performed in 0.5 M Na_2SO_4 (Carl Roth) at a scan rate of 5 mV/s. The cell was purged with argon for at least 15 min before starting the LSV measurement. The potential was converted from vs. Ag/AgCl (sat. KCl) to the reversible hydrogen electrode (RHE) using Eq. 27.

$$E_{RHE} = \mathrm{E} + 0.059\, pH + E_{Ag/AgCl\,(sat.KCl)} \tag{27}$$

In Eq. 27, E is the measured working potential and $E_{Ag/AgCl\,(sat.KCl)}$ is the potential of Ag/AgCl (sat. KCl) reference electrode which is 0.197 V at 25 °C. This conversion was performed to simplify the comparison with other literature data.

For the PEC measurement of the free-standing porous Cu_2O, the sample was taped onto a gold-plated brass coin and was placed inside the sample adapter. The gold-plated brass coin provides good ohmic contact and exposes only one side of the free-standing porous Cu_2O sample to the electrolyte. This configuration allows for better comparison with the other sample that was deposited on a flat Cu substrate. The sample adapter ensured a reproducible exposure of the surface with a geometric surface area of 1 ± 0.01 cm^2 to the electrolyte. The PEC performance for different samples deposited on various substrates is evaluated, and the photocurrent densities at a potential of 0 V vs. RHE were compared.

4 Results and discussion

4.1 Dendritic porous Cu framework

Increasing the active area and optimization of the morphology creates more active sites for the photoelectrochemical reactions. By varying the electrodeposition duration (40 – 400 s) and current density (-0.075 – -2.25 A cm^{-2}), different surface morphologies of Cu layers (Figure 4–2Figure 4–1a-f) could be obtained. The durations and current densities were adjusted accordingly to reach the average thickness of ~200-250 µm for better comparison.

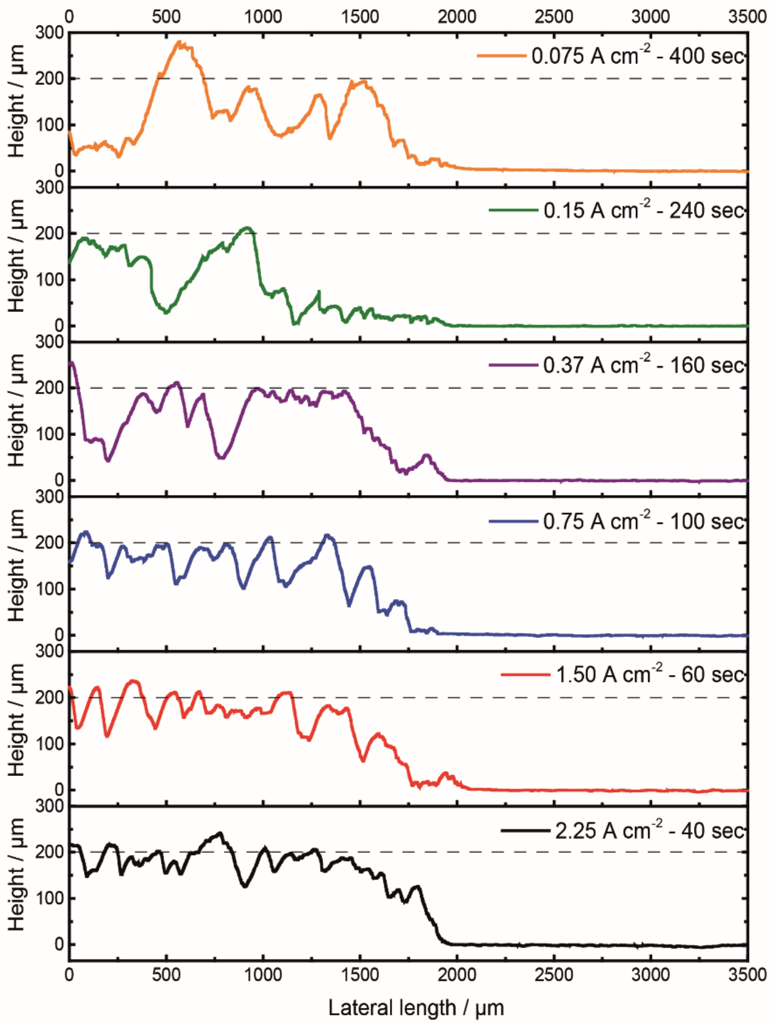

Figure 4–1 Height profiles of various dendritic porous Cu structures electrodeposited in an acidic copper electrolyte (0.2 M $CuSO_4$ and 1 M H_2SO_4) with different current densities and durations (see information at the top left corner of each graph).

The thickness of the deposited Cu layer was measured using a contact profilometer (Veeco Dektak 150) equipped with a stylus with a tip diameter of 10 µm. The measurement was carried out with an applied mass of 3 mg, scan size of 3.5 mm, and a scan rate of 0.2 µm s^{-1}. The scan was initiated from the surface of the porous layer and stopped at the flat Cu surface. A leveling procedure was performed on the flat Cu surface using the Dektak software to remove the tilt error. Figure 4–1 shows that as the current density increases, the height difference between the hills and valleys of the curve becomes relatively smaller, and the number of the peak variations increases. Additionally, the widths of the valleys also decrease significantly, especially for the samples deposited at higher current densities, starting from -0.75 A cm^{-2}.

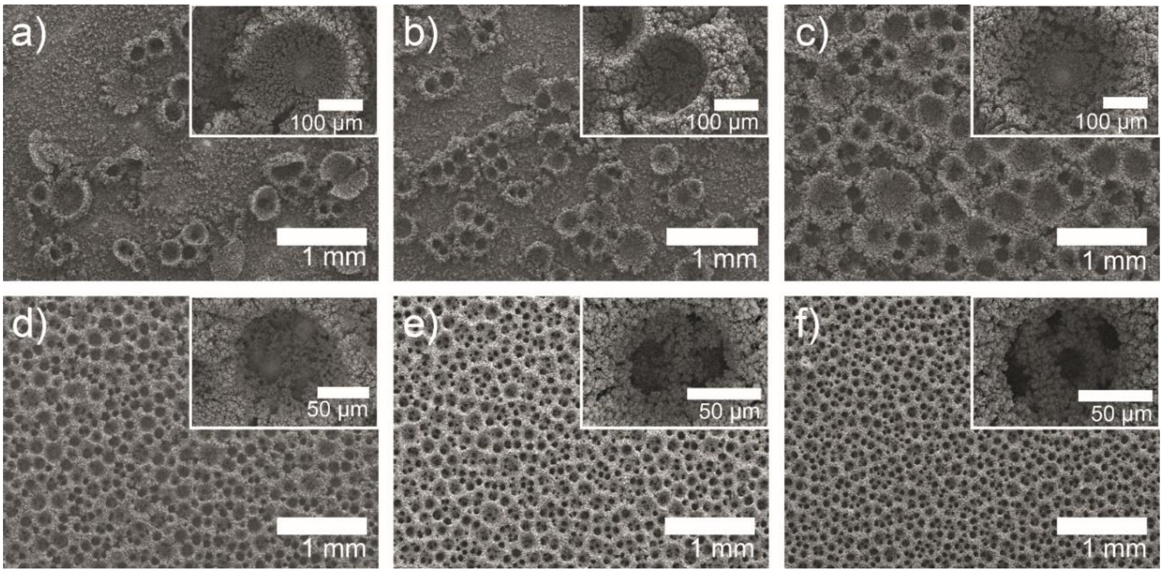

Figure 4–2 Scanning electron micrographs of the electrodeposited dendritic porous Cu structures on a flat Cu substrate in an acidic copper bath using different current densities and deposition durations: a) -0.075 A cm^{-2}, 400 s; b) -0.15 A cm^{-2}, 240 s; c) -0.37 A cm^{-2}, 160 s; d) -0.75 A cm^{-2}, 100 s; e) -1.5 A cm^{-2}, 60 s and f) -2.25 A cm^{-2}, 40 s. The insets show magnified images of the pores.

SEM shows that only a small amount of widely scattered porous structures were obtained for the sample that was deposited with low current densities and long deposition time (Figure 4–2a and b). At higher current densities, starting from -0.37 A cm^{-2} with an electrodeposition time of 160 s, the surface gets fully covered with porous structures. The formation of these porous structures is strongly influenced by the amount and size of the hydrogen bubbles generated during the electrodeposition process[91]. The high current densities increase both the hydrogen productions and the detachment rate of the bubbles from the flat Cu surface, which influences the modification of the pore size diameter. To obtain the current efficiency, the weight of the deposited Cu obtained at different current densities is measured using an analytical balance (Sartorius AG, Bp301S) and then was divided by the theoretical mass calculated using the Faraday equation (Eq. 28).

$$m = \frac{M \cdot Q}{n \cdot F} \tag{28}$$

In Eq. 28, m is the theoretical mass, Q is the total charge measured, M is the molar mass of the substance, and n is the number of electrons per ion.

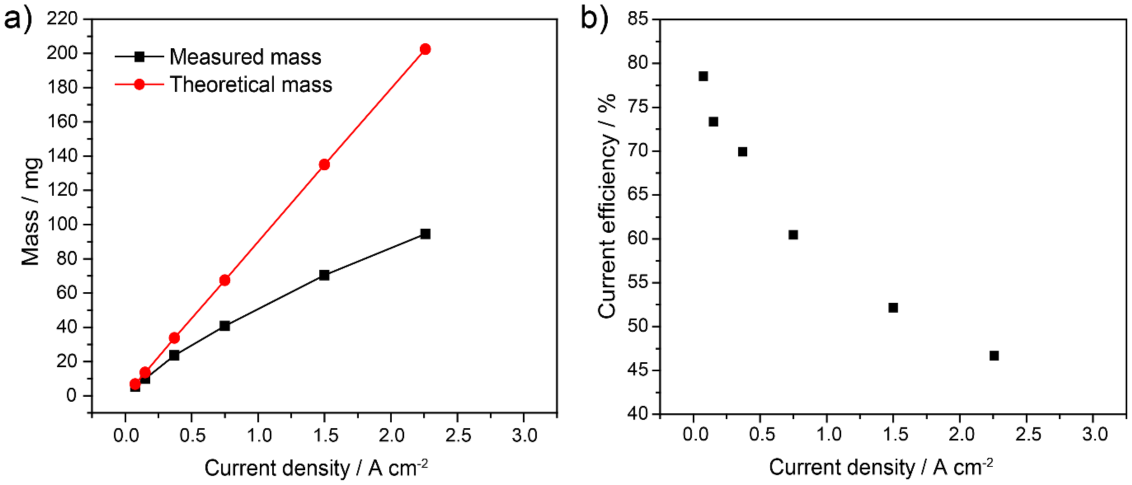

Figure 4–3 Influence of applied current density on the change of a) mass and b) current efficiency for electrodeposited Cu on flat Cu substrate.

The value of the measured mass deviates from the theoretical mass as the current density increases, leading to the decreasing current efficiency (Figure 4–3). The reason for this is likely caused by the hydrogen evolution, which occurs in parallel during the electrodeposition process. At low current density (-0.075 A cm^{-2}), the Cu deposition has high current efficiency of ~78% and a low hydrogen evolution rate, limiting the formation of the bubbles on the surface of the substrate and reducing the porosity of the sample (Figure 4–2a and b). In addition, the large pore size also suggests that the bubbles accumulate and stay longer before detaching from the surface. As the current density increases to -0.75 A cm^{-2}, the average pore size on the top layer decreases significantly from ~300 µm (Figure 4–2a-c) to ~100 µm (Figure 4–2d-f). Beyond -0.75 A cm^{-2}, there is no significant difference in the average pore size, but the number of interconnecting pore tunnels shown in the insets in Figure 4–2d-f increases. To better understand these interconnecting pore tunnels and the formation of the porous structure, different samples were deposited at a fixed current density of -1.5 A cm^{-2}, and the electrodeposition time was varied from 2 s to 60 s.

The pore size becomes larger as the electrodeposition time gets longer (Figure 4–4). The deposited samples with shorter durations (2-5 s) have relatively small pores (10-25 μm), and no interconnecting pore tunnels are present. As the electrodeposition time extended, the amount of the deposited Cu increases, making the porous layer thicker, and also the interconnecting pore tunnels become apparent. This phenomenon is likely due to the characteristic of the hydrogen bubbles that act as the dynamic template to form the porous structure. The tiny bubbles generated on the surface of the flat Cu substrate coalesce and thus create larger bubbles at the upper layer.

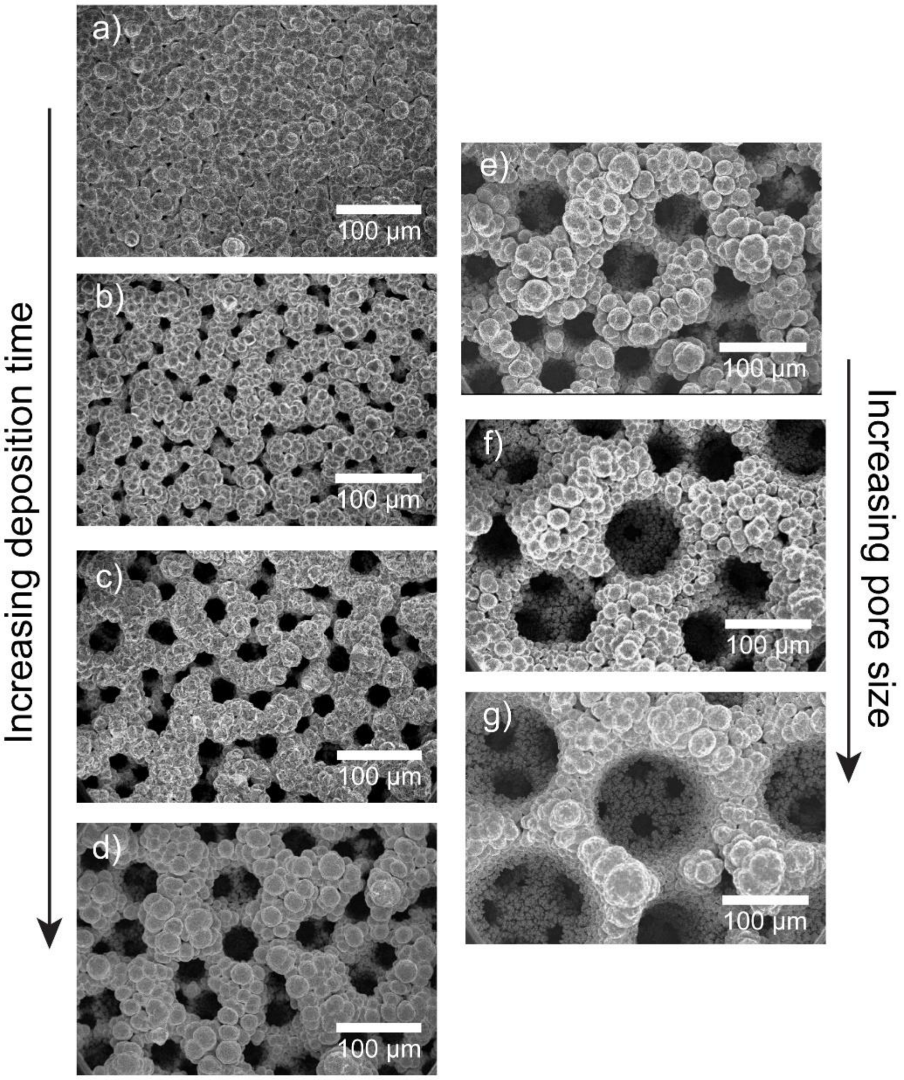

Figure 4–4 Morphological comparison of the electrodeposited porous Cu structure on flat Cu substrate deposited at a fixed current density of -1.5 A cm^{-2} for a) 2 s, b) 5 s, c) 10 s, d) 20 s, e) 30 s, f) 40 s and g) 60 s. These samples undergo a reinforcement procedure for 60 min (see section 3.1.2).

The structure comprises small Cu grains (Figure 4–5) with a size between ~300 nm to ~1 µm. Although these dendritic structures provide a large surface area, they are very delicate and could be damaged in a PEC water splitting application.

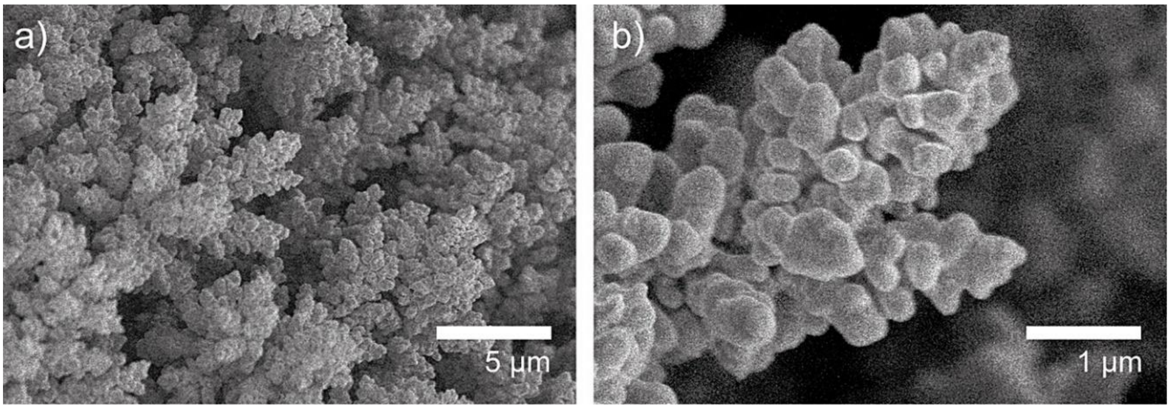

Figure 4–5 Magnified wall of the porous Cu layer electrodeposited at -1.5 A cm^{-2} for 60 sec with a) 5x and b) 25x magnifications.

To investigate the mechanical stability of this ramified dendritic porous Cu sample, a water-splitting experiment was performed on the dendritic porous Cu sample. The sample that was electrodeposited at -1.5 A cm^{-2} for 60 s was immersed in 0.5 M Na_2SO_4 electrolyte, and a strong hydrogen evolution was conducted at -100 mA for 2 min. The mass of the sample was measured before and after the water reduction using an analytical balance (Sartorius AG, Bp301S) to examine the weight loss during the test. The dendritic porous Cu sample mass was reduced by ~22% from the initial mass of 21.1 ± 0.1 mg to 16.3 ± 0.1 mg. A Cu residue could be observed at the bottom of the cell, indicating that the dendritic structure disintegrated during the experiment due to the hydrogen evolution reaction. This result shows the weak mechanical stability of the sample. Therefore, the porous Cu must be reinforced to be used as a substrate material for PEC water splitting application.

4.2 Reinforced porous Cu and free-standing porous Cu framework.

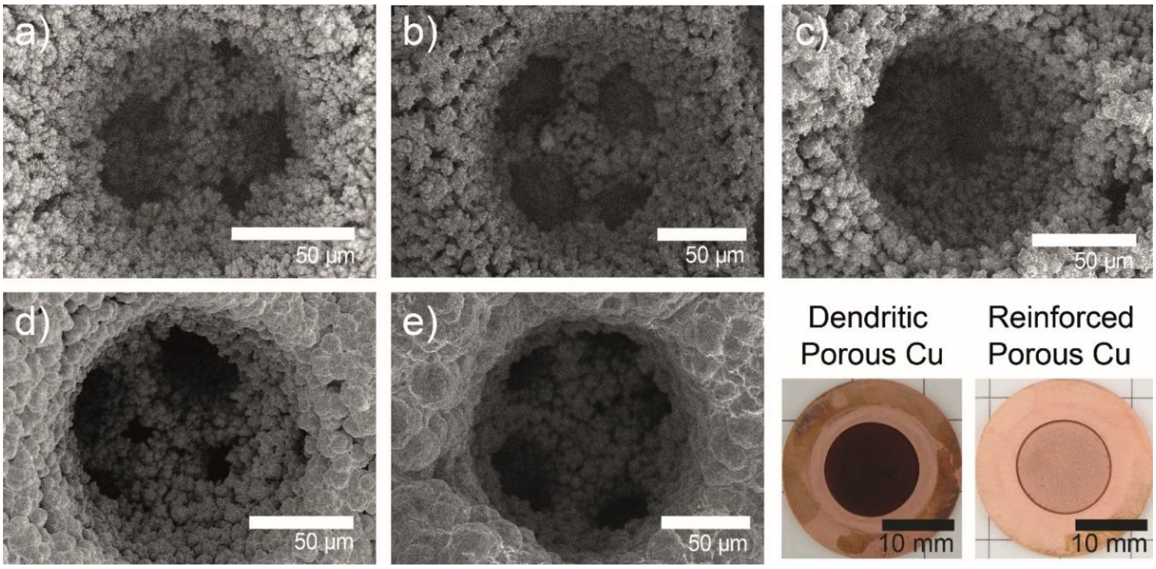

Figure 4–6 Reinforcement procedure of the dendritic porous Cu (deposited at 1.5 A cm^{-2} for 60 s) with a) no reinforcement b) 5 min, c) 30 min, d) 60 min, and e) 120 min Cu deposition time at current densities of -20 mA cm^{-2}. The photographs show the samples before and after the reinforcement procedure.

A second electrodeposition process was carried out to improve the mechanical stability of the dendritic porous Cu structure. The dendritic porous Cu sample deposited at -1.5 A cm^{-2} for 60 s was used as the template to study the reinforcement process. The small current density (-20 mA cm^{-2}) plays a vital role in significantly reducing hydrogen evolution, increasing the current efficiency for the Cu deposition, and enabling a homogenous deposition of a compact Cu layer. Thereby, the dendritic structure is slowly covered with Cu and becomes more compact with increasing deposition time (Figure 4–6 a-e).

This surface transformation also influences the color of the sample(Figure 4–6). Starting from 60 min of the reinforcement process, the top region of the pore wall becomes more compact as the gaps between the dendrites have decreased significantly. However, the bottom region within the pore reveals that it is still in the granular dendritic structure. For further investigation of the structural analysis, especially at the bottom part, the samples were cut, and a cross-sectional evaluation was carried out.

Figure 4–7a shows two different morphologies between the bottom region and top region of the porous layer. Despite the long duration of the reinforcement procedure, the bottom part of the sample still consists of dendrites. This might be caused by the low diffusion of the Cu ions to the small inner pores at the bottom region near the flat Cu substrate. The top part of the porous layer is more exposed to the electrolyte and therefore, is accessible to a higher concentration of Cu ions. Because most of the Cu ions are being reduced to Cu metal on the top region, the diffusion of the Cu ions to the inner pores becomes relatively low and could not replenish the depleted Cu ions resulting in no reinforcement of the dendrites even after a long electrodeposition time.

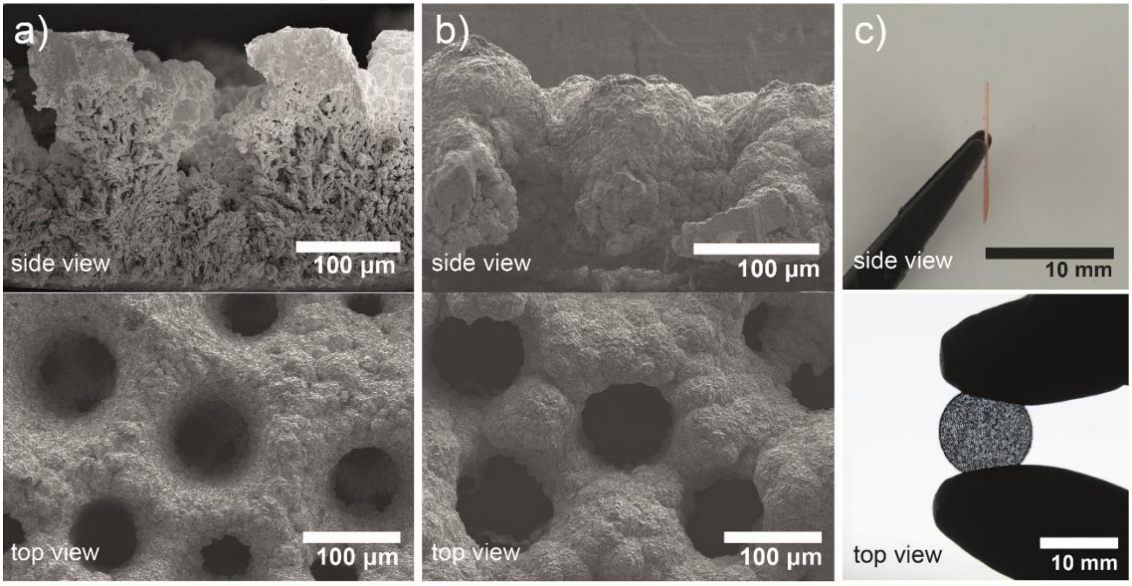

Figure 4–7 Morphological comparison of a) a substrate-bound and b) free-standing porous Cu frameworks electrodeposited at -1.5 A cm^{-2} for 60 s and reinforced at -20 mA cm^{-2} for 120 min (for detail see section 3.1.2). c) Sample photographs of the free-standing porous Cu. The top image shows the cross-section of the samples (side view), and the bottom part shows the surface morphology (top view)

On the other hand, the weak structural integrity at the bottom region allows the sample to be further developed to obtain a free-standing porous Cu framework. The reinforced porous layer was separated easily from the flat Cu substrate by using the ultrasonication method (see section 3.1.2). The weak and delicate dendritic structures disintegrated during the ultrasonic process, and the compact pore walls at the top region, which are more mechanically stable, can withstand the intense agitation in the ultrasonic bath. The interconnected pore tunnels that were observed previously at the interface between the porous Cu layer and the flat Cu substrate are also absent on the free-standing porous Cu (Figure 4–7a, and b).

The ultrasonic process successfully removed the dendritic Cu layer consisting of those interconnecting pore tunnels and created single through pores. The cross-section SEM images also reveal that the thickness of the porous Cu layer was reduced by ~32% (from ~250 µm for the substrate-bound sample to ~170 µm for the free-standing sample) after the lift-off procedure from the flat Cu substrate. The average diameter of the pore size was then estimated from the top-view SEM image of the free-standing porous Cu, which is between 60 µm and 110 µm.

By extending the reinforcement time up to 300 min (Figure 4–8a-d), there was no significant decrease in the size of the pores, which indicates that the deposition of Cu is predominantly occurring at the top surface. Moreover, the effortless separation of the porous Cu framework from the substrate by ultrasonication implies that the long reinforcement duration does not change the diffusion of the Cu ions into the interconnecting pore tunnels. The surface morphology varies significantly from 180 min reinforcement time, and a cauliflower-like structure can be observed from those samples.

The reinforcement procedure (section 3.1.2) was also implemented on various dendritic porous Cu samples that were deposited at -1.5 A cm^{-2} with shorter electrodeposition times between 2 and 30 s (Figure 4–4). In this case, the reinforcement time was set for 120 min. The samples deposited below 20 s could not be separated from the substrate by ultrasonication. This might be influenced by the relatively thin layer of the porous structure that allows the Cu ions to diffuse better into the inner pores and making a stronger adhesion with the flat Cu substrate. Starting from 30 s deposition time, the samples are relatively thicker and consist of the interconnecting pore tunnels which are still in the dendrites from after the reinforcement. Therefore, these samples can be easily separated from the flat Cu substrate by ultrasonication and form a free-standing porous Cu framework.

To determine the mechanical stability of the free-standing porous Cu during water splitting, the same hydrogen evolution experiment as explained in section 4.1 was conducted on the sample reinforced with 120 min. After 2 min, there were no traces of Cu residues, and the sample does not lose any mass. This improvement of the mechanical stability provides a stable surface to deposit photoactive material for the PEC water splitting application (see section 4.3).

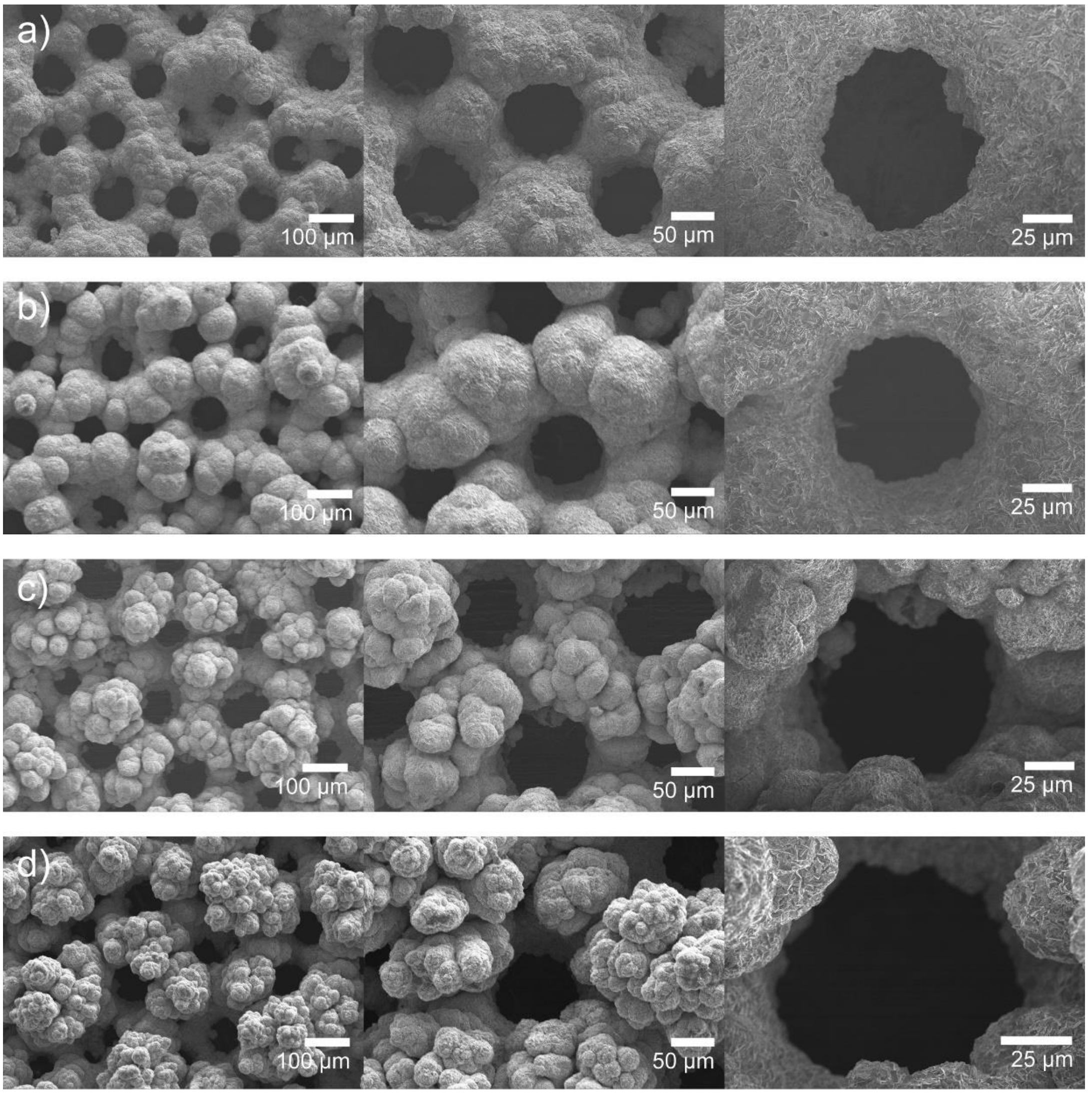

Figure 4–8 Reinforcement procedure of the dendritic porous Cu layer with a)120 min, b) 180 min, c) 240 min, and d) 300 min. Ultrasonication was performed on all samples to separate the porous layer from the flat Cu substrate.

4.3 Electrodeposition of Cu_2O film

Cyclic voltammetry (CV) measurement was carried out to analyze the electrochemical reactions occurring in the alkaline bath (pH ~12) and determine the reduction potential of Cu_2O. Figure 4–9 shows the cyclic voltammogram of the reinforced porous Cu substrate in the alkaline bath. The voltammogram shows two distinct reduction peaks located at potentials of -0.39 V vs. Ag/AgCl (sat. KCl) and -0.65 V vs. Ag/AgCl (sat. KCl), which belong to the reduction of the Cu ions to Cu_2O and Cu metal, respectively. It can be observed that the current density near the scanned potential of~-0.4 V vs. Ag/AgCl (sat. KCl) decreases significantly with the increasing cycle numbers, especially from the first cycle to the seventh cycle. The reaction seems to be saturated after the eighth cycle, which indicates a slower deposition rate. This behavior can be related to the semiconductor properties of the Cu_2O. The increasing thickness of the Cu_2O film lowers the sample conductivity and therefore slows down the electrodeposition rate.

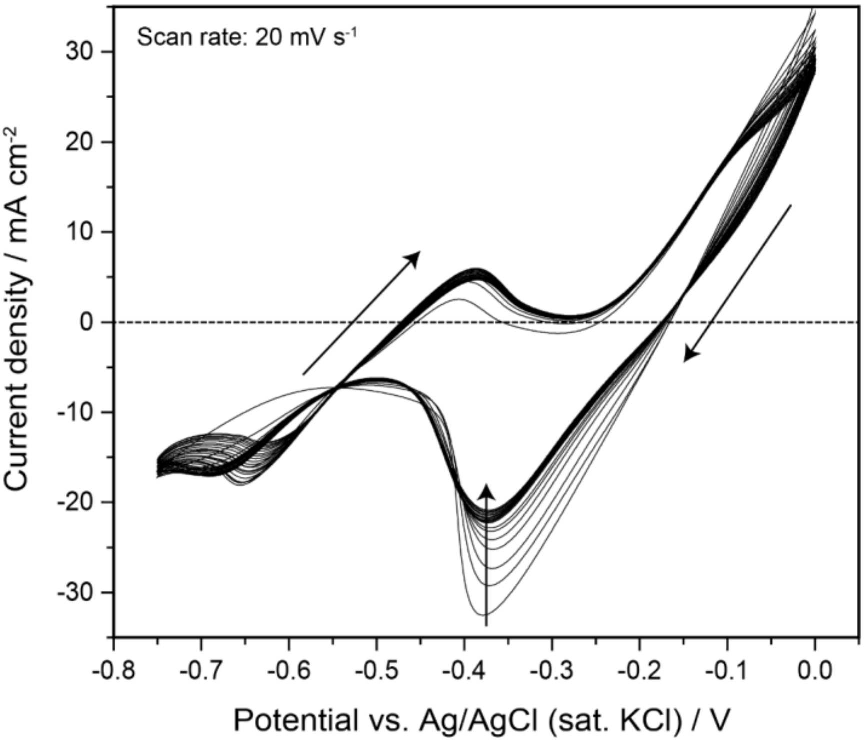

Figure 4–9 Cyclic voltammogram of the reinforced porous Cu substrate (at -1.5 A cm^{-2}, 60 s – reinforced for 120 min) in alkaline Cu bath (pH ~12) with constant bath temperature of 60°C recorded with a scan rate of 20 mV s^{-1} and 20 cycles. The arrow which points upward indicates the movement of the cathodic peak with increasing cycle number.

Two oxidation peaks were also visible in the voltammogram. The oxidation peak at -0.4 V vs. Ag/AgCl (sat. KCl) belong to the oxidation reaction of the Cu metal (Cu^0) to Cu^{1+}, whereas the oxidation peak after -0.1 V vs. Ag/AgCl (sat. KCl) refers to the further oxidation reaction of the Cu^{1+} to Cu^{2+} ions. The oxidation peak at -0.4 V vs. Ag/AgCl (sat. KCl) only appear when the reduction peak at -0.65 V vs. Ag/AgCl (sat. KCl) occurs. This was verified by stopping the scanned potential at -0.5 V vs. Ag/AgCl (sat. KCl) which shows no oxidation peaks. Based on the Nernst equation (Eq. 4), every change of the pH will shift the electrochemical potential by 59 mV. Therefore, it is essential to keep the pH of the alkaline bath constant. Evaporation of the electrolyte can change the Cu concentration and thus must be avoided. The electrodeposition potential of ~-0.4 V vs. Ag/AgCl (sat. KCl) at pH 12 provides a consistent and homogenous Cu_2O layer. Therefore, it will be used for all electrodeposition on various substrates.

4.3.1 Deposition of Cu_2O film on planar substrates

4.3.1.1 Growth mechanism of Cu_2O film

The electrodeposition of Cu_2O film on different planar surfaces was performed to study the effect of the substrate on the growth mechanism of the Cu_2O. The geometry of the planar substrates allows an accurate analysis of the crystal planes and orientations by XRD. The Cu_2O film was deposited on Au and Cu substrates with different crystalline properties. The planar Au substrate was prepared using thermal evaporation that deposits 200 nm of Au film on a Si wafer. The Si wafer was coated with 5 nm of Cr to improve the adhesion of the Au layer. This method is known to produce a preferred [111] oriented crystallite with a highly smooth surface[108]. On the other hand, the planar Cu substrate with a polycrystalline structure was obtained by cutting a high purity copper rod (99.9%) into a Cu coin with a diameter of 27 mm and a thickness of 2 mm. The crystal orientation and the facet of the Cu_2O crystal play an essential factor in improving the PEC water splitting performance[109].

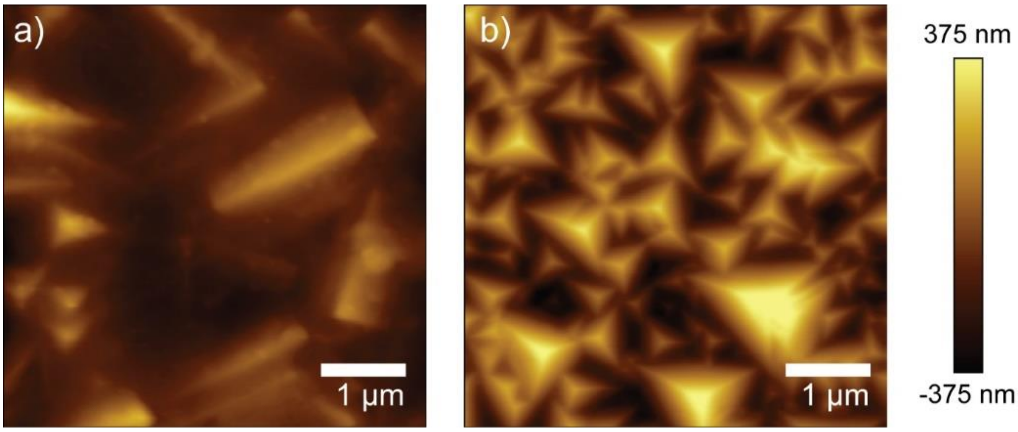

Figure 4–10 AFM images of electrodeposited Cu_2O film on a) flat Cu coin and b) 200 nm of Au plated Si wafer. The 200 nm Au layer was deposited on a Si wafer by a thermal evaporation method. The Cu_2O film on both substrates is electrodeposited at -0.4 V vs. Ag/AgCl (sat. KCl) in the alkaline Cu bath for 30 min with a constant bath temperature of 60°C.

The Cu_2O films were electrodeposited on the Au and Cu substrates for 30 min, using the same procedure described in section 3.2. Figure 4–10 shows the morphology of the deposited Cu_2O film on the two planar substrates. The Cu_2O grains on Cu offer different crystalline shapes and sizes than the deposited Cu_2O on the Au. A large Cu_2O crystal that consists of a triangular prism shape (see section 2.3 and Figure 2–6) with a grain size of ~2 µm can be clearly observed from the sample on the Cu substrate (Figure 4–10a). In contrast, the Cu_2O crystals on the Au substrate are made of a three-sided pyramidal structure typical for the Cu_2O crystal grown in [111] direction. The size of the grains varied widely between ~300 nm and ~1 µm for the sample on the Au substrate. This variation might be influenced by the grain size of Au, which affects the nucleation and generates an epitaxial growth of the Cu_2O crystals. From the AFM analysis, the root mean square roughness, was 98 and 144 nm for the Cu and Au substrates, respectively.

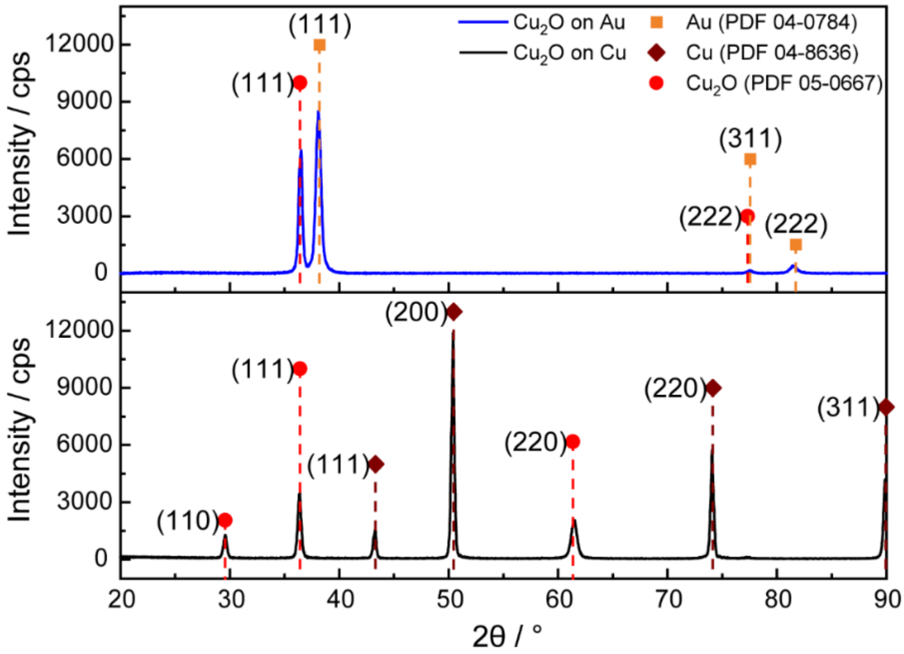

Figure 4–11 X-ray diffractogram of the electrodeposited Cu_2O film on planar Au and Cu substrates. The Cu2O film was electrodeposited at -0.4 V vs. Ag/AgCl (sat. KCl) in an alkaline Cu bath for 30 min on both substrates. All XRD patterns undergo the Kα2 removal process using the Diffrac evaluation software from Bruker.

Figure 4–11 shows the XRD patterns of the deposited Cu_2O on Au and Cu substrates. The composition and the crystalline phase of the materials were obtained by identifying the peak positions on the XRD patterns and indexing them using the international center for diffraction data (ICDD) database. The sample deposited on the Au substrates shows four reflections that belong to the crystal planes of Cu_2O and Au. Three crystal planes of (111), (311), and (222) were identified for the Au, whereas the Cu_2O showed only one (111) peak. Two dominant peaks can be observed, which belong to the (111) planes for both the Cu_2O and Au. The absence of other crystal planes with different (hkl) reflections for both the Au and Cu_2O suggests that the film is grown in a single preferred orientation [111]. This result agrees with the morphology of the Cu_2O crystal on Au (Figure 4.10b), revealing three-sided pyramidal features typical for a cubic lattice with [111] growth direction.

The Cu_2O on Cu, on the other hand, shows a polycrystalline structure. The Cu substrate shows four reflections which belong to the (111), (200), (220), and (311) planes, whereas the Cu_2O has only three peaks which index to the (110), (111), and (220) planes. Although the peak for the (200) plane of the Cu was more dominant, no traces of the (200) plane of the Cu_2O are visible. This behavior is likely due to the influence of the pH of the alkaline copper bath. Some reports show that the Cu_2O film deposited at higher pH (>10) produces Cu_2O with preferred crystal orientation of [111] and [110], whereas, at lower pH <~9, the crystal was dominated with [100] crystal orientation [76]. The formation of [100] oriented crystals was likely suppressed at higher pH due to the different surface charges due to the low absorption of the hydroxide ions and kinetics [110–114]. Nevertheless, the crystalline structure of the substrate shows a substantial impact on the growth direction between the [111] and [110] when deposited at the same high alkalinity bath. Therefore, it is also essential to modify the substrates' crystalline structure to tune the growth orientation of the Cu_2O film.

To tune the crystal orientation of the deposited Cu_2O, a capping agent such as HMT is added to the alkaline copper electrolyte. The influence of this capping agent was investigated by changing the concentrations of HMT in the electrolyte to produce different Cu_2O samples on a planar Cu substrate. The report by Marimon et al [104] shows that based on the RTC values, the texture changed significantly from previously more dominant [110] to the [100] orientation at higher HMT concentration. The RTC value of [110] decreases about ~24 % while the [100] increases up to~38 % with 860 mM HMT. The [111] orientation was affected by the high concentration of HMT, which reduces the RTC value from 14 to 4 %. However, due to the inconsistent preferred orientation of the polycrystalline structure of the planar Cu substrate, it was challenging to clearly determine the influence of HMT, especially at the lower concentration on the phase transition between the [110] and [111] orientation. The significant transition of the crystal orientation with a high concentration of HMT shows that the capping agent can assist the electrodeposition process and control the crystal orientation of the Cu_2O film without changing the crystalline properties of the substrate or altering the pH of the bath.

4.3.1.2 Thickness evaluation of the Cu_2O film

The electrodeposition method allows control of the Cu_2O film thickness by adjusting the deposition time. The thickness of the electrodeposited Cu_2O can be evaluated from the total charge obtained during the deposition process. Samples with different thicknesses were deposited on planar Cu substrates, with a geometric area of 1 cm^2. The total charge was extracted by applying an integral to the current transient curve using the EC lab software. At least three samples were evaluated for each deposition time to obtain an accurate analysis of the thickness (error bar shown in Figure 4–12). The mass was calculated from the total charge using the Faraday equation (Eq. 28), where n is 2 (number of electrons needed for the reaction). The current efficiency for the electrodeposition of Cu_2O in the alkaline electrolyte is 100 %, according to Eskhult et al. [36]. The calculated mass was then divided by the Cu_2O density (6 g cm^{-3}) and the geometric surface area to obtain the thickness of the Cu_2O films.

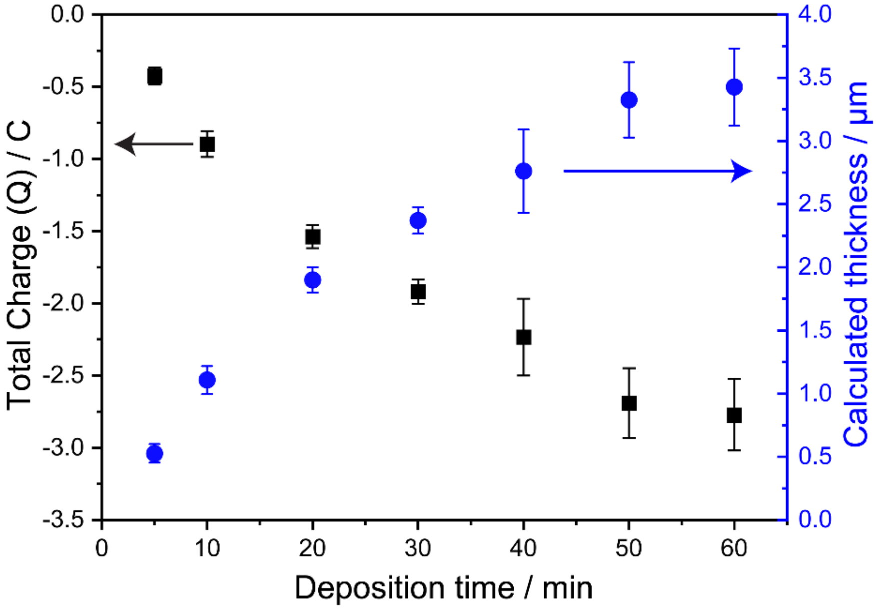

Figure 4–12 Estimated Cu_2O film thickness using Faraday law with 100 % current efficiency from the total charge obtained at different deposition times. The mass of the deposited Cu_2O is calculated using the Faraday equation (Eq. 28).

Figure 4–12 shows that the thickness of the deposited Cu_2O films increases with the deposition time. Significant thickness variation can be observed, especially for shorter deposition (5- 20 min). After 30 min, the film thickness increases at a slower rate and reaches a plateau at a deposition time of 50 min. To further evaluate the thickness of the Cu_2O film, a cross-sectional SEM analysis was performed on the samples deposited at 5, 30, and 60 min (Figure 4–13).

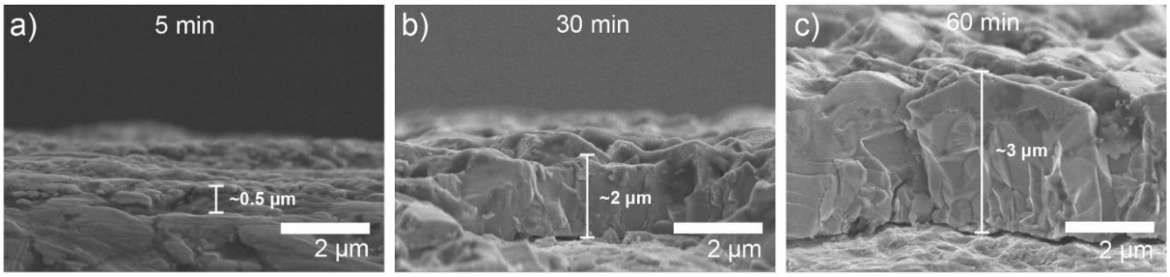

Figure 4–13 Thickness comparison of the electrodeposited Cu_2O film on flat Cu substrates with deposition time of a) 5 min, b) 30 min, and c) 60 min. These samples were deposited at -0.4 V vs. Ag/AgCl (sat. KCl) in the alkaline copper bath with a constant bath temperature of 60°C. The samples were cut using a sharp hand lever scissor.

The cross-sectional analysis shows that the Cu_2O film increases from ~0.5 to ~3 µm for the samples deposited between 5 min and 60 min, which is similar to the calculated thickness from the total charge (Figure 4–12). The thickness of the Cu_2O samples deposited between 5 and 30 min increases about four times, whereas after 30 min deposition time, the thickness change becomes less significant. The slight increase of the thickness with a longer deposition time is correlated to the potentiostatic electrodeposition method and properties of Cu_2O as a semiconductor. The conductivity of the Cu_2O film decreases as the thickness of the film increases, limiting the electron transport to the surface and slowing down the electrodeposition process.

4.3.2 Cu_2O on porous Cu frameworks

The photoactive Cu_2O layer was electrodeposited on various porous Cu frameworks (dendritic porous Cu (-1.5 mA cm^{-2}, 60 s), reinforced substrate-bound porous Cu, and free-standing porous Cu) using the deposition parameters discussed in sections 3.2 and 4.3. The chronoamperometric curves (Figure 4–14) were normalized by the geometric surface area of 1 cm^2. The current densities represent the growth rates of the Cu_2O film, and the thickness determination discussed in section 4.3.1. The electrodeposition process begins with the nucleation of the Cu_2O crystals on the conductive Cu surface and is followed by the crystal growth to form a film layer that covers the whole substrate. The current transient for the deposition on a pristine Cu surface usually starts with a high value of the current density that slowly decreases over time as the surface becomes gradually covered with the less conductive Cu_2O layer. However, the current transient curves of the dendritic porous Cu and the reinforced substrate-bound porous Cu in Figure 4–14a reveal a similar behavior, which reaches a plateau after 15 s.

The dendritic porous Cu in its non-reinforced form consists of a ramified structure with a large surface area, leading to current densities in the range of -18 to -14 mA cm^{-2} after 15 s. On the other hand, the reinforced substrate-bound porous Cu is more compact, particularly at the top region, and has a considerably smaller surface area (Figure 4–6e), resulting in current densities in the range of -6 to – 4 mA cm^{-2}. For both the dendritic porous Cu and the substrate-bound porous Cu, the low diffusion of the Cu ions through the ramified structure and the interconnecting pore networks (section 4.2), might be the limiting factor in the deposition process.

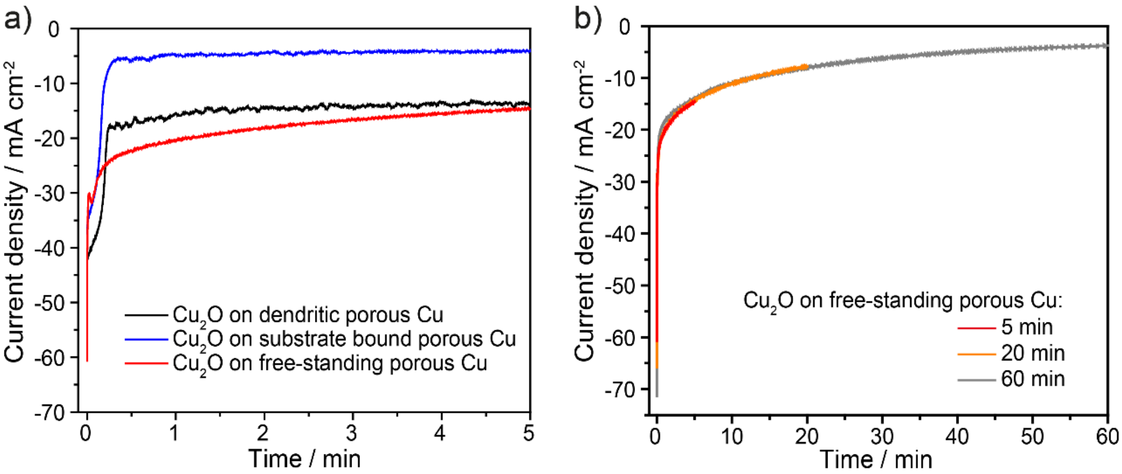

Figure 4–14 Current transients of a) Cu_2O film electrodeposited on different substrates and b) Cu_2O film on free-standing porous Cu substrates at different deposition times. The blue and black curves represent the Cu_2O on the dendritic porous Cu and reinforced substrate-bound porous Cu substrates, respectively. The red, yellow, and grey curves correspond to the Cu_2O on free-standing porous Cu substrates. All samples were electrodeposited at -0.4 V vs. Ag/AgCl (sat. KCl) in the alkaline copper bath.

Aside from the other two substrates, the free-standing porous Cu, which is reinforced and completely separated from the flat Cu substrate, was exposed to the electrolyte from the front and backside. This configuration makes the whole surface, including the inner part of the pores, more accessible, resulting in even higher deposition currents than from the dendritic porous Cu substrate (Figure 4–14b). The current densities of all the deposited samples have a similar trend indicating good reproducibility for the preparation of the porous substrates. The current densities increase rapidly at the initial stage and then decrease at a slower rate over a long deposition time scale.

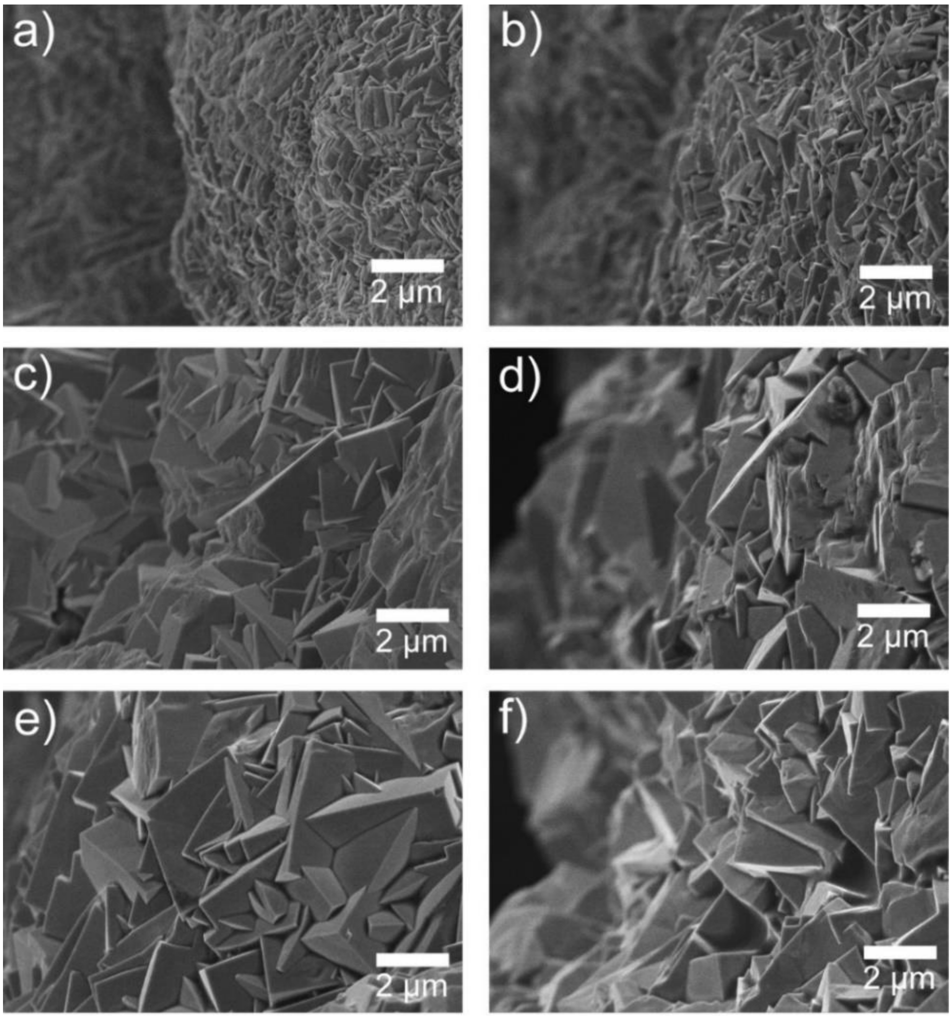

Figure 4–15 Surface morphology comparison of Cu_2O films electrodeposited potentiostatically at -0.4 V vs. Ag/AgCl (sat. KCl) on the free-standing porous Cu framework for of a) 5, b) 10, c) 20, d) 30, e) 40, and f) 60 min deposition time in a Cu citrate bath (pH 12).

It can be observed in Figure 4–15a-f that the grains of the Cu_2O on the free-standing porous Cu surface grow larger with increasing deposition time. The SEM micrograph of the 5 min deposited samples (Figure 4–15a) shows a thin layer of small Cu_2O grains with sizes between 500 and 800 nm. The crystals grow to about 1-1.5 µm after 10 min and increase further to 2-4 µm at a longer deposition time. However, after 20 min, no significant change in the grain size could be observed. This behavior could be linked to the current transient curve of the Cu_2O in Figure 4–14b, which shows that the current density decreases at a much slower rate after 20 min deposition time due to the increasing resistance of Cu_2O film. This behavior indicates that the layer morphology and the electro crystallization process were strongly influenced by the deposition time.

The thickness of these layers could not be determined directly due to the complex morphology of the porous structure. As an alternative, indirect estimation of the layer thickness is taken here. Since a potentiostatic electrodeposition method is used to deposit the Cu_2O on the free-standing porous Cu framework, the upper limit of the achievable layer thickness can be expected from the planar Cu_2O samples (see section 4.3.1), which was deposited using the same deposition configuration and parameters. The thickness estimation using the total charge could not be realized due to the undetermined total surface area of the porous structure.

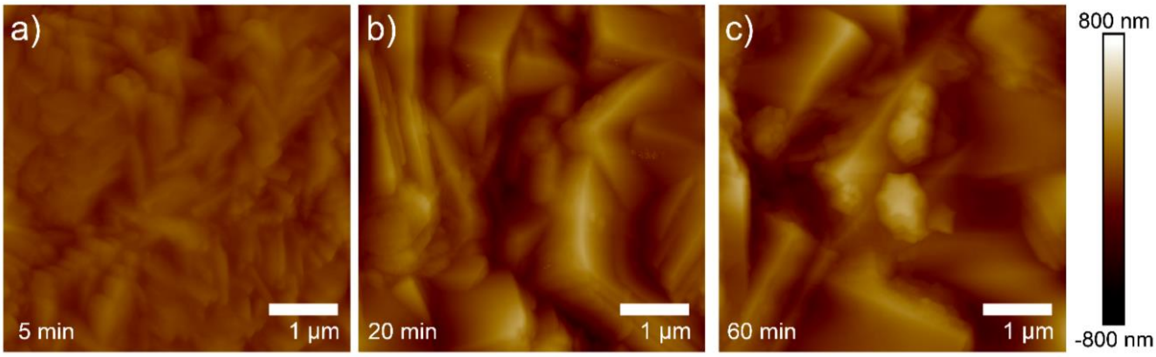

Figure 4–16 High magnification AFM images of Cu_2O film deposited on free-standing porous Cu for a) 5 min, b) 20 min, and c) 60 min with surface roughness Sq of 53.2 nm, 149 nm, and 165 nm, respectively.

From the cross-sectional SEM analysis, the thickness of the sample with 5-, 30-, and 60-min deposition time will not exceed ~0.5, ~2, and ~3 µm, respectively. Figure 4–16 shows high magnification AFM images of the Cu_2O film deposited at 5, 20, and 60 min. The root mean squared roughness of the free-standing porous Cu_2O frameworks is 53.2, 149, and 165 nm 5-,20-and 60- min deposition time, respectively. From these roughness values, the surface area is estimated to have an increase of 17 % (5 min), 35.7 % (20 min), and 41.3 % (60 min). The longer deposition time generates more significant surface roughness which is influenced by the grain size of the Cu_2O crystal. After 20 min of deposition time, the change of the surface roughness becomes less significant.

Figure 4–17 shows the XRD patterns of the Cu_2O samples deposited at different deposition times. The diffraction peaks can be assigned to bulk Cu_2O (JCPSDS 01-077-0199), with the most intense peaks indexed for the (111) plane, followed by the (220) and (200) planes. The crystal planes of (111), (200), (220), and (311) from the porous Cu substrate (JCPDS 01-085-1326) were also present in the XRD patterns.

The 5-min deposited sample exhibits five noticeable (hkl) reflections. The small peak at 36.4°is identified as the Cu_2O (111) plane, and the four remaining peaks belong to Cu substrate with the two most dominant peaks indexed as (111) and (200). As the deposition time increases (20-min and 60-min samples), new peaks that were identified for the Cu_2O (200) and (220) planes have emerged. Moreover, the peak intensity of the Cu_2O (111) planes has increased significantly while the intensity of the Cu (111) gradually decreases. This change of the intensity is likely due to the increasing Cu_2O layer thickness. The full-width at half maximum (FWHM) of the (111) peak, which belongs to the 5-,20-, and 60 min samples, decreases progressively from 0.44 to 0.41° and finally 0.35°, respectively. The crystallite size was estimated to be 22, 24, and 28 nm using the Scherrer equation [115].

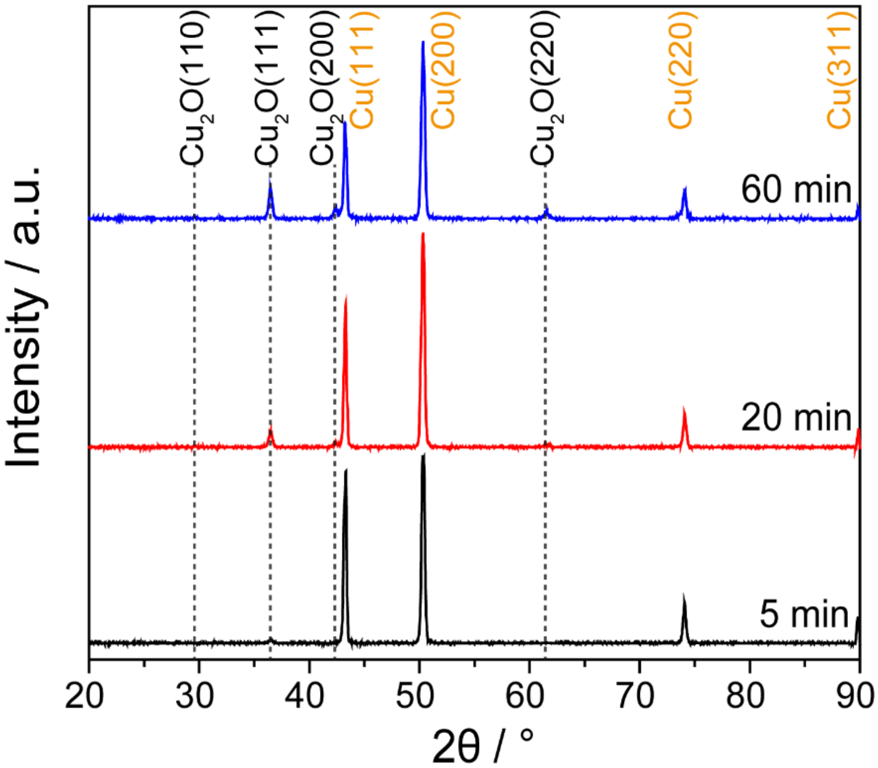

Figure 4–17 XRD patterns of Cu_2O films deposited on free-standing porous frameworks at different deposition times. All patterns underwent the Kα2 removal process using the Diffrac evaluation software from Bruker. The identified crystal plane for both Cu_2O and Cu is placed in the graph with the text color of black and yellow, respectively.

The investigated samples do not show any reflections for cupric oxide (CuO), thus confirming the suitability of the electrodeposition method for producing pure Cu_2O layers. Unfortunately, due to the complex structure of the porous structure, the preferred orientation of the Cu_2O crystals could not be determined. The XRD was performed with the Bragg-Brentano configuration, which extracts the crystal plane's information parallel to a planar surface. The free-standing porous Cu_2O samples, however, consist of not only the planar surface on top but also tilted and vertical surfaces at the inner pore walls. As a result, the samples exhibit a powder-like behavior not because of the intrinsic different crystal plane orientations but due to the morphology of the porous Cu framework, which makes the quantitative determination of the crystal growth orientation of the Cu_2O rather challenging. An indirect correlation of the crystal orientations on the PEC performance for this porous Cu substrate was reported by Marimon et.al [104].

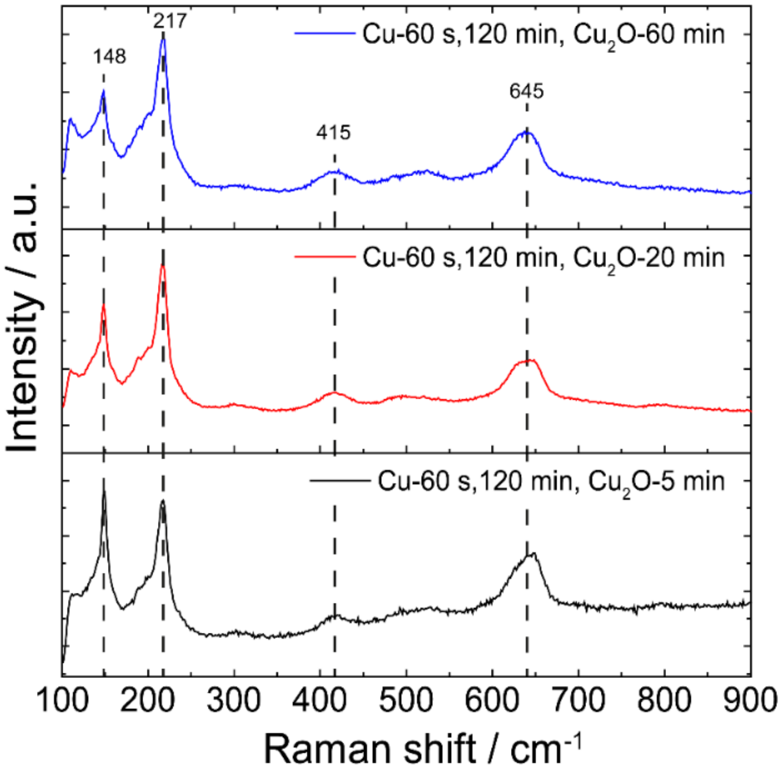

Figure 4–18 Raman spectra of Cu_2O film on free-standing porous Cu frameworks deposited at different durations. the peak positions are placed at the top part of the graph.

The material composition of the samples was further confirmed by Raman spectroscopy. A Cu_2O crystal has a cubic lattice that consists of six atoms in a primitive unit cell and belongs to the Pn-3m space group. Based on this structure, it possesses fifteen optical phonon vibrations that are grouped into six different modes at the Brillouin zone center, which are classified in Eq. 29.

$$\Gamma = T_{2g} + 2T_{1u} + T_{2u} + E_u + A_{2u} \tag{29}$$

Or alternatively described in other literature as Eq. 30.

$$\Gamma = {}^{3}\Gamma'_{25} + 2\,{}^{3}\Gamma_{15} + {}^{3}\Gamma_{25} + {}^{2}\Gamma_{12} + {}^{1}\Gamma_{2} \qquad (30)$$

The phonon mode of T_{2g} is Raman active, and the two T_{1u} phonon modes are infrared (IR) active. In a perfect Cu_2O crystal, these modes should be present while the other phonon modes (T_{2u}, E_u, and A_{2u}) are silent. However, the non-stoichiometric Cu_2O crystal defects such as vacancies may activate the silent modes together with the forbidden phonon modes, which have been reported in the literature [103, 116–118]. Additionally, multi-phonon processes can also be present in the Raman spectra of a Cu_2O crystal [119].

Figure 4–18 shows the Raman spectra of the Cu_2O films on the free-standing porous Cu frameworks for different deposition times. Several prominent Raman peaks which belong to the Cu_2O crystal at 148, 218, 412, and 645 cm^{-1} are present for all the samples. The peaks at 148 and 645 cm^{-1} are assigned to the two T_{1u} phonon modes which are IR active [120]. The intense peak at 217 cm^{-1} and the broad peak at 412 cm^{-1} belong to the second-order Raman active overtones of $2E_u$ [121, 122] and the multi-phonon process ($3E_u$+T_{2u}) [123], respectively. For the 5- and 60-min samples, a small bump at 520 cm^{-1} is also visible which belongs to the Raman active mode of T_{2g}.

The intensity at 148 cm^{-1} is gradually decreasing with increasing deposition time, and the peak at 109 cm^{-1} has also slowly become more visible. A report made by Powell et al. shows that the peak at 148 cm^{-1} increases significantly after inducing the Cu_2O crystal with ion implantation [124]. The external ion caused damage in the crystal lattice and triggered the relaxation of symmetry selection rules or lattice symmetry breakdown, increasing the intensity of the Raman spectra at 148 cm^{-1}. In our case, the increasing peak intensity at 148 cm^{-1} is likely influenced by the defects such as copper vacancies or oxygen vacancies [117, 123, 125, 126] in the crystal lattice during the electrodeposition process.

The peak at 148 cm^{-1} of the 20-and 60-min samples has similar and relatively low intensity while the 5-min sample has the highest intensity. This variation in the intensities shows that a shorter deposition time (5 min-sample) is expected to create a higher number of defects in the crystal lattice. The existence of these defects is related to the increase of the hole concentration of the Cu_2O samples will be shown in the flat band potential

-Schottky analysis (section 4.5). Figure 4–19 shows the photoluminescence spectra of the free-standing Cu_2O framework deposited at different durations. All spectra of the samples show very similar characteristics, with the peaks of the emission band centered at a photon energy of 1.45 eV. A tiny peak can also be detected at the emission band of 2 eV, which belongs to the direct bandgap luminescence of the Cu_2O.

The broad peaks located between the photon energy of 1.2 eV and 1.8 eV are probably comprised of several emission bands due to the combination of different types of defects in the crystal lattice. Several publications have reported that the region of the relax excitons for oxygen and copper vacancies is located between ~1.05 eV and ~1.96 eV [127, 128]. The emission bands triggered by the copper vacancies usually appear at photon energy below 1.52 eV. In comparison, the bands caused by the oxygen vacancies occur at higher photon energies between 1.72 eV and 1.96 eV [128].

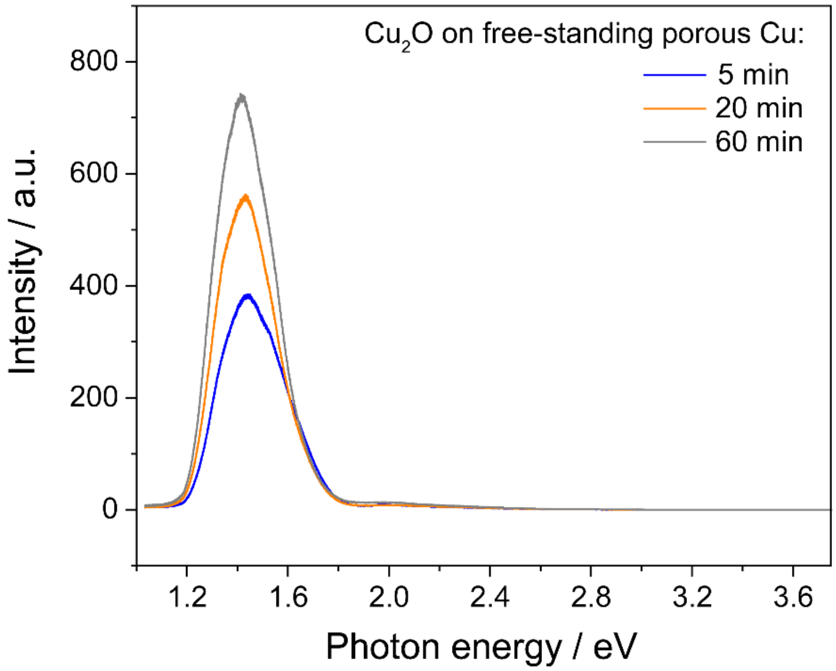

Figure 4–19 Photoluminescence spectra of the Cu_2O on free-standing porous Cu frameworks. The blue, yellow, and grey curves belong to the free-standing porous Cu_2O samples electrodeposited at -0.4 V vs. Ag/AgCl (sat. KCl) in an alkaline copper bath for 5, 20, and 60 min, respectively.

The highest peak located at 1.45 eV for all samples is most likely due to the recombination of bound excitons at the copper vacancies(V_{Cu}) [113]. The stable position of the peak indicates that all Cu_2O on the free-standing porous Cu samples have a similar type of defects in their crystal lattice. It can also be observed that the luminescence intensity of the samples increases with increasing deposition time. This characteristic is probably triggered by the different Cu_2O film thicknesses obtained at different durations (see above and section 4.3.1).

The electrodeposited Cu_2O films have been reported to have many defects [122, 129, 130]. The ratio between copper and oxygen vacancies varies significantly depending on the electrodeposition parameters such as the pH and the bath temperature. In this work, the electrolyte and all the electrodeposition parameters, besides the deposition time, were kept constant, and therefore, the same crystal quality could be preserved.

4.4 Optical characterization of the Cu_2O on the porous Cu frameworks.

The diffuse reflectance of the 5-min sample shows a different characteristic compared to the other two samples that were electrodeposited with 20 and 60 min (Figure 4–20a). This behavior is likely triggered by the different thicknesses of the Cu_2O films that affect the light absorption. The 5-min Cu_2O sample has a thickness of ~500 nm (see section 4.3). This relatively thin layer allows the light to pass through the whole film and be absorbed by the Cu substrate. Cu metal is known to absorb the light in the green and blue region (2.19 eV-2.75 eV), giving its red-orange color[131]. The influence of the Cu substrate can be seen in the reflectance spectrum of the 5-min sample, which shows two different slopes located between the photon energy of ~2 eV and ~2.6 eV. On the other hand, the 20- and 60- min Cu_2O samples with film thicknesses of ~2 µm and ~3 µm, respectively, possess only one slope between ~2 eV and ~2.2 eV. Furthermore, the % reflectance of the 20- and 60-min samples is much lower than the 5-min sample, implying that more light is absorbed in the thicker Cu_2O film.

The optical bandgap energies of the different Cu_2O samples were determined using the Kubelka-Munk function (Eq. 24) with the diffuse reflectance data to obtain the Kubelka-Munk absorption coefficient. The Tauc plot was then constructed based on the correlation between the Kubelka-Munk absorption coefficient and the photon energy (Figure 4–20b), which enabled the extrapolation of the linear region to the abscissa to estimate the bandgap energies (see section 3.3.3).

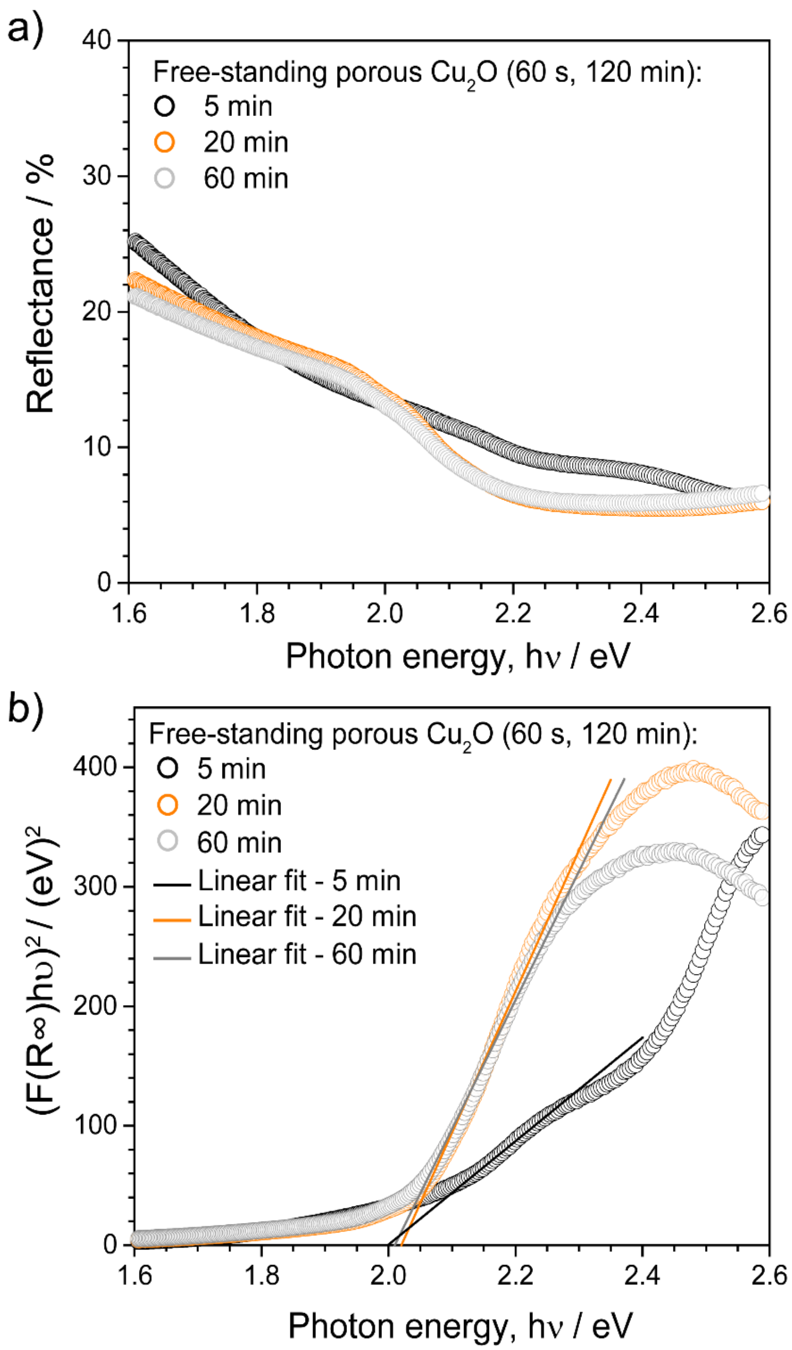

Figure 4–20 Optical characterization using a) UV-Vis diffuse reflectance spectra and b) Tauc plot with the Kubelka-Munk function of the free-standing porous Cu_2O samples with different deposition times. The black, yellow, and grey symbols represent the free-standing porous Cu_2O samples electrodeposited at -0.4 V vs. Ag/AgCl (sat. KCl) in the alkaline copper bath for 5, 20, and 60 min, respectively.

Both the 20- and 60-min Cu_2O samples have one noticeable slope, which lies almost at the same position, while the 5-min sample has two slopes. Similar to the reflectance result, the steep slope at the higher photon energy of the 5-min sample is likely due to the influence of both the translucent thin Cu_2O film and the absorption of the light by the Cu substrate. The extrapolation of the linear fit to the abscissa reveals that all the free-standing porous Cu_2O samples have nearly identical bandgap energies of ~2 eV, which agrees with the literature [132]. This result is to be expected as the Cu_2O samples were prepared using the same electrolyte and deposition parameters such as the pH, bath temperature, and the applied voltage.

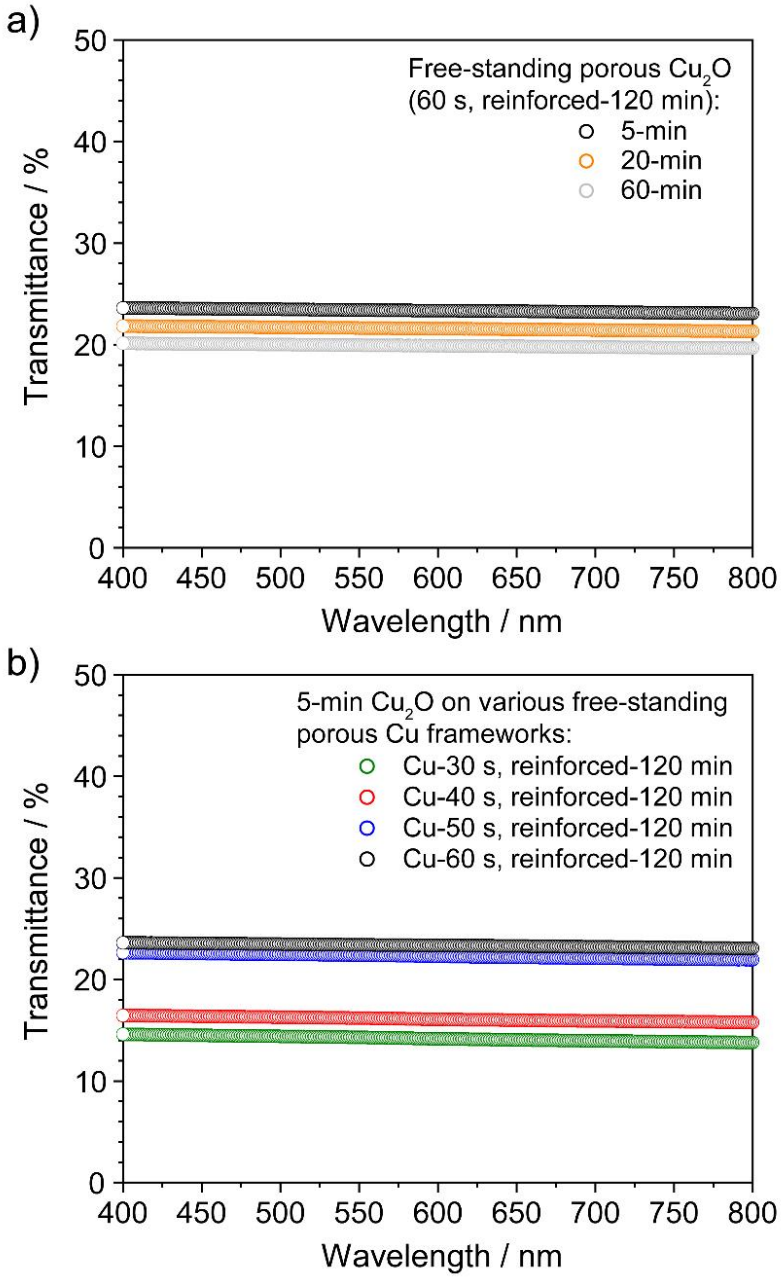

Figure 4–21 Transmittance spectra of a) electrodeposited Cu_2O films on a free-standing porous Cu framework ($-1.5\ A\ cm^{-2}$ for 60 s and reinforced at $20\ mA\ cm^{-2}$ for 120 min) with different durations and b) 5-min Cu_2O film on various free-standing porous Cu samples with different pore sizes. The black, yellow, and grey symbols belong to the Cu_2O samples deposited at -0.4 V vs. Ag/AgCl (sat. KCl) for 5, 20, and 60 min, respectively, on a free-standing porous Cu framework. The green, red and blue symbols belong to the Cu_2O samples deposited for 5 min on various free-standing porous Cu deposited at $-1.5\ A\ cm^{-2}$ for 30, 40, and 50 s, respectively.

The transmission spectroscopy was performed on the various free-standing porous Cu_2O samples to investigate the porosity of the porous structure. In this case, the light can be fully transmitted due to the through pores Cu. Figure 4–21a shows the transmission spectra of the Cu_2O film on the free-standing porous Cu samples deposited at different durations. The free-standing porous Cu frameworks were fabricated using the same electrodeposition parameters and deposition time (-1.5 A cm^{-2} for 60 s and further reinforced at 20 mA cm^{-2} for 120 min) and therefore is expected to have a similar structure. The 5-min deposited sample has the highest overall transmittance of ~23 %, and as the deposition time increases to 20- and 60-min, the transmittance slightly reduces to ~21 and ~20 %, respectively. The decrease in the transmittance is caused by the increasing Cu_2O film thickness described in the previous sections. The thicker Cu_2O film reduces the inner pores and thus decreases the transmittance.

Various free-standing porous Cu substrates were fabricated to investigate the influence of the pore size on the transmittance. The pore size of the porous Cu frameworks can be tuned by adjusting the deposition time during the fabrication of the dendritic porous Cu structure (section 3.1.1). After 30 s of deposition time, the porous Cu can be separated from the flat Cu substrate and form a free-standing porous Cu framework. Figure 4–21b shows the different transmission spectra of the Cu_2O film electrodeposited for 5 min on various free-standing porous Cu frameworks with varying pore sizes. The short deposition time of 30 s has low transmittance of ~14 %, and the value increases to 16, 22, and 23 % for the sample deposited with 40, 50, and 60 s, respectively.

This trend indicates that as the deposition time for the dendritic porous Cu increases, the pore size becomes larger and increases transmittance. The transmittance data can be directly correlated to the porosity due to the through-pores structure. The tunable transmittance features allow the porous samples to be used in a tandem system. The porous Cu_2O samples that are used as the photocathode can be placed in front of a photoanode that can harvest the transmitted light in a full cell configuration or dual photocathode configuration, as reported by Niu et al. [133].

4.5 Determination of flat band potential and charge carrier density by Mott-Schottky analysis

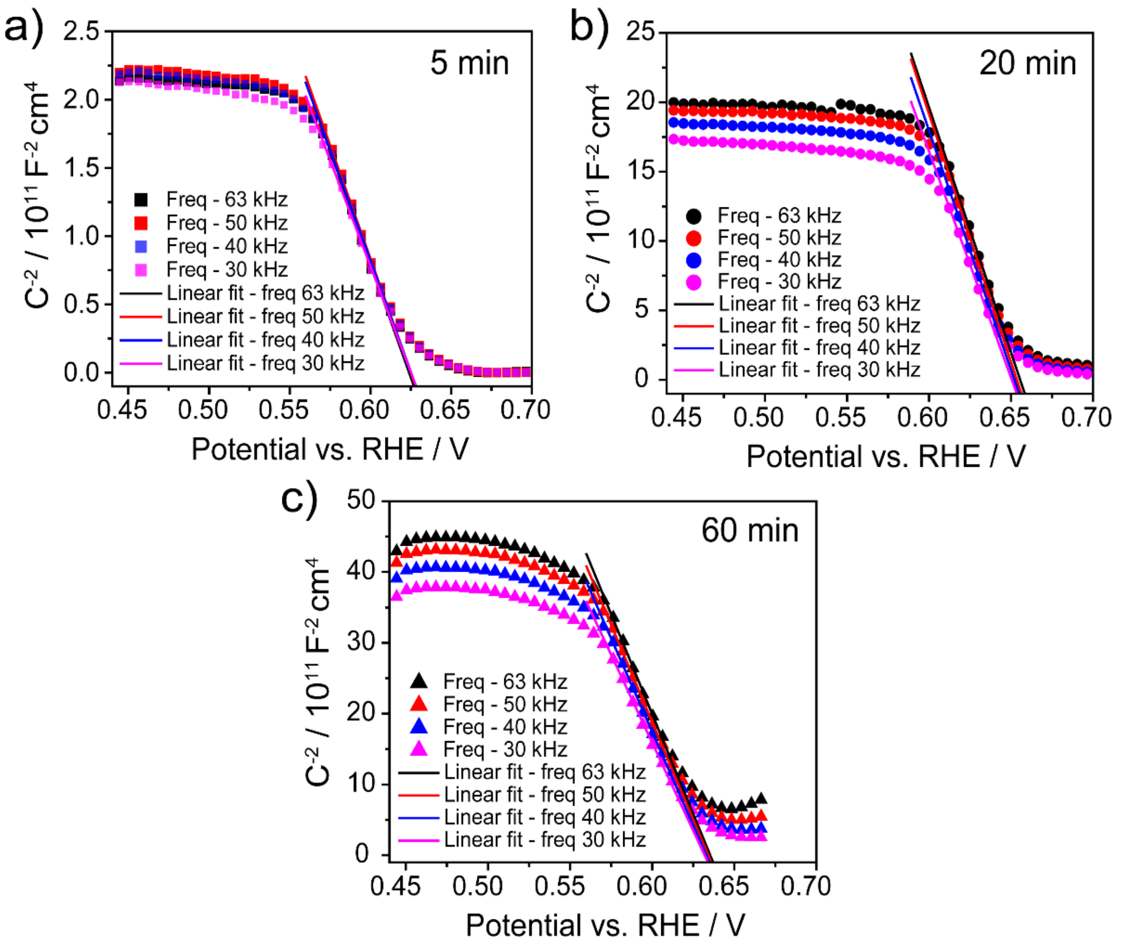

Figure 4–22 Mott-Schottky plots of deposited Cu_2O films on free-standing porous Cu framework (dendritic porous Cu deposition for 60 s and reinforced with 120 min) for a) 5, b) 20, and c) 60 min deposition time at various frequencies in 0.5 M Na_2SO_4 (pH ~6).

Mott-Schottky (MS) analysis was conducted at 30, 40, 50, and 63 kHz to determine the flat-band potential and the charge carrier density of the free-standing porous Cu_2O samples that were electrodeposited for 5, 20, and 60 min. The MS plots shown in Figure 4.22 confirmed that the deposited Cu_2O film is a p-type semiconductor due to the negative slope between the high plateau (depletion region) and low plateau (accumulation region) of the plots. At the various frequency range, the Mott-Schottky plot for each Cu_2O sample lies at almost the same position, which indicates the measurement range is stable and no indication of the influence of double-layer capacitance. The squared reciprocal of space charge capacitance (C^{-2}) for the Cu_2O samples becomes larger as the electrodeposition time increases, which might be related to the charge carrier densities. It has been reported that a small value of C^{-2} provides a higher charge carrier density [134, 135].

The flat-band potential and the hole concentrations (Figure 4–23) were extracted using Eq. 26 in section 3.3.4. The average flat-band potential lies between ~0.625 ± 0.002 V vs. RHE for the 5-min sample and ~0.65 V ± 0.005 vs. RHE for the 60-min sample, as was shown in Figure 4–23a, which is in agreement with the reported values (~0.65 V vs. RHE) of highly catalytic Cu_2O nanowires [29]. With the bandgap energies of 2 eV(Figure 4–20b), these potential values placed the conduction band edge of the electrodeposited Cu_2O film at approximately ~-0.75 ± 0.15 V more negative than the HER potential.

The overall surface area of the Cu_2O samples should be measured to determine the charge carrier density accurately. Unfortunately, due to the limitation of the experimental procedure, the overall surface area of the free-standing Cu_2O frameworks could not be determined. Therefore, an indirect approach is taken here to estimate the change of the surface areas of the Cu_2O samples by using the roughness increase due to the different crystal grains and include it in the calculation. The free-standing porous Cu frameworks were deposited using the same electrodeposition parameters, and they are expected to have the same structures. This can be concluded from the chronoamperometric curve in Figure 4–14b, which shows overlapping reproducible current transients suggesting that the surface area of all underlying porous Cu substrates is similar.

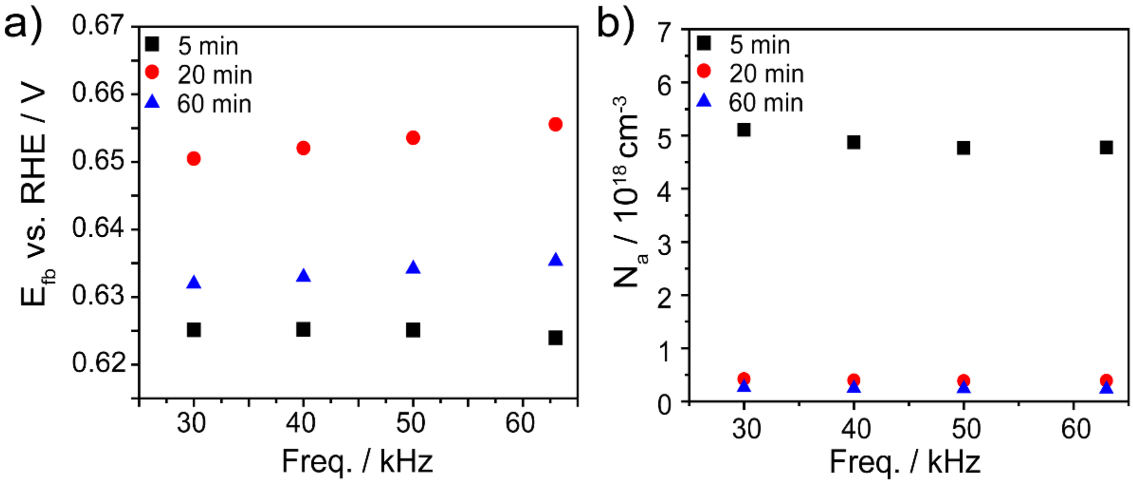

Figure 4–23 Evaluation of a) the flat-band potential (E_{fb}) and b) the hole concentrations (N_a) from the Mott-Schottky plots at different frequencies. The black square, red circle, and blue triangle represent the free-standing porous Cu2O sample deposited at -0.4 V vs. Ag/AgCl (sat. KCl) in the alkaline copper bath for 5, 20, and 60 min, respectively.

Since the surface of the free-standing porous Cu does not vary significantly, the variation of the surface area of the Cu_2O film on the free-standing porous Cu samples mostly comes from the different surface roughness due to the grain size variation on the surface. AFM was performed to investigate the surface roughness (Figure 4–16 and section 4.3.2). The roughness factor of the Cu_2O sample deposited for 5, 20, and 60 min is estimated to be 1.17, 1.36, and 1.41, respectively. The charge carrier densities were calculated by including the roughness factor to the surface area (geometric surface area of all samples is 1 cm^2) in Eq 26. Hole concentrations of 4.9×10^{18}, 3.9×10^{17}, and 2.5×10^{17} cm^{-3} for the samples with 5-, 20-, and 60-min deposition time were obtained (Figure 4–23b). As for the flat band potential, the influence of the various frequencies on the charge carrier densities is relatively small, indicating that the selected frequency range is suitable for the estimation of the acceptor level of the semiconductor.

While the average flat-band potential variation is minor among the three samples over the investigated range of the frequencies, the charge carrier densities vary more strongly. Especially for the 5-min deposited samples, a significant increase of a hole concentration of $\sim 4.9 \times 10^{18}$ cm^{-3} could be observed. This large hole concentration might be influenced by several factors, such as a higher number of crystal defects as was shown by the Raman spectroscopy, smaller Cu_2O crystals, and the lower layer thickness, which influences the bulk conductivity of the film. An increased hole concentration plays an important role to improve the overall performance of the PEC water splitting.

4.6 Photoelectrochemical performances of the Cu_2O samples

4.6.1 Cu_2O on flat Cu substrates

The LSV measurement was conducted in 0.5 M Na_2SO_4 under chopped illumination from the solar simulator. The electrodeposition time was gradually increased to obtain various Cu_2O samples on planar Cu substrate with different thicknesses, as mentioned in section 4.3.1.

Figure 4–24a shows the LSV polarization curve of the Cu_2O film that was deposited at different deposition times. The measurement was scanned from 0.45 to -0.1 vs. RHE. The photocurrent (current during illumination) gradually increases with decreasing applied voltage. In contrast, the dark current (current without illumination) stays constant until -0.05 V vs. RHE and increases slightly. The photocurrents of all samples remain comparable between 0.45 V and 0.2 V vs. RHE. However, below 0.2 V vs. RHE, the photocurrents start to vary, which is likely caused by the different thicknesses of the Cu_2O films. The highest overall photocurrents were obtained for the much thinner films of 5- and 10-min. In contrast, the thicker films deposited with 40, 50, and 60 min have low overall photocurrents throughout the entire scanned voltage.

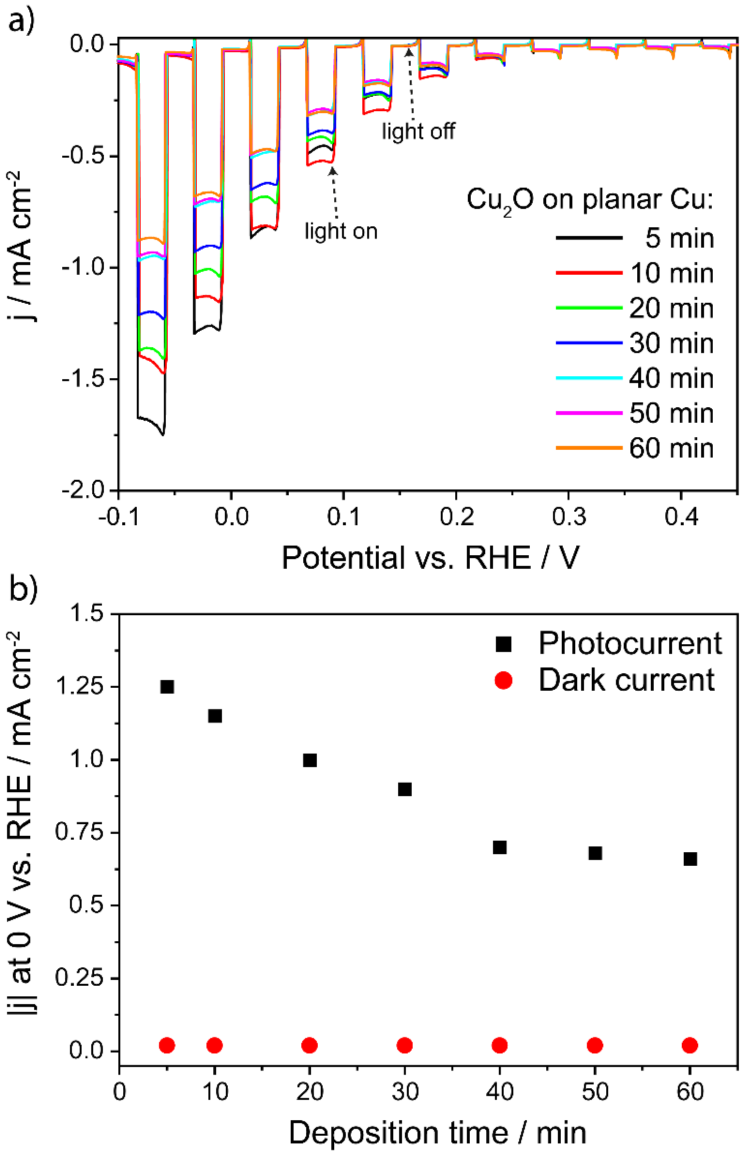

Figure 4–24 a) LSV polarization curve of Cu_2O films on planar Cu substrates deposited at various deposition times and b) Comparison plot of the absolute current densities at 0 V vs. RHE versus the deposition time. The measurement was performed in 0.5 M Na_2SO_4 (pH ~6) under chopped illumination with a scan rate of 5 mV s^{-1}. The black, red, green, blue, cyan, purple, and orange curves represent various planar Cu_2O samples deposited at -0.4 V vs. Ag/AgCl (sat. KCl) for 5, 10,20,30, 40, 50, and 60 min, respectively. The black square and red circle symbols represent the photocurrent and dark current, respectively, at 0 V vs. RHE for various planar Cu_2O samples.

To provide a better comparison for the different Cu_2O samples, the photocurrents and the dark currents at 0 V vs. RHE (HER potential) were plotted against the deposition time

(Figure 4–24b). While the dark currents are constant for all the samples, a linear decrease of the photocurrent between the Cu_2O sample deposited for 5 min and 40 min can be observed. The photocurrents of the sample deposited with longer than 40 min seem to have reached a plateau. Although a thicker Cu_2O film is required for efficient light absorption, the short electron diffusion length of the Cu_2O combined with a longer travel distance of the electron to the surface causes higher recombination rates which leads to an inefficient charge separation [15, 16]. Therefore, low photocurrents were obtained for the samples with a thicker Cu_2O film.

The highest photocurrent of -1.25 mA cm^{-2} was measured for the sample with 5 min deposition time. The thinner film thickness of the 5-min sample with presumably high electrical conductivity allows the electrons to travel to the surface more quickly, thus giving a high photoelectrochemical performance. On the other hand, the 40-, 50-, and 60-min samples with film thicknesses above 2.75 µm are likely to have low electrical conductivity and have a higher rate of charge carrier recombination, limiting the movement of the electron to the surface.

4.6.2 Cu_2O on porous Cu substrates

Figure 4–25a shows the LSV measurement with a scan rate of 5 mV s^{-1} under chopped illumination of the Cu_2O films deposited on various Cu substrates (planar Cu, dendritic porous Cu, reinforced substrate-bound porous Cu, and free-standing porous Cu framework). Figure 4–25b shows the LSV measurement of Cu_2O films obtained at different deposition times on the free-standing porous Cu frameworks.

The Cu_2O deposited on the flat Cu, which has a photocurrent of ~-1.25 mA cm^{-2} at 0 V vs. RHE under illumination. A significant increase in the overall current density can be observed for the sample with the dendritic porous Cu substrate. However, this increase is mainly generated by the undesirably high dark current. In our opinion, there are two possible main reasons why the dark current of the dendritic porous Cu_2O sample is higher than the reference sample. 1) The dendritic porous Cu_2O sample exposes a much higher surface area than that of the flat Cu_2O sample, and therefore it enhances the electrochemical reduction process of the Cu_2O to Cu. 2) The deposition of Cu_2O on the dendritic porous Cu substrate is likely to be non-uniform, and much thinner Cu_2O layers are expected to be deposited at the complex interconnecting pore network due to the low diffusion of the Cu ions. This transport limitation of the Cu ions can also be detected during the reinforcement process of the dendritic porous Cu (see section 4.2) and shown in the chronoamperometric curve of Cu_2O deposition in Figure 4–14a. The relatively thicker layers of the Cu_2O films are less prone to the reduction due to their increased electrical resistivity and thus cause a lower dark current. In contrast, the exceptionally thin Cu_2O layers on the dendritic structures are more reactive, accelerating the reduction process resulting in the increasing dark current.

The two reinforced porous Cu_2O samples (free-standing porous Cu_2O and substrate-bound porous Cu_2O) in Figure 4–25a, also show higher overall current densities than the reference sample (Cu_2O on planar Cu). However, the substrate-bound porous Cu_2O sample shows an increasing dark current, while the free-standing porous Cu_2O sample has a stable low dark current. The cause for this is probably again the inhomogeneously coated dendritic Cu which is still present for the substrate-bound sample at the bottom region (see Figure 4–7a). The free-standing porous Cu_2O sample, on the other hand, reveals a high photocurrent density of -2.25 mA cm^{-2} at 0 V vs. RHE, which is 80 % higher than the photocurrents obtained for the Cu_2O on flat Cu while still maintaining a low dark current (~-35 μA cm^{-2}).

These promising results, which the Cu_2O synthesis via the thermal oxidation on the dendritic porous Cu could not obtain [136] (see Table 1), show that the electrodeposition method can stabilize the reduction of Cu_2O when deposited on a suitable, high surface area substrate. The stabilization of the Cu_2O reduction and low dark current is likely caused by a high-quality homogenous coating of the Cu_2O layer. Furthermore, our results also show a significant improvement of both the photocurrent and the dark current compared to most of the other bare Cu_2O photocathodes prepared on the Cu substrates shown in Table 1. However, the Cu_2O film on planar Au or FTO substrates shows a slightly higher photocurrent due to their preferred crystal orientation in the [111] direction, which was reported to improve the PEC performance significantly [92].

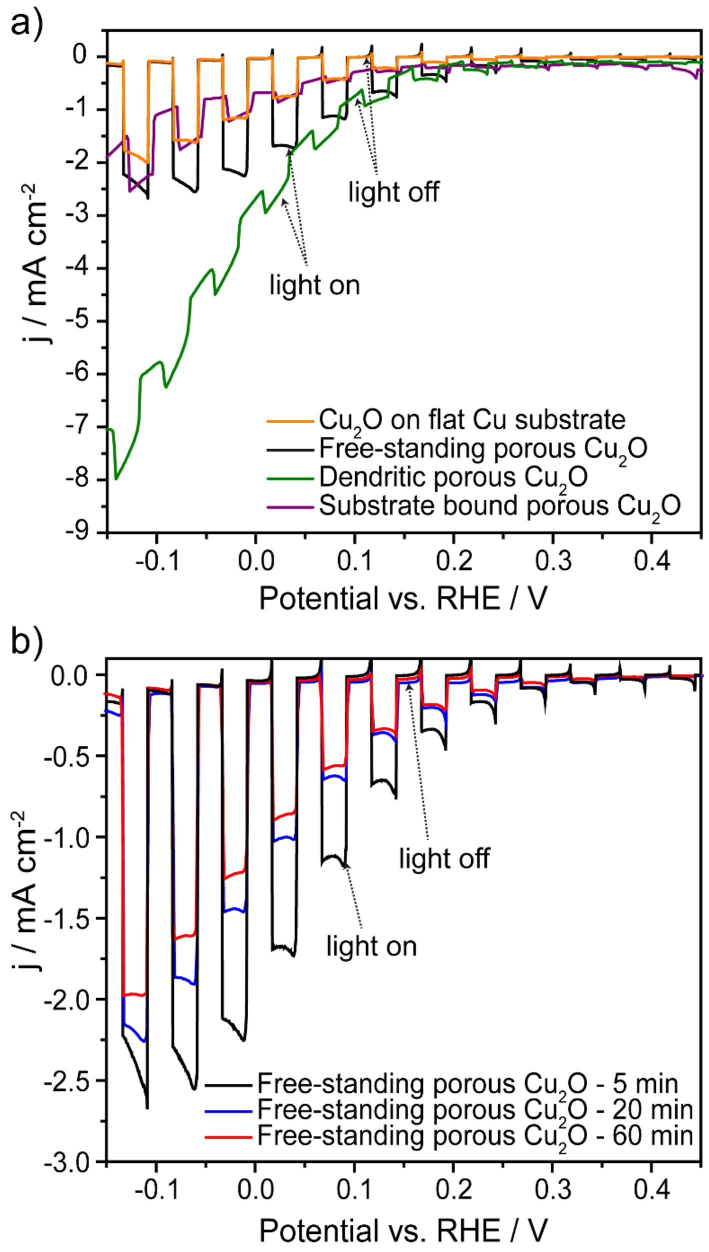

Figure 4–25 Photoelectrochemical analysis of a) Cu_2O film deposited for 5 min on different Cu substrates and b) Cu_2O film deposited on a free-standing porous Cu with different durations. The measurements were done in 0.5 M Na2SO4 (pH ~6) under chopped illumination. The orange, black, green, and purple curves belong to the Cu_2O sample deposited on flat Cu substrate, free-standing porous Cu, dendritic porous Cu, and reinforced substrate-bound porous Cu frameworks, respectively at -0.4 V vs. Ag/AgCl (sat. KCl) for5 min. The red and blue curves represent the Cu_2O samples deposited on free-standing porous Cu frameworks for 20 and 60 min, respectively.

The electrodeposition time of the Cu_2O film strongly influences the photocurrent densities (Figure 4–25b). As was explained previously regarding the PEC performance of the Cu_2O on planar samples, the thickness of the Cu_2O film has a strong influence on enhancing the photocurrent. The short deposition time of 5 min with thinner film thickness shows the highest photocurrents of ~-2.25 mA cm^{-2} at 0 V vs. RHE, while the longer deposition times of 60 min have decreased photocurrent of ~-1.2 mA cm^{-2}.

Table 1 Comparison of various bare Cu_2O photocathodes on their PEC performance.

Substrate	Structure	Fabrication method	Electrolyte	Photocurrent/ dark-current (at 0 V vs. RHE)	Ref.
Flat Cu	Bare Cu_2O nanowire	Wet chemistry/ Thermal annealing	1 M Na_2SO_4	~-2.08 mA cm^{-2} / ~-0.3 mA cm^{-2}	[137]
Cu nanowires	Bare Cu_2O film	Thermal oxidation	1 M Na_2SO_4	~-0.5 mA cm^{-2} / Close to zero	[138]
FTO /Au	Bare Cu_2O film	Electrodeposition	1 M Na_2SO_4	~-2.4 mA cm^{-2} / Close to zero	[17]
FTO	Bare Cu_2O film	Electrodeposition	1 M Na_2SO_4 and 0.1 M formic acid	~-2.5 mA cm^{-2} / ~-0.25 mA cm^{-2}	[139]
FTO	Bare Cu_2O film	Electrodeposition	0.5 M Na_2SO_4	~-0.21 mA cm^{-2} / Close to zero	[107]
FTO	Bare Cu_2O film	Electrodeposition	0.1 M Na_2SO_4	~-0.58 mA cm^{-2} / ~-0.2 mA cm^{-2}	[23]
Dendritic porous Cu	Bare Cu_2O film	Thermal oxidation	0.1 M Na_2SO_4	~-2.25 mA cm^{-2} /~-1 mA cm^{-2}	[136]
Flat Cu	Bare Cu_2O film	Electrodeposition	0.5 M Na_2SO_4	~-1.25 mA cm^{-2} /~-35 µA cm^{-2}	This work
Free-standing porous Cu (large pores)	Bare Cu_2O film	Electrodeposition	0.5 M Na_2SO_4	~-2.25 mA cm^{-2} /~-35 µA cm^{-2}	This work
Free-standing porous Cu (small pores)	Bare Cu_2O film	Electrodeposition	0.5 M Na_2SO_4	~-2.75 mA cm^{-2} /~-35 µA cm^{-2}	This work

After further evaluation of the electronic properties of these samples, even though they have comparable bandgaps (~2eV), the result from the Raman spectroscopy (Figure 4–18) and the Mott-Schottky analysis (Figure 4.23) reveals a significant variation in the number of hole concentrations. This might relate to the high photocurrent density obtained from the thin 5-min Cu_2O sample (-2.25 mA cm^{-2}), which possesses a high hole concentration of 4.9×10^{18} cm^{-3}. Moreover, the insignificant change of the photocurrents between the 20 min (-1.5 mA cm^{-2}) and 60 min (-1.25 mA cm^{-2}) samples also correlates with the slight variation of the hole concentrations of 3.9×10^{17} and 2.5×10^{17} cm^{-3}, respectively.

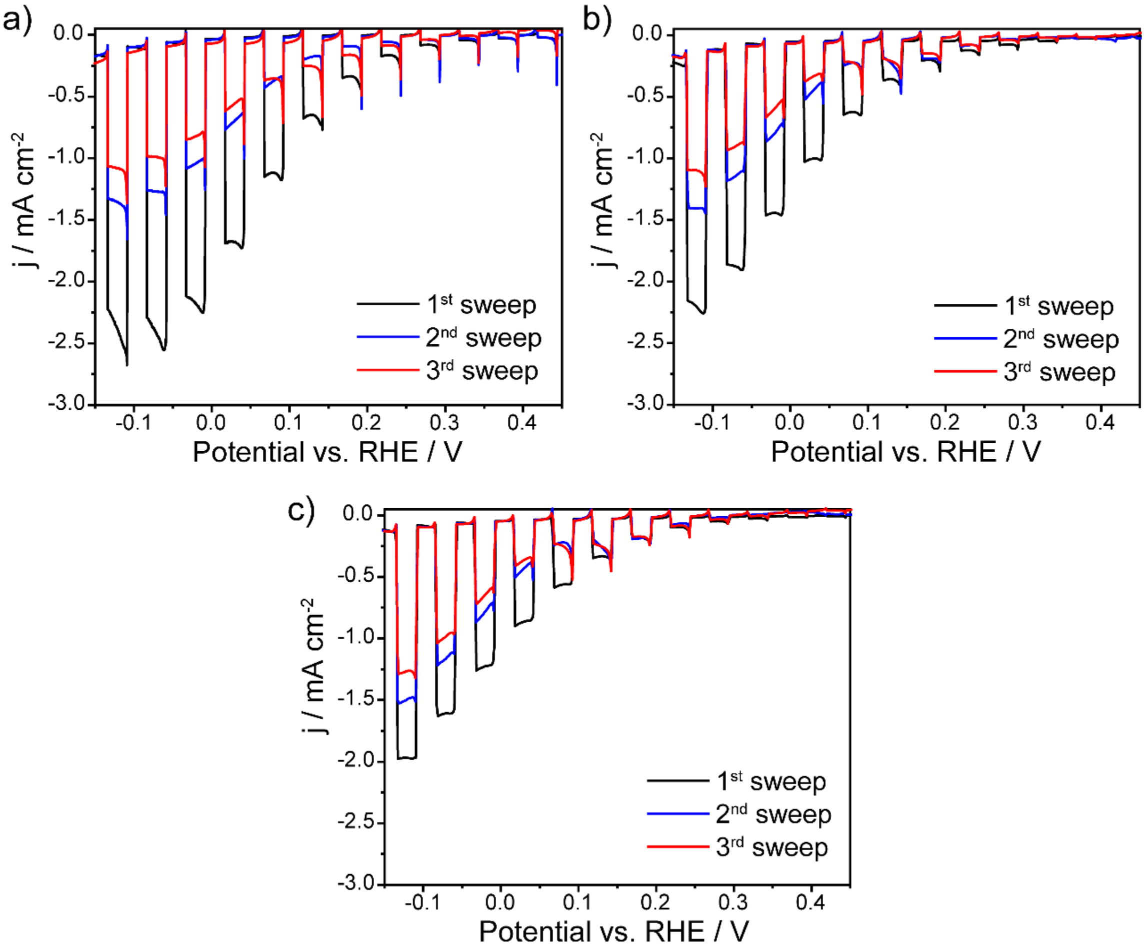

Figure 4–26 Repetitive LSV polarization curve of the free-standing porous Cu_2O samples electrodeposited at a) 5, b) 20, and c) 60 min deposition time. The black, blue, and red curves belong to the first, second, and third consecutive LSV measurements of the same free-standing porous Cu_2O sample.

Without a protective coating, bare Cu_2O is known to have limited stability. The Cu_2O reduces into Cu metal below 0.46 V vs. RHE which causes the photoactivity of the material to degrade [17, 18]. The LSV measurements were repeated three times to investigate the chemical stability of the free-standing porous Cu_2O samples (Figure 4–26). After the second LSV sweep, the photocurrent density of the 5-min deposited sample decreases from -2.25 to -1 mA cm^{-2} at 0 V vs. RHE. In contrast, the photocurrent densities of the 20- and 60-min samples reduce about 0.75 and 0.5 mA cm^{-2}, respectively.

The thin Cu_2O film of the 5-min sample is more photoactive than the thicker film due to the higher hole concentrations and the short diffusion length of the electron to the surface. Therefore, the photodegradation rate is much higher for the 5-min sample than the other Cu_2O samples deposited at 20 and 60 min. After the third LSV sweep, the photodegradation rate of all samples seems to have slowed down. From the second to the third LSV sweep, the photocurrent density decreases about 0.2, 0.15, and 0.1 mA cm^{-2} for the 5-, 20-, and 60-min samples, respectively. This indicates that the surface of the Cu_2O film is gradually covered by Cu metal, which prevents the light from being fully absorbed by the Cu_2O and reduces the photocurrent significantly. The efficiency of the hydrogen production and the long-term stability could not be determined at this point due to the absence of the protective coatings on the Cu_2O samples.

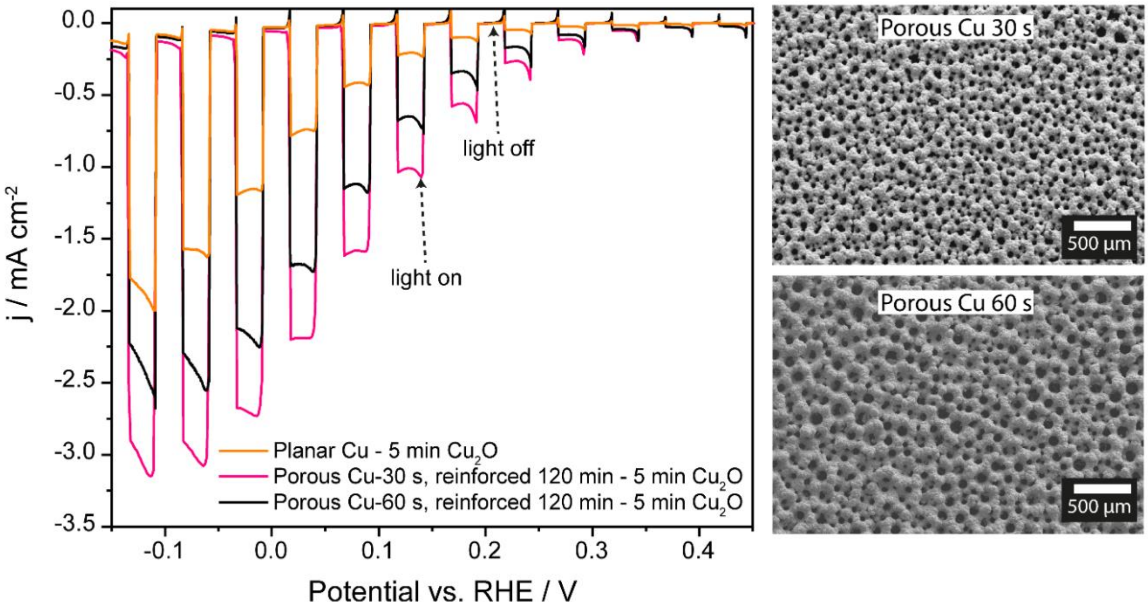

Figure 4–27 linear sweep voltammogram of the Cu_2O film on a planar Cu and two different types of free-standing porous Cu substrates. The free-standing porous Cu samples were electrodeposited at -1.5 A cm^{-2} for 30 s (small pores) and 60 s (large pores). Both samples underwent a second electrodeposition procedure at -20 mA cm^{-2} for 120 min.

Further improvement of the photocurrent was achieved by depositing Cu_2O on the free-standing porous Cu substrate with a smaller pore size (Figure 4–27). The smaller-pores framework was deposited at -1.5 A cm^{-2} for 30 s and was further reinforced with a second electrodeposition process using a smaller current density of -20 mA cm^{-2} for 120 min. The pore diameter of the small-pores sample lies between 25 and 55 µm while the large-pores sample has the diameter of the pores ranging from 60 to 110 µm. Using ImageJ software, the pore density is estimated to be ~80 pores mm^{-2} (small-pores) and ~55 pores mm^{-2} (large-pores). Using the transmittance spectra in section 4.4, the porosity was estimated at 14 % and 23 % for small-pore and large-pore samples, respectively.

These results suggest that the porosity of the sample is not strongly influenced by the pore density but is more related to the pore size diameter and the thickness of the pore wall. The low porosity of the small-pore sample provides a higher surface area, thus significantly improving PEC performance. This can be observed from the photocurrent density of the small-pores sample in Figure 4–27, which is 1.2 times higher than that of the Cu_2O on flat Cu substrate at 0 V vs. RHE and 0.5 mA cm^{-2} more than the previously reported photocurrent for the large-pores sample.

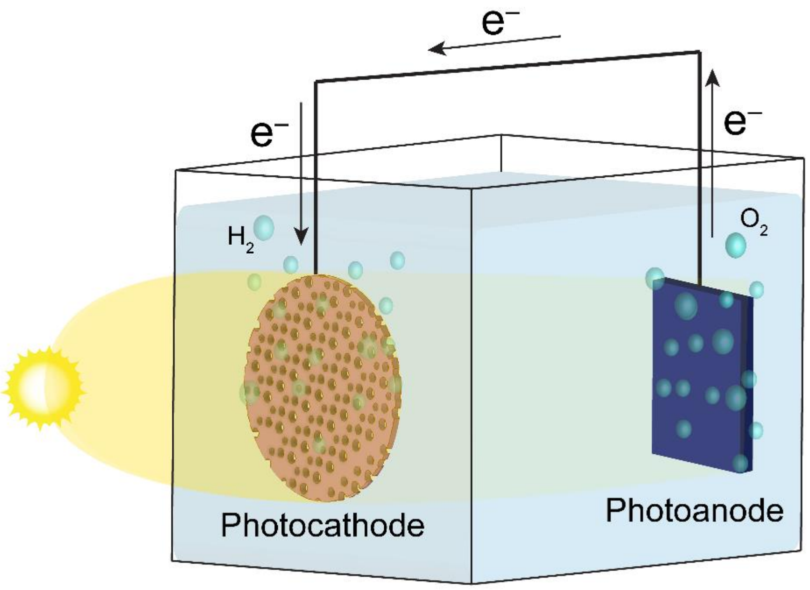

Figure 4–28 Schematic diagram of a photoelectrochemical cell consisting of the free-standing porous Cu_2O photocathode (front) and an n-type photoanode (back) in an aqueous electrolyte under solar illumination.

These unique features, such as tunable porosity and the increased photocurrent, make the porous Cu_2O sample a promising candidate to be used in a tandem system with a photoanode in a full PEC cell (Figure 4–28).

5 Conclusion and Perspective

A preparation route was developed to produce Cu_2O photocathodes with a high photoelectrochemical performance using solely electrochemical deposition processes. Various porous Cu substrates were prepared, and the influence of those substrates on the electrodeposition process of the Cu_2O and their impact on the PEC performance was investigated. A stable porous Cu framework can be achieved by employing a two-step electrodeposition process followed by an ultrasonication procedure (section 3.1.1 and 3.1.2).

In the first step, a dendritic porous Cu structure with a high surface area was electrodeposited on a planar Cu substrate using hydrogen bubbles as a dynamic soft template to produce the porous structure in an acidic $CuSO_4$ bath. Higher current densities (>-1.5 A cm^{-2}) produced more hydrogen bubbles with a high detachment rate and improved the pore distribution, increased the interconnecting pore networks at the interface, and reduced the average pore size from ~300 to ~100 μm. The walls of the porous structure were mainly made of dendritic Cu branches, which have a large surface area but are mechanically too unstable to be used in practical applications (section 4.1). Therefore, a novel approach was used to reinforce the porous structure and improve the mechanical stability.

The dendritic porous Cu framework underwent a second electrodeposition process with a lower current density of -20 mA cm^{-2} in the same acidic copper bath. After 60 min reinforcement, a compact Cu layer on the top region can be observed. However, due to the low diffusion of the Cu ion into the complex interconnecting pore networks at the substrate interface, the dendritic porous Cu could not be fully reinforced. This feature allows the reinforced porous Cu layer to be separated from the planar Cu substrate using an ultrasonication process and form a stable free-standing porous Cu framework with tubular-shaped through pores. The pore size of the free-standing porous Cu frameworks can be tuned easily with an average pore diameter between 50 and 100 μm by changing the electrodeposition time during the synthesis of the dendritic porous Cu. A short duration will produce a porous sample with a smaller pore size.

The Cu_2O layers were deposited on the various substrates, including planar Cu and planar Au, using the potentiostatic electrodeposition method. Aside from the pH of the electrolyte, the growth direction of the Cu_2O crystal during the electrodeposition process is mainly influenced by the crystalline structure of the substrate, which was confirmed by XRD. Further investigation reveals that the grain size and thickness of the layer increase simultaneously as electrodeposition time extends. An electrodeposition time of 5 min produces a film thickness of ~500 nm and crystals between 500 and 800 nm. The planar Cu_2O samples deposited between 5 and 30 min show a significant increase in their thickness and grain size. However, after 30 min deposition time, the electrodeposition rate seems to slow down (section 4.3.1). This behavior can be seen from the unchanging crystal grain size and minor increase of the film thickness, which is likely caused by the increased resistance of the Cu_2O semiconductor due to the thick Cu_2O layer.

Although the different film thicknesses of the Cu_2O samples possess similar defects as investigated using photoluminescence spectroscopy, the number of the defects varied largely between the samples (section 4.3.2). The increasing number of defects can be observed in the Raman spectra and the Mott-Schottky analysis (section 4.3.2 and 4.5), which reveal a high charge carrier density (4.9×10^{18} cm^{-3}) for the thin film sample deposited with 5-min deposition time.

The electrodeposition process of Cu_2O on the different porous substrates (dendritic porous Cu, substrate-bound porous Cu, and the free-standing porous Cu) shows unusual characteristics (section 4.3.2). Like the reinforcement procedure, the low diffusion of the Cu ions into the complex interconnecting pore networks of the dendritic porous Cu structures might produce an inhomogeneous coating of the Cu_2O films. This was observed from chronoamperometric curves of both the dendritic porous Cu and substrate-bound porous Cu samples, which show a fast initial drop of the current densities followed by a plateau after 15 s. On the other hand, the completely exposed free-standing porous Cu frameworks generate a higher overall current density during the potentiostatic electrodeposition process.

For the PEC performance, the photoactivity of the Cu_2O photocathodes decreases as the thickness of the Cu_2O film increases (section 4.6.1). The sample deposited for 5 min on a flat Cu substrate possesses the highest photocurrent density of ~-1.25 mA cm^{-2} at 0 V vs. RHE under 1.5 AM illumination with a low dark current (~-35 µA cm^{-2}). The best overall results on the PEC performance were obtained for the free-standing porous Cu_2O samples that combine high photocurrent densities of -2.25 (large-pore sample) and -2.75 mA cm^{-2}

(small-pore sample), which are 80 % and 120 % higher compared to the Cu_2O on flat Cu sample (section4.6.2), with also a low dark current (~-35 µA cm^{-2}).

Although the dendritic porous structure has considerable potential as electrode material due to its large surface area, the small photocurrent and high dark current obtained from the PEC measurement caused by the inhomogeneous Cu_2O film coating makes it unsuitable to be used as photoelectrode for the PEC application. The dark current is due to the reduction of Cu_2O to Cu. Furthermore, the photocurrent is generated only when the photoactive Cu_2O surfaces are irradiated with light. The highly rough surfaces and the complex geometry of the dendritic porous structure might obstruct the light from reaching the pores' inner region, contributing to the low PEC performance. On the other hand, the dendrite-free surface of the free-standing porous Cu_2O samples with a homogenous Cu_2O coating layer is evenly irradiated with the light and thus shows a high PEC performance. In addition, the geometry of the free-standing porous Cu framework allows for Cu_2O coated tubular pore walls, which are preferentially oriented towards the irradiating light and can help to mitigate the inherent mismatch between the photon absorption length and electron diffusion length in the Cu_2O layer.

Diffuse reflectance UV-Vis spectroscopy reveals that the Cu_2O samples with different thicknesses possess a nearly identical bandgap of ~2 eV (section 3.3.3). This is to be expected as the deposition parameters, besides the electrodeposition time, were kept constant for all the samples. However, even with the same bandgap, the PEC performance varied between the samples. The short deposition time (5 min) leads to the highest photocurrents. This result is in agreement with the higher hole concentrations (4.9×10^{18} cm^{-3}) that were observed by the Mott-Schottky analysis.

Compared to other work based on bare Cu_2O photocathodes, especially on Cu substrates, our samples show an improvement of the photocurrent and the dark current. For instance, a Cu_2O photocathode produced by thermal oxidation of the dendritic porous Cu was reported to reach an overall current density of -2.25 mA cm^{-2} at 0 V vs. RHE [136] under illumination, which is in some way similar to our result. However, a relatively high dark current of -1 mA cm^{-2} at 0 V vs. RHE was observed due to inhomogeneous Cu_2O coating. This confirms that a homogenous layer of Cu_2O film plays a crucial role in lowering the dark current and enhancing PEC performance which can be obtained by implementing the proposed electrodeposition processes.

The other important feature of the free-standing porous Cu_2O samples lies in their tubular through pore structure, which allows light to pass through. Transmission spectroscopy reveals that the transmittance of the Cu_2O samples varies with their different pore size. The small-pore sample (25-55 μm) and the large-pore sample (60-110 μm) have 14 % and 23 % transmittance, respectively (section 3.3.3). This makes these structures promising candidates to be used in a tandem system together with a photoanode.

In perspective, the long-term chemical stability of the Cu_2O photocathodes needs to be thoroughly investigated and improved. A homogeneous and thin protective layer should be coated preferably using an inexpensive electrodeposition method on the Cu_2O surfaces to prevent electrochemical reduction of the materials in the presence of hydrogen evolution. Additionally, an n-type semiconductor such as Ga_2O_3 can also be added as a buffer layer, creating a p-n junction and increasing the overall photogenerated voltage. Once the long-term chemical stability of the photocathode is achieved, the amount of hydrogen can be evaluated using gas chromatography, and solar-to-hydrogen efficiency can then be determined.

The overall surface area of the free-standing porous Cu should be further characterized. One approach is to use EIS or CV to determine the double-layer capacitance. This capacitance is sensitive to the electrode surface and can be used to determine the electrochemically active surface area of the sample.

References

1. Creutzig F., Agoston P., Goldschmidt JC., et al. (2017) The underestimated potential of solar energy to mitigate climate change. Nat Energy 2:. https://doi.org/10.1038/nenergy.2017.140
2. Edenhofer O., Madruga RP., Sokona Y., et al. (2011) Renewable energy sources and climate change mitigation: Special report of the intergovernmental panel on climate change
3. Jäger-Waldau A. (2019) PV Status Report 2019
4. Schultz O., Mette A., Preu R., Gluntz SW. (2007) Silicon Solar Cells with Screen-printed Front Side Metallization Exceeding 19% Efficiency. Silicon Sol Cells with Screen-printed Front Side Met Exceed 19% Effic 6–9
5. Hisatomi T., Kubota J., Domen K. (2014) Recent advances in semiconductors for photocatalytic and photoelectrochemical water splitting. Chem Soc Rev 43:7520–7535. https://doi.org/10.1039/c3cs60378d
6. Yartys VA., Lototsky M V. (2005) An Overview of Hydrogen Storage Methods. In: Veziroglu TN, Yu. Zaginaichenko S, Schur D V, et al (eds) Hydrogen Materials Science and Chemistry of Carbon Nanomaterials. Springer Netherlands, Dordrecht, pp 75–104
7. Glenk G., Reichelstein S. (2019) Economics of converting renewable power to hydrogen. Nat Energy 4:216–222. https://doi.org/10.1038/s41560-019-0326-1
8. Soltani R., Rosen MA., Dincer I. (2014) Assessment of CO2 capture options from various points in steam methane reforming for hydrogen production. Int J Hydrogen Energy 39:20266–20275. https://doi.org/10.1016/j.ijhydene.2014.09.161
9. Fujishima A., Honda K. (1972) Electrochemical Photolysis of Water at a Semiconductor Electrode. Nature 238:37–38. https://doi.org/10.1038/238038a0
10. Zhong M., Sato Y., Kurniawan M., et al. (2012) ZnO dense nanowire array on a film structure in a single crystal domain texture for optical and photoelectrochemical applications. Nanotechnology 23:495602
11. Wang H., Deutsch T., Turner J a. (2008) Direct Water Splitting under Visible Light with Nanostructured Hematite and WO[sub 3] Photoanodes and a GaInP[sub 2] Photocathode. J Electrochem Soc 155:F91. https://doi.org/10.1149/1.2888477
12. Zhang X., Li H., Wang S., et al. (2014) Improvement of hematite as photocatalyst by doping with tantalum. J Phys Chem C 118:16842–16850. https://doi.org/10.1021/jp500395a
13. Paracchino A., Brauer JC., Moser JE., et al. (2012) Synthesis and characterization of high-photoactivity electrodeposited Cu 2O solar absorber by photoelectrochemistry and ultrafast spectroscopy. J Phys Chem C 116:7341–7350. https://doi.org/10.1021/jp301176y
14. Meyer BK., Polity A., Reppin D., et al. (2012) Binary copper oxide semiconductors: From materials towards devices. Phys Status Solidi Basic Res 249:1487–1509. https://doi.org/10.1002/pssb.201248128
15. de Jongh PE., Vanmaekelbergh D., Kelly JJ. (2000) Photoelectrochemistry of Electrodeposited Cu[sub 2]O. J Electrochem Soc 147:486. https://doi.org/10.1149/1.1393221
16. Engel CJ., Polson TA., Spado JR., et al. (2008) Photoelectrochemistry of porous p-Cu2 O films. J Electrochem Soc 155:37–42. https://doi.org/10.1149/1.2830850
17. Paracchino A., Laporte V., Sivula K., et al. (2011) Highly active oxide photocathode for photoelectrochemical water reduction. Nat Mater 10:456–461. https://doi.org/10.1038/nmat3017
18. Nitopi S., Bertheussen E., Scott SB., et al. (2019) Progress and Perspectives of Electrochemical CO2 Reduction on Copper in Aqueous Electrolyte. Chem Rev 119:7610–7672. https://doi.org/10.1021/acs.chemrev.8b00705

19. An X., Li K., Tang J. (2014) Cu2O/reduced graphene oxide composites for the photocatalytic conversion of CO2. ChemSusChem 7:1086–1093. https://doi.org/10.1002/cssc.201301194
20. Paracchino A., Mathews N., Hisatomi T., et al. (2012) Ultrathin films on copper(i) oxide water splitting photocathodes: a study on performance and stability. Energy Environ Sci 5:8673. https://doi.org/10.1039/c2ee22063f
21. Brittman S., Yoo Y., Dasgupta NP., et al. (2014) Epitaxially aligned cuprous oxide nanowires for all-oxide, single-wire solar cells. Nano Lett 14:4665–4670. https://doi.org/10.1021/nl501750h
22. Lin CY., Lai YH., Mersch D., Reisner E. (2012) Cu 2ONiO x nanocomposite as an inexpensive photocathode in photoelectrochemical water splitting. Chem Sci 3:3482–3487. https://doi.org/10.1039/c2sc20874a
23. Wu H., Zheng Z., Toe CY., et al. (2020) A pulse electrodeposited amorphous tunnel layer stabilises Cu2O for efficient photoelectrochemical water splitting under visible-light irradiation. J Mater Chem A 8:5638–5646. https://doi.org/10.1039/d0ta00629g
24. Azevedo J., Steier L., Dias P., et al. (2014) On the stability enhancement of cuprous oxide water splitting photocathodes by low temperature steam annealing. Energy Environ Sci 7:4044–4052. https://doi.org/10.1039/c4ee02160f
25. Dasgupta NP., Liu C., Andrews S., et al. (2013) Atomic layer deposition of platinum catalysts on nanowire surfaces for photoelectrochemical water reduction. J Am Chem Soc 135:12932–12935. https://doi.org/10.1021/ja405680p
26. Dai P., Xie J., Mayer MT., et al. (2013) Solar hydrogen generation by silicon nanowires modified with platinum nanoparticle catalysts by atomic layer deposition. Angew Chemie - Int Ed 52:11119–11123. https://doi.org/10.1002/anie.201303813
27. Zhang Z., Dua R., Zhang L., et al. (2013) Carbon-Layer-Protected Cuprous Oxide Nanowire Arrays for Efficient Water Reduction. 1709–1717
28. Kargar A., Seena Partokia S., Tong Niu M., et al. (2014) Solution-grown 3D Cu2O networks for efficient solar water splitting. Nanotechnology 25:. https://doi.org/10.1088/0957-4484/25/20/205401
29. Luo J., Steier L., Son MK., et al. (2016) Cu2O Nanowire Photocathodes for Efficient and Durable Solar Water Splitting. Nano Lett 16:1848–1857. https://doi.org/10.1021/acs.nanolett.5b04929
30. Bowker M. (2011) Sustainable hydrogen production by the application of ambient temperature photocatalysis. Green Chem 13:2235–2246. https://doi.org/10.1039/c1gc00022e
31. Rheinländer PJ., Herranz J., Durst J., Gasteiger HA. (2014) Kinetics of the Hydrogen Oxidation/Evolution Reaction on Polycrystalline Platinum in Alkaline Electrolyte Reaction Order with Respect to Hydrogen Pressure. J Electrochem Soc 161:F1448–F1457. https://doi.org/10.1149/2.0501414jes
32. Habbache N., Alane N., Djerad S., Tifouti L. (2009) Leaching of copper oxide with different acid solutions. Chem Eng J 152:503–508. https://doi.org/10.1016/j.cej.2009.05.020
33. Grätzel M. (2001) Photoelectrochemical cells. Nature 414:338–344. https://doi.org/10.1038/35104607
34. Nozik AJ. (1978) Photoelectrochemistry : Applications to Solar Energy Conversion. Annu Rev Phys Chem 29:189–222
35. Sivula K. (2013) Metal oxide photoelectrodes for solar fuel production, surface traps, and catalysis. J Phys Chem Lett 4:1624–1633. https://doi.org/10.1021/jz4002983
36. Bott AW. (1998) Electrochemistry of Semiconductors. 3:87–91
37. McShane CM., Choi KS. (2012) Junction studies on electrochemically fabricated p-n Cu 2O homojunction solar cells for efficiency enhancement. Phys Chem Chem Phys 14:6112–6118. https://doi.org/10.1039/c2cp40502d

38. Gelderman K., Lee L., Donne SW. (2007) Flat-Band Potential of a Semiconductor: Using the Mott–Schottky Equation. J Chem Educ 84:685–688. https://doi.org/10.1021/ed084p685
39. Xu Q., Zhang L., Yu J., et al. (2018) Direct Z-scheme photocatalysts: Principles, synthesis, and applications. Mater Today 21:1042–1063. https://doi.org/10.1016/j.mattod.2018.04.008
40. Park K., Kim YJ., Yoon T., et al. (2019) A methodological review on material growth and synthesis of solar-driven water splitting photoelectrochemical cells. RSC Adv 9:30112–30124. https://doi.org/10.1039/c9ra05341g
41. Polman A., Atwater HA. (2012) Photonic design principles for ultrahigh-efficiency photovoltaics. Nat Mater 11:174–177. https://doi.org/10.1038/nmat3263
42. Yang W., Prabhakar RR., Tan J., et al. (2019) Strategies for enhancing the photocurrent, photovoltage, and stability of photoelectrodes for photoelectrochemical water splitting. Chem Soc Rev 48:4979–5015. https://doi.org/10.1039/c8cs00997j
43. Dias P., Mendes A. (2019) Hydrogen Production from Photoelectrochemical Water Splitting
44. Jian J., Jiang G., van de Krol R., et al. (2018) Recent advances in rational engineering of multinary semiconductors for photoelectrochemical hydrogen generation. Nano Energy 51:457–480. https://doi.org/10.1016/j.nanoen.2018.06.074
45. Maeda K., Domen K. (2010) Photocatalytic water splitting: Recent progress and future challenges. J Phys Chem Lett 1:2655–2661. https://doi.org/10.1021/jz1007966
46. Chen Z., Dinh HN., Miller E. (2013) Photoelectrochemical water splitting: standards, experimental methods, and protocols
47. Lin Y., Yuan G., Sheehan S., et al. (2011) Hematite-based solar water splitting: Challenges and opportunities. Energy Environ Sci 4:4862–4869. https://doi.org/10.1039/c1ee01850g
48. Chen S., Wang LW. (2012) Thermodynamic oxidation and reduction potentials of photocatalytic semiconductors in aqueous solution. Chem Mater 24:3659–3666. https://doi.org/10.1021/cm302533s
49. Wick R., Tilley SD. (2015) Photovoltaic and Photoelectrochemical Solar Energy Conversion with Cu2O. J Phys Chem C 119:26243–26257. https://doi.org/10.1021/acs.jpcc.5b08397
50. Li C., Li Y., Delaunay JJ. (2014) A novel method to synthesize highly photoactive Cu2O microcrystalline films for use in photoelectrochemical cells. ACS Appl Mater Interfaces 6:480–486. https://doi.org/10.1021/am404527q
51. Liu C., Dasgupta NP., Yang P. (2014) Semiconductor Nanowires for Artificial Photosynthesis
52. Zhang Y., Deng B., Zhang T., et al. (2010) Shape effects of Cu2O polyhedral microcrystals on photocatalytic activity. J Phys Chem C 114:5073–5079. https://doi.org/10.1021/jp9110037
53. Bornoz P., Abdi FF., Tilley SD., et al. (2014) A bismuth vanadate-cuprous oxide tandem cell for overall solar water splitting. J Phys Chem C 118:16959–16966. https://doi.org/10.1021/jp500441h
54. Yourey JE., Bartlett BM. (2011) Electrochemical deposition and photoelectrochemistry of CuWO4, a promising photoanode for water oxidation. J Mater Chem 21:7651–7660. https://doi.org/10.1039/c1jm11259g
55. Ida S., Yamada K., Matsunaga T., et al. (2010) Preparation of p-type CaFe2O4 photocathodes for producing hydrogen from water. J Am Chem Soc 132:17343–17345. https://doi.org/10.1021/ja106930f
56. Tahir AA., Wijayantha KGU., Mazhar M., McKee V. (2010) ZnFe2O4 thin films from a single source precursor by aerosol assisted chemical vapour deposition. Thin Solid Films 518:3664–3668. https://doi.org/10.1016/j.tsf.2009.09.104
57. Prévot MS., Guijarro N., Sivula K. (2015) Enhancing the Performance of a Robust Sol-Gel-

Processed p-Type Delafossite CuFeO2 Photocathode for Solar Water Reduction. ChemSusChem 8:1359–1367. https://doi.org/10.1002/cssc.201403146

58. Ruiz E., Alvarez S., Alemany P., Evarestov RA. (1997) Electronic structure and properties of Cu2O. Phys Rev B 56:7189–7196. https://doi.org/10.1103/physrevb.56.7189
59. Raebiger H., Lany S., Zunger A. (2007) Origins of the p-type nature and cation deficiency in Cu2O and related materials. Phys Rev B - Condens Matter Mater Phys 76:. https://doi.org/10.1103/PhysRevB.76.045209
60. Wright AF., Nelson JS. (2002) Theory of the copper vacancy in cuprous oxide. J Appl Phys 92:5849–5851. https://doi.org/10.1063/1.1516620
61. Nolan M., Elliott SD. (2006) The p-type conduction mechanism in Cu2O: A first principles study. Phys Chem Chem Phys 8:5350–5358. https://doi.org/10.1039/b611969g
62. Matsuzaki K., Nomura K., Yanagi H., et al. (2008) Epitaxial growth of high mobility Cu2 O thin films and application to p -channel thin film transistor. Appl Phys Lett 93:2–5. https://doi.org/10.1063/1.3026539
63. Jiang C., Moniz SJA., Wang A., et al. (2017) Photoelectrochemical devices for solar water splitting-materials and challenges. Chem Soc Rev 46:4645–4660. https://doi.org/10.1039/c6cs00306k
64. Marschall R. (2014) Semiconductor composites: Strategies for enhancing charge carrier separation to improve photocatalytic activity. Adv Funct Mater 24:2421–2440. https://doi.org/10.1002/adfm.201303214
65. Ishizuka S., Kato S., Okamoto Y., Akimoto K. (2002) Control of hole carrier density of polycrystalline Cu2O thin films by Si doping. Appl Phys Lett 80:950–952. https://doi.org/10.1063/1.1448398
66. Sowers KL., Fillinger A. (2009) Crystal Face Dependence of p-Cu[sub 2]O Stability as Photocathode. J Electrochem Soc 156:F80. https://doi.org/10.1149/1.3089290
67. Deuermeier J., Gassmann J., Brötz J., Klein A. (2011) Reactive magnetron sputtering of Cu2O: Dependence on oxygen pressure and interface formation with indium tin oxide. J Appl Phys 109:. https://doi.org/10.1063/1.3592981
68. Iivonen T., Heikkilä MJ., Popov G., et al. (2019) Atomic Layer Deposition of Photoconductive Cu2O Thin Films. ACS Omega 4:11205–11214. https://doi.org/10.1021/acsomega.9b01351
69. Lim YF., Chua CS., Lee CJJ., Chi D. (2014) Sol-gel deposited Cu2O and CuO thin films for photocatalytic water splitting. Phys Chem Chem Phys 16:25928–25934. https://doi.org/10.1039/c4cp03241a
70. Chua D., Kim SB., Li K., Gordon R. (2019) Low temperature chemical vapor deposition of cuprous oxide thin films using a copper(i) amidinate precursor. ACS Appl Energy Mater 2:7750–7756. https://doi.org/10.1021/acsaem.9b01683
71. Choudhary S., Sarma JVN., Gangopadhyay S. (2016) Growth and characterization of single phase Cu2O by thermal oxidation of thin copper films. AIP Conf Proc 1724:. https://doi.org/10.1063/1.4945236
72. Wang YX., Tang XF., Yang ZG. (2011) A novel wet-chemical method of preparing highly monodispersed Cu2O nanoparticles. Colloids Surfaces A Physicochem Eng Asp 388:38–40. https://doi.org/10.1016/j.colsurfa.2011.08.004
73. Daltin A-L., Addad A., Chopart J-P. (2005) Potentiostatic deposition and characterization of cuprous oxide films and nanowires. J Cryst Growth 282:414–420. https://doi.org/10.1016/j.jcrysgro.2005.05.053
74. Septina W., Ikeda S., Khan MA., et al. (2011) Potentiostatic electrodeposition of cuprous oxide thin films for photovoltaic applications. Electrochim Acta 56:4882–4888. https://doi.org/10.1016/j.electacta.2011.02.075
75. Kim M., Yoon S., Jung H., et al. (2014) The influence of polarity of electrodeposited Cu2O thin films on the photoelectrochemical performance. Jpn J Appl Phys 53:11–15.

https://doi.org/10.7567/JJAP.53.08NJ01

76. Wang LC., de Tacconi NR., Chenthamarakshan CR., et al. (2007) Electrodeposited copper oxide films: Effect of bath pH on grain orientation and orientation-dependent interfacial behavior. Thin Solid Films 515:3090–3095. https://doi.org/10.1016/j.tsf.2006.08.041
77. Mo C., Barreto J., Stavale F., et al. (2018) Water Adsorption to Crystalline Cu 2 O Thin Films : Structural and Vibrational Properties. https://doi.org/10.1021/acs.jpcc.7b10835
78. Shi H., Yu K., Sun F., Zhu Z. (2012) Controllable synthesis of novel Cu2O micro/nano-crystals and their photoluminescence, photocatalytic and field emission properties. CrystEngComm 14:278–285. https://doi.org/10.1039/c1ce05868a
79. Pan L., Kim JH., Mayer MT., et al. (2018) Boosting the performance of Cu2O photocathodes for unassisted solar water splitting devices. Nat Catal 1:412–420. https://doi.org/10.1038/s41929-018-0077-6
80. Martell AE., Hancock RD. (1996) Metal Complexes in Aqueous Solutions
81. Obradović MD., Stevanović RM., Despić AR. (2003) Electrochemical deposition of Ni-W alloys from ammonia-citrate electrolyte. J Electroanal Chem 552:185–196. https://doi.org/10.1016/S0022-0728(03)00151-7
82. Poizot P., Hung CJ., Nikiforov MP., et al. (2003) An electrochemical method for CuO thin film deposition from aqueous solution. Electrochem Solid-State Lett 6:2–7. https://doi.org/10.1149/1.1535753
83. Breyfogle BE., Hung C., Shumsky MG., Switzer JA. (1996) Electrodeposition of Silver(II) Oxide Films. J Electrochem Soc 143:2741–2746. https://doi.org/10.1149/1.1837101
84. Gujar TP., Shinde VR., Lokhande CD., Han SH. (2006) Electrosynthesis of Bi2O3 thin films and their use in electrochemical supercapacitors. J Power Sources 161:1479–1485. https://doi.org/10.1016/j.jpowsour.2006.05.036
85. Wang AQ., Golden TD. (2013) Electrodeposition of Oriented Cerium Oxide Films. Int J Electrochem 2013:1–10. https://doi.org/10.1155/2013/482187
86. Zhou Y., Switzer JA. (1996) Growth of cerium(IV) oxide films by the electrochemical generation of base method. J Alloys Compd 237:1–5. https://doi.org/10.1016/0925-8388(95)02048-9
87. Eskhult J., Herranen M., Nyholm L. (2006) On the origin of the spontaneous potential oscillations observed during galvanostatic deposition of layers of Cu and Cu2O in alkaline citrate solutions. J Electroanal Chem 594:35–49. https://doi.org/10.1016/j.jelechem.2006.05.019
88. Eskhult J., Nyholm L. (2008) Pulsed galvanostatic and potentiostatic electrodeposition of Cu and Cu 2O nanolayers from alkaline Cu(II)-citrate solutions. J Electrochem Soc 155:2–9. https://doi.org/10.1149/1.2806793
89. Shin HC., Liu M. (2004) Copper foam structures with highly porous nanostructured walls. Chem Mater 16:5460–5464. https://doi.org/10.1021/cm048887b
90. Laursen AB., Varela AS., Dionigi F., et al. (2012) Electrochemical hydrogen evolution: Sabatiers principle and the volcano plot. J Chem Educ 89:1595–1599. https://doi.org/10.1021/ed200818t
91. Plowman BJ., Jones LA., Bhargava SK. (2015) Building with bubbles: The formation of high surface area honeycomb-like films via hydrogen bubble templated electrodeposition. Chem Commun 51:4331–4346. https://doi.org/10.1039/c4cc06638c
92. Li Y., Jia WZ., Song YY., Xia XH. (2007) Superhydrophobicity of 3D porous copper films prepared using the hydrogen bubble dynamic template. Chem Mater 19:5758–5764. https://doi.org/10.1021/cm071738j
93. Shin HC., Liu M. (2005) Three-dimensional porous copper-tin alloy electrodes for rechargeable lithium batteries. Adv Funct Mater 15:582–586. https://doi.org/10.1002/adfm.200305165
94. Plowman BJ., O'Mullane AP., Selvakannan P., Bhargava SK. (2010) Honeycomb nanogold

networks with highly active sites. Chem Commun 46:9182–9184. https://doi.org/10.1039/c0cc03696j

95. González-Buch C., Herraiz-Cardona I., Ortega E., et al. (2013) Synthesis and characterization of macroporous Ni, Co and Ni-Co electrocatalytic deposits for hydrogen evolution reaction in alkaline media. Int J Hydrogen Energy 38:10157–10169. https://doi.org/10.1016/j.ijhydene.2013.06.016
96. Yu X., Wang M., Wang Z., et al. (2016) 3D multi-structural porous NiAg films with nanoarchitecture walls: high catalytic activity and stability for hydrogen evolution reaction. Electrochim Acta 211:900–910. https://doi.org/10.1016/j.electacta.2016.06.062
97. Ahn CY., Lim MS., Hwang W., et al. (2017) Effect of Porous Metal Flow Field in Polymer Electrolyte Membrane Fuel Cell under Pressurized Condition. Fuel Cells 17:652–661. https://doi.org/10.1002/fuce.201700042
98. Varzi A., Mattarozzi L., Cattarin S., et al. (2018) 3D Porous Cu–Zn Alloys as Alternative Anode Materials for Li-Ion Batteries with Superior Low T Performance. Adv Energy Mater 8:1–11. https://doi.org/10.1002/aenm.201701706
99. Chaturvedi P., Sarker S., Chen X., et al. (2019) Enhancing the Cooperative Catalytic Effect in Ni/Co Hydr(oxy)oxide Porous Electrodes for Overall Water Splitting and Glucose Sensing. ACS Sustain Chem Eng 7:11303–11312. https://doi.org/10.1021/acssuschemeng.9b00822
100. Hao M., Charbonneau V., Fomena NN., et al. (2019) Hydrogen Bubble Templating of Fractal Ni catalysts for Water Oxidation in Alkaline Media. ACS Appl Energy Mater 2:5734–5743. https://doi.org/10.1021/acsaem.9b00860
101. Still ER., Wikberg P. (1980) Solution studies of systems with polynuclear complex formation. 1. The copper(II) citrate system. Inorganica Chim Acta 46:147–152. https://doi.org/10.1016/S0020-1693(00)84183-3
102. Daniele PG., Ostacoli G., Zerbinati O., et al. (1988) Mixed metal complexes in solution. Thermodynamic and spectrophotometric study of copper(II)-citrate heterobinuclear complexes with nickel(II), zinc(II) or cadmium(II) in aqueous solution. Transit Met Chem 13:87–91. https://doi.org/10.1007/BF01087794
103. Shyamal S., Hajra P., Mandal H., et al. (2015) Effect of Substrates on the Photoelectrochemical Reduction of Water over Cathodically Electrodeposited p-Type Cu2O Thin Films. ACS Appl Mater Interfaces 7:18344–18352. https://doi.org/10.1021/acsami.5b04116
104. Marimon M. (2019) The influence of the crystal orientation of Copper (I) oxide on the performance for photoelectrochemical water splitting
105. Bérubé LP., L'Espérance G. (1989) A Quantitative Method of Determining the Degree of Texture of Zinc Electrodeposits. J Electrochem Soc 136:2314–2315. https://doi.org/10.1149/1.2097318
106. Beranek R. (2011) (Photo)electrochemical methods for the determination of the band edge positions of TiO 2-based nanomaterials. Adv Phys Chem 2011:80–83. https://doi.org/10.1155/2011/786759
107. Yang Y., Xu D., Wu Q., Diao P. (2016) Cu2O/CuO bilayered composite as a high-efficiency photocathode for photoelectrochemical hydrogen evolution reaction. Sci Rep 6:1–13. https://doi.org/10.1038/srep35158
108. Mahmoodi N., Rushdi AI., Bowen J., et al. (2017) Room temperature thermally evaporated thin Au film on Si suitable for application of thiol self-assembled monolayers in micro/nano-electro-mechanical-systems sensors. J Vac Sci Technol A Vacuum, Surfaces, Film 35:041514. https://doi.org/10.1116/1.4990026
109. Ma QB., Hofmann JP., Litke A., Hensen EJM. (2015) Cu2O photoelectrodes for solar water splitting: Tuning photoelectrochemical performance by controlled faceting. Sol Energy

Mater Sol Cells 141:178–186. https://doi.org/10.1016/j.solmat.2015.05.025

110. Chen K., Xue D. (2012) PH-assisted crystallization of Cu 2O: Chemical reactions control the evolution from nanowires to polyhedra. CrystEngComm 14:8068–8075. https://doi.org/10.1039/c2ce26084k

111. Wang W., Wu D., Zhang Q., et al. (2010) PH -dependence of conduction type in cuprous oxide synthesized from solution. J Appl Phys 107:. https://doi.org/10.1063/1.3452383

112. Burrows ND., Hale CRH., Penn RL. (2013) Effect of pH on the kinetics of crystal growth by oriented aggregation. Cryst Growth Des 13:3396–3403. https://doi.org/10.1021/cg4001939

113. Elmahdy MM., El-Shaer A. (2019) Structural, optical and dielectric investigations of electrodeposited p-type Cu2O. J Mater Sci Mater Electron 30:19894–19905. https://doi.org/10.1007/s10854-019-02356-z

114. Du QT., Tan JS., Wang QT., et al. (2012) Electrochemical deposition and formation mechanism of single-crystalline Cu 2O octahedra on aluminum. J Anal Methods Chem 1:. https://doi.org/10.1155/2012/406162

115. Langford JI., Wilson AJC. (1978) Scherrer after Sixty Years: A Survey and Some New Results in the Determination of Crystallite Size. J Appl Crystallogr 11:102–113. https://doi.org/10.1107/S0021889878012844

116. Compaan A., Cummins HZ. (1972) Raman scattering, luminescence, and exciton-phonon coupling in Cu2O. Phys Rev B 6:4753–4757. https://doi.org/10.1103/PhysRevB.6.4753

117. Compaan A. (1975) Surface damage effects on allowed and forbidden phonon. Solid State Commun 16:293–296

118. Balkanski M., Nusimovici MA., Reydellet J. (1969) First order Raman spectrum of Cu2O. Solid State Commun 7:815–818. https://doi.org/10.1016/0038-1098(69)90768-6

119. Reydellet J., Balkanski M., Trivich D. (1972) Light Scattering and Infrared Absorption in Cuprous Oxide. Phys Status Solidi 52:175–185. https://doi.org/10.1002/pssb.2220520120

120. Dawson P., Hargreave MM., Wilkinson GR. (1973) The dielectric and lattice vibrational spectrum of cuprous oxide. J Phys Chem Solids 34:2201–2208. https://doi.org/10.1016/S0022-3697(73)80067-8

121. Sander T. (2015) Monitoring defect-induced perturbations of the ideal crystal structure of ZnO and Cu2O by Raman spectroscopy. Justus-Liebig-Universität Gieÿen

122. Ganesan KP., Sivakumar G., Anandhan N., et al. (2019) Influence of bath temperatures on physical and electrical properties of potentiostatically deposited Cu 2 O thin films for heterojunction solar cell applications. Opt Quantum Electron 51:1–16. https://doi.org/10.1007/s11082-019-1745-8

123. Sander T., Reindl CT., Giar M., et al. (2014) Correlation of intrinsic point defects and the Raman modes of cuprous oxide. Phys Rev B - Condens Matter Mater Phys 90:1–8. https://doi.org/10.1103/PhysRevB.90.045203

124. Powell D., Compaan A., Macdonald JR., Forman RA. (1975) Raman-scattering study of ion-implantation-produced damage in Cu2O. Phys Rev B 12:20–25. https://doi.org/10.1103/PhysRevB.12.20

125. Li C., Li Y., Delaunay J. (2014) A Novel Method to Synthesize Highly Photoactive Cu 2 O Microcrystalline Films for Use in Photoelectrochemical Cells

126. Sander T., Reindl CT., Klar PJ. (2014) Breaking of Raman selection rules in Cu2O by intrinsic point defects. J Br Stud 1633:81–86. https://doi.org/10.1557/opl.2014.47

127. Ito T., Masumi T. (1997) Detailed Examination of Relaxation Processes of Excitons in Photoluminescence Spectra of Cu2O. J. Phys. Soc. Japan 66:2185–2193

128. Zouaghi M., Prevot B., Carabatos C., Sieskind M. (1972) Near infrared optical and photoelectric properties of Cu2O. III. Interpretation of experimental results. Phys Status Solidi 11:449–460. https://doi.org/10.1002/pssa.2210110207

129. Wang C., Xu J., Shi S., et al. (2016) Structural, optical and photoelectrical properties of Cu2O films electrodeposited at different pH. RSC Adv 6:4422–4428. https://doi.org/10.1039/c5ra23216c

130. Shi H., Yu K., Wang Y., et al. (2012) Shape evolution, photoluminescence and degradation properties of novel Cu 2O micro/nanostructures. Appl Phys A Mater Sci Process 108:709–717. https://doi.org/10.1007/s00339-012-6954-y

131. Suzuki M., Yamamoto T., Katayama Y., et al. (2012) Light absorption by metals with porous surface layer formed by oxidizationreduction treatment. Mater Trans 53:1556–1562. https://doi.org/10.2320/matertrans.M2012139

132. Wang Y., Lany S., Ghanbaja J., et al. (2016) Electronic structures of C u2 O, C u4 O3, and CuO: A joint experimental and theoretical study. Phys Rev B 94:. https://doi.org/10.1103/PhysRevB.94.245418

133. Niu W., Moehl T., Cui W., et al. (2018) Extended Light Harvesting with Dual Cu2O-Based Photocathodes for High Efficiency Water Splitting. Adv Energy Mater 8:. https://doi.org/10.1002/aenm.201702323

134. Hankin A., Bedoya-Lora FE., Alexander JC., et al. (2019) Flat band potential determination: Avoiding the pitfalls. J Mater Chem A 7:26162–26176. https://doi.org/10.1039/c9ta09569a

135. Vasheghani Farahani SK., Veal TD., Mudd JJ., et al. (2014) Valence-band density of states and surface electron accumulation in epitaxial SnO2 films. Phys Rev B - Condens Matter Mater Phys 90:. https://doi.org/10.1103/PhysRevB.90.155413

136. Ma X., Zhang J., Wang B., et al. (2018) Hierarchical Cu2O foam/g-C3N4 photocathode for photoelectrochemical hydrogen production. Appl Surf Sci 427:907–916. https://doi.org/10.1016/j.apsusc.2017.09.075

137. Bai J., Li Y., Wang R., et al. (2015) A novel 3D ZnO/Cu2O nanowire photocathode material with highly efficient photoelectrocatalytic performance. J Mater Chem A 3:22996–23002. https://doi.org/10.1039/c5ta07583a

138. Huang Q., Kang F., Liu H., et al. (2013) Highly aligned Cu2O/CuO/TiO2 core/shell nanowire arrays as photocathodes for water photoelectrolysis. J Mater Chem A 1:2418–2425. https://doi.org/10.1039/c2ta00918h

139. Kunturu PP., Huskens J. (2019) Efficient Solar Water Splitting Photocathodes Comprising a Copper Oxide Heterostructure Protected by a Thin Carbon Layer. ACS Appl Energy Mater 2:7850–7860. https://doi.org/10.1021/acsaem.9b01290

List of Figures

FIGURE 1–1: SCHEMATIC REPRESENTATION OF THE ENHANCED LIGHT ABSORPTION WITH THE SHORT ELECTRON DIFFUSION LENGTH TO THE SURFACE OF THE CU_2O COATED PORE WALL STRUCTURE. 3

FIGURE 2–1: UPWARD BAND BENDING OF A) N-TYPE SEMICONDUCTOR AND DOWNWARD BAND BENDING OF B) P-TYPE SEMICONDUCTOR IN EQUILIBRIUM WITH ELECTROLYTE WITHOUT ILLUMINATION[35]. 9

FIGURE 2–2: ILLUSTRATION OF PEC CELL CONFIGURATION USING A) A SINGLE PHOTOANODE, C) A SINGLE PHOTOCATHODE, AND E) TANDEM CONFIGURATION (Z-SCHEME). THE ENERGY BAND DIAGRAM WITH THE DETAILED MECHANISM OF EACH CONFIGURATION IS PRESENTED IN B), D), AND F). [39] 11

FIGURE 2–3: ILLUSTRATION OF THE PEC CELL BASED ON A PHOTOCATHODE AND METAL ANODE UNDER LIGHT ILLUMINATION[42]. $E_{F,P,}$ AND $E_{F,N}$ REPRESENT THE QUASI-FERMI LEVEL OF HOLES AND ELECTRONS, RESPECTIVELY. 12

FIGURE 2–4: THEORETICAL VALUE OF THE MAXIMUM ACHIEVABLE SOLAR-TO-HYDROGEN (STH) EFFICIENCY AND THE PHOTOCURRENT AS A FUNCTION OF THE SEMICONDUCTOR BANDGAP[45]. THE PHOTOCURRENT WAS CALCULATED UNDER THE ASSUMPTION THAT THE SOLAR CONVERSION HAS NO ADDITIONAL EFFICIENCY LOSS. 13

FIGURE 2–5: BAND EDGE POSITIONS OF VARIOUS SEMICONDUCTORS FOR PEC WATER SPLITTING APPLICATION AT PH 0. THE BLUE AND RED BAR REPRESENT THE VB AND THE CB OF THE SEMICONDUCTOR, RESPECTIVELY. THE DATA WAS ADAPTED FROM REFERENCE[47]. 14

FIGURE 2–6: A) CRYSTAL STRUCTURE OF CU_2O IN A SINGLE UNIT CELL. VARIOUS CRYSTALLINE SHAPES OF THE ELECTRODEPOSITED CU_2O WITH DIFFERENT CRYSTAL ORIENTATIONS: B) [100]-ORIENTED, C) [110]-ORIENTED, AND D) [111]-ORIENTED. THE FIGURES WERE RECONSTRUCTED ACCORDING TO THE REFERENCE [75]. 17

FIGURE 3–1: SCHEMATIC REPRESENTATION OF THE ELECTROCHEMICAL PROCEDURE TO SYNTHESIZE POROUS CU_2O PHOTOCATHODE 23

FIGURE 3–2: PHOTOGRAPHS OF THE CUSTOM-MADE PVDF SAMPLE HOLDER AND ADAPTER. 24

FIGURE 3–3: PHOTOGRAPH OF A) A PMMA CELL CONTAINER AND B) AN ASSEMBLED CELL WITH THE SAMPLE ADAPTER 25

FIGURE 3–4: ELECTROCHEMICAL DEPOSITION PROCESS OF DENDRITIC POROUS CU IN AN ACIDIC BATH CONTAINING 0.2 M CUSO4 AND 1 M H_2SO_4 AT PH ~0 25

FIGURE 3–5: ELECTRODEPOSITION PROCESS OF CU_2O IN AN ALKALINE COPPER BATH AT 60°C. 27

FIGURE 3–6: SCHEMATIC DIAGRAM OF A) ELECTRICAL DOUBLE LAYER AT THE INTERFACE BETWEEN THE N-TYPE SEMICONDUCTOR AND THE ELECTROLYTE AND B) AN EQUIVALENT CIRCUIT CONSISTING OF A SPACE CHARGE CAPACITANCE OF THE SEMICONDUCTOR AND DOUBLE LAYER CAPACITANCE CONNECTED IN SERIES. IHP AND OHP ARE THE INNER AND OUTER HELMHOLTZ PLANES, RESPECTIVELY. THIS DIAGRAM IS ADAPTED FROM THE REFERENCE [105]. 32

FIGURE 3–7: PHOTOGRAPH OF A) PMMA PEC CELL WITH A TRANSPARENT FRONT WINDOW AND B) FULLY ASSEMBLED PEC CELL WITH SAMPLE ADAPTER AND ELECTRODES HOLDER. THE REFERENCE ELECTRODE (RE) AND COUNTER ELECTRODE (CE) IS PLACED ON THE LEFT AND RIGHT SIDES, RESPECTIVELY, OF THE COPPER WORKING ELECTRODE (WE). 34

FIGURE 3–8: SOLAR SIMULATOR CONFIGURATION FOR THE PEC EXPERIMENT (TOP VIEW). 35

FIGURE 4–1: HEIGHT PROFILES OF VARIOUS DENDRITIC POROUS CU STRUCTURES ELECTRODEPOSITED IN AN ACIDIC COPPER ELECTROLYTE (0.2 M CUSO$_4$ AND 1 M H$_2$SO$_4$) WITH DIFFERENT CURRENT DENSITIES AND DURATIONS (SEE INFORMATION AT THE TOP LEFT CORNER OF EACH GRAPH). 37

FIGURE 4–2: SCANNING ELECTRON MICROGRAPHS OF THE ELECTRODEPOSITED DENDRITIC POROUS CU STRUCTURES ON A FLAT CU SUBSTRATE IN AN ACIDIC COPPER BATH USING DIFFERENT CURRENT DENSITIES AND DEPOSITION DURATIONS: A) -0.075 A CM^{-2}, 400 S; B) -0.15 A CM^{-2}, 240 S; C) -0.37 A CM^{-2}, 160 S; D) -0.75 A CM^{-2}, 100 S; E) -1.5 A CM^{-2}, 60 S AND F) -2.25 A CM^{-2}, 40 S. THE INSETS SHOW MAGNIFIED IMAGES OF THE PORES. 38

FIGURE 4–3: INFLUENCE OF APPLIED CURRENT DENSITY ON THE CHANGE OF A) MASS AND B) CURRENT EFFICIENCY FOR ELECTRODEPOSITED CU ON FLAT CU SUBSTRATE. 39

FIGURE 4–4: MORPHOLOGICAL COMPARISON OF THE ELECTRODEPOSITED POROUS CU STRUCTURE ON FLAT CU SUBSTRATE DEPOSITED AT A FIXED CURRENT DENSITY OF -1.5 A CM^{-2} WITH DIFFERENT DURATIONS BETWEEN 2 TO 60 S. THESE SAMPLES UNDERGO A REINFORCEMENT PROCEDURE FOR 30 MIN. 40

FIGURE 4–5: MAGNIFIED WALL OF THE POROUS CU LAYER ELECTRODEPOSITED AT -1.5 A CM^{-2} FOR 60 SEC WITH A) 5X AND B) 25X MAGNIFICATIONS. 41

FIGURE 4–6: REINFORCEMENT PROCEDURE OF THE DENDRITIC POROUS CU (DEPOSITED AT 1.5 A CM^{-2} FOR 60 S) WITH A) NO REINFORCEMENT B) 5 MIN, C) 30 MIN, D) 60 MIN, AND E) 120 MIN CU DEPOSITION TIME AT CURRENT DENSITIES OF -20 MA CM^{-2}. THE PHOTOGRAPHS SHOW THE SAMPLES BEFORE AND AFTER THE REINFORCEMENT PROCEDURE. 42

FIGURE 4–7: MORPHOLOGICAL COMPARISON OF A) A SUBSTRATE-BOUND AND B) FREE-STANDING POROUS CU FRAMEWORKS ELECTRODEPOSITED AT -1.5 A CM^{-2} FOR 60 S AND REINFORCED AT -20 MA CM^{-2} FOR 120 MIN (FOR DETAIL SEE SECTION 3.1.2). C) SAMPLE PHOTOGRAPHS OF THE FREE-STANDING POROUS CU. THE TOP IMAGE SHOWS THE CROSS-SECTION OF THE SAMPLES (SIDE VIEW), AND THE BOTTOM PART SHOWS THE SURFACE MORPHOLOGY (TOP VIEW) 43

FIGURE 4–8: REINFORCEMENT PROCEDURE OF THE DENDRITIC POROUS CU LAYER WITH A)120 MIN, B) 180 MIN, C) 240 MIN, AND D) 300 MIN. ULTRASONICATION WAS PERFORMED ON ALL SAMPLES TO SEPARATE THE POROUS LAYER FROM THE FLAT CU SUBSTRATE. 45

FIGURE 4–9: CYCLIC VOLTAMMOGRAM OF THE REINFORCED POROUS CU SUBSTRATE (AT -1.5 A CM^{-2}, 60 S – REINFORCED FOR 120 MIN) IN ALKALINE CU BATH (PH ~12) WITH CONSTANT BATH TEMPERATURE OF 60°C RECORDED WITH A SCAN RATE OF 20 MV S^{-1} AND 20 CYCLES. THE ARROW WHICH POINTS UPWARD INDICATES THE MOVEMENT OF THE CATHODIC PEAK WITH INCREASING CYCLE NUMBER. 46

FIGURE 4–10:AFM IMAGES OF ELECTRODEPOSITED CU$_2$O FILM ON A) FLAT CU COIN AND B) 200 NM OF AU PLATED SI WAFER. THE 200 NM AU LAYER WAS DEPOSITED ON A SI WAFER BY A THERMAL EVAPORATION METHOD. THE CU$_2$O FILM ON BOTH SUBSTRATES IS ELECTRODEPOSITED AT -0.4 V VS. AG/AGCL (SAT. KCL) IN THE ALKALINE CU BATH FOR 30 MIN WITH A CONSTANT BATH TEMPERATURE OF 60°C. 47

FIGURE 4–11:X-RAY DIFFRACTOGRAM OF THE ELECTRODEPOSITED CU$_2$O FILM ON PLANAR AU AND CU SUBSTRATES. THE CU2O FILM WAS ELECTRODEPOSITED AT -0.4 V VS. AG/AGCL (SAT. KCL) IN AN ALKALINE CU BATH FOR 30 MIN ON BOTH SUBSTRATES. ALL XRD PATTERNS UNDERGO THE KA2 REMOVAL PROCESS USING THE DIFFRAC EVALUATION SOFTWARE FROM BRUKER. 48

FIGURE 4–12:ESTIMATED CU$_2$O FILM THICKNESS USING FARADAY LAW WITH 100 % CURRENT EFFICIENCY FROM THE TOTAL CHARGE OBTAINED AT DIFFERENT DEPOSITION TIMES. THE MASS OF THE DEPOSITED CU$_2$O IS CALCULATED USING THE FARADAY EQUATION (EQ. 29). 50

FIGURE 4–13:THICKNESS COMPARISON OF THE ELECTRODEPOSITED CU_2O FILM ON FLAT CU SUBSTRATES WITH DEPOSITION TIME OF A) 5 MIN, B) 30 MIN, AND C) 60 MIN. THESE SAMPLES WERE DEPOSITED AT -0.4 V VS. AG/AGCL (SAT. KCL) IN THE ALKALINE COPPER BATH WITH A CONSTANT BATH TEMPERATURE OF 60°C. THE SAMPLES WERE CUT USING A SHARP HAND LEVER SCISSOR. 51

FIGURE 4–14:CURRENT TRANSIENTS OF A) CU_2O FILM ELECTRODEPOSITED ON DIFFERENT SUBSTRATES AND B) CU_2O FILM ON FREE-STANDING POROUS CU SUBSTRATES AT DIFFERENT DEPOSITION TIMES. THE BLUE AND BLACK CURVES REPRESENT THE CU_2O ON THE DENDRITIC POROUS CU AND REINFORCED SUBSTRATE BOUND POROUS CU SUBSTRATES, RESPECTIVELY. THE RED, YELLOW, AND GREY CURVES CORRESPOND TO THE CU_2O ON FREE-STANDING POROUS CU SUBSTRATES. ALL SAMPLES WERE ELECTRODEPOSITED AT -0.4 V VS. AG/AGCL (SAT. KCL) IN THE ALKALINE COPPER BATH. 52

FIGURE 4–15:SURFACE MORPHOLOGY COMPARISON OF CU_2O FILMS ELECTRODEPOSITED POTENTIOSTATICALLY AT -0.4 V VS. AG/AGCL (SAT. KCL) ON THE FREE-STANDING POROUS CU FRAMEWORK FOR OF A) 5, B) 10, C) 20, D) 30, E) 40, AND F) 60 MIN DEPOSITION TIME IN A CU CITRATE BATH (PH 12). 53

FIGURE 4–16:HIGH MAGNIFICATION AFM IMAGES OF CU_2O FILM DEPOSITED ON FREE-STANDING POROUS CU FOR A) 5 MIN, B) 20 MIN, AND C) 60 MIN WITH SURFACE ROUGHNESS SQ OF 53.2 NM, 149 NM, AND 165 NM, RESPECTIVELY. 54

FIGURE 4–17:XRD PATTERNS OF CU_2O FILMS DEPOSITED ON FREE-STANDING POROUS FRAMEWORKS AT DIFFERENT DEPOSITION TIMES. ALL PATTERNS UNDERWENT THE KA2 REMOVAL PROCESS USING THE DIFFRAC EVALUATION SOFTWARE FROM BRUKER. THE IDENTIFIED CRYSTAL PLANE FOR BOTH CU_2O AND CU IS PLACED IN THE GRAPH WITH THE TEXT COLOR OF BLACK AND YELLOW, RESPECTIVELY. 55

FIGURE 4–18:RAMAN SPECTRA OF CU_2O FILM ON FREE-STANDING POROUS CU FRAMEWORKS DEPOSITED AT DIFFERENT DURATIONS. THE PEAK POSITIONS ARE PLACED AT THE TOP PART OF THE GRAPH. 56

FIGURE 4–19:PHOTOLUMINESCENCE SPECTRA OF THE CU_2O ON FREE-STANDING POROUS CU FRAMEWORKS. THE BLUE, YELLOW, AND GREY CURVES BELONG TO THE FREE-STANDING POROUS CU_2O SAMPLES ELECTRODEPOSITED AT -0.4 V VS. AG/AGCL (SAT. KCL) IN AN ALKALINE COPPER BATH FOR 5, 20, AND 60 MIN, RESPECTIVELY. 58

FIGURE 4–20:OPTICAL CHARACTERIZATION USING A) UV-VIS DIFFUSE REFLECTANCE SPECTRA AND B) TAUC PLOT WITH THE KUBELKA-MUNK FUNCTION OF THE FREE-STANDING POROUS CU_2O SAMPLES WITH DIFFERENT DEPOSITION TIMES. THE BLACK, YELLOW, AND GREY SYMBOLS REPRESENT THE FREE-STANDING POROUS CU_2O SAMPLES ELECTRODEPOSITED AT -0.4 V VS. AG/AGCL (SAT. KCL) IN THE ALKALINE COPPER BATH FOR 5, 20, AND 60 MIN, RESPECTIVELY. 60

FIGURE 4–21:TRANSMITTANCE SPECTRA OF A) ELECTRODEPOSITED CU_2O FILMS ON A FREE-STANDING POROUS CU FRAMEWORK (-1.5 A CM^{-2} FOR 60 S AND REINFORCED AT 20 MA CM^{-2} FOR 120 MIN) WITH DIFFERENT DURATIONS AND B) 5-MIN CU_2O FILM ON VARIOUS FREE-STANDING POROUS CU SAMPLES WITH DIFFERENT PORE SIZES. THE BLACK, YELLOW, AND GREY SYMBOLS BELONG TO THE CU_2O SAMPLES DEPOSITED AT -0.4 V VS. AG/AGCL (SAT. KCL) FOR 5, 20, AND 60 MIN, RESPECTIVELY, ON A FREE-STANDING POROUS CU FRAMEWORK. THE GREEN, RED AND BLUE SYMBOLS BELONG TO THE CU_2O SAMPLES DEPOSITED FOR 5 MIN ON VARIOUS FREE-STANDING POROUS CU DEPOSITED AT -1.5 A CM^{-2} FOR 30, 40, AND 50 S, RESPECTIVELY. 61

FIGURE 4–22:MOTT-SCHOTTKY PLOTS OF DEPOSITED CU_2O FILMS ON FREE-STANDING POROUS CU FRAMEWORK (DENDRITIC POROUS CU DEPOSITION FOR 60 S AND REINFORCED WITH 120 MIN) FOR A) 5, B) 20, AND C) 60 MIN DEPOSITION TIME AT VARIOUS FREQUENCIES IN 0.5 M NA_2SO_4 (PH ~6). 63

FIGURE 4–23:EVALUATION OF A) THE FLAT-BAND POTENTIAL (E_{FB}) AND B) THE HOLE CONCENTRATIONS (N_A) FROM THE MOTT-SCHOTTKY PLOTS AT DIFFERENT FREQUENCIES. THE BLACK SQUARE, RED CIRCLE,

AND BLUE TRIANGLE REPRESENT THE FREE-STANDING POROUS CU2O SAMPLE DEPOSITED AT -0.4 V VS. AG/AGCL (SAT. KCL) IN THE ALKALINE COPPER BATH FOR 5, 20, AND 60 MIN, RESPECTIVELY. 64

FIGURE 4–24:A) LSV POLARIZATION CURVE OF CU_2O FILMS ON PLANAR CU SUBSTRATES DEPOSITED AT VARIOUS DEPOSITION TIMES AND B) COMPARISON PLOT OF THE ABSOLUTE CURRENT DENSITIES AT 0 V VS. RHE VERSUS THE DEPOSITION TIME. THE MEASUREMENT WAS PERFORMED IN 0.5 M NA_2SO_4 (PH ~6) UNDER CHOPPED ILLUMINATION WITH A SCAN RATE OF 5 MV S^{-1}. THE BLACK, RED, GREEN, BLUE, CYAN, PURPLE, AND ORANGE CURVES REPRESENT VARIOUS PLANAR CU_2O SAMPLES DEPOSITED AT -0.4 V VS. AG/AGCL (SAT. KCL) FOR 5, 10,20,30, 40, 50, AND 60 MIN, RESPECTIVELY. THE BLACK SQUARE AND RED CIRCLE SYMBOLS REPRESENT THE PHOTOCURRENT AND DARK CURRENT, RESPECTIVELY, AT 0 V VS. RHE FOR VARIOUS PLANAR CU_2O SAMPLES. 66

FIGURE 4–25:PHOTOELECTROCHEMICAL ANALYSIS OF A) CU2O FILM DEPOSITED FOR 5 MIN ON DIFFERENT CU SUBSTRATES AND B) CU2O FILM DEPOSITED ON A FREE-STANDING POROUS CU WITH DIFFERENT DURATIONS. THE MEASUREMENTS WERE DONE IN 0.5 M NA2SO4 (PH ~6) UNDER CHOPPED ILLUMINATION. THE ORANGE, BLACK, GREEN, AND PURPLE CURVES BELONG TO THE CU2O SAMPLE DEPOSITED ON FLAT CU SUBSTRATE, FREE-STANDING POROUS CU, DENDRITIC POROUS CU, AND REINFORCED SUBSTRATE-BOUND POROUS CU FRAMEWORKS, RESPECTIVELY AT -0.4 V VS. AG/AGCL (SAT. KCL) FOR5 MIN. THE RED AND BLUE CURVES REPRESENT THE CU2O SAMPLES DEPOSITED ON FREE-STANDING POROUS CU FRAMEWORKS FOR 20 AND 60 MIN, RESPECTIVELY. 69

FIGURE 4–26:REPETITIVE LSV POLARIZATION CURVE OF THE FREE-STANDING POROUS CU_2O SAMPLES ELECTRODEPOSITED AT A) 5, B) 20, AND C) 60 MIN DEPOSITION TIME. THE BLACK, BLUE, AND RED CURVES BELONG TO THE FIRST, SECOND, AND THIRD CONSECUTIVE LSV MEASUREMENTS OF THE SAME FREE-STANDING POROUS CU_2O SAMPLE. 71

FIGURE 4–27:LINEAR SWEEP VOLTAMMOGRAM OF THE CU_2O FILM ON A PLANAR CU AND TWO DIFFERENT TYPES OF FREE-STANDING POROUS CU SUBSTRATES. THE FREE-STANDING POROUS CU SAMPLES WERE ELECTRODEPOSITED AT -1.5 A CM^{-2} FOR 30 S (SMALL PORES) AND 60 S (LARGE PORES). BOTH SAMPLES UNDERWENT A SECOND ELECTRODEPOSITION PROCEDURE AT -20 MA CM^{-2} FOR 120 MIN. 72

FIGURE 4–28:SCHEMATIC DIAGRAM OF A PHOTOELECTROCHEMICAL CELL CONSISTING OF THE FREE-STANDING POROUS CU_2O PHOTOCATHODE (FRONT) AND AN N-TYPE PHOTOANODE (BACK) IN AN AQUEOUS ELECTROLYTE UNDER SOLAR ILLUMINATION. 73

Scientific Publications

Peer-reviewed Journals

1) **Kurniawan, M.**; Stich, M.; Marimon, M.; Camargo, M.; Peipmann, R.; Hannappel, T.; Bund, A. Electrodeposition of Cuprous Oxide on a Porous Cu Framework for an Improved Photoelectrochemical Performance. J. Mater. Sci. 2021. https://doi.org/10.1007/s10853-021-06058-y.

2) Link, S.; **Kurniawan, M**.; Dimitrova, A.; Krischok, S.; Bund, A.; Ivanov, S. Enhanced Cycling Performance of Binder Free Silicon-Based Anode by Application of Electrochemically Formed Microporous Substrate. Electrochim. Acta 2021, 380, 138216. https://doi.org/10.1016/j.electacta.2021.138216.

3) Carmen Mejia, M. Del; Sánchez, L. F.; **Kurniawan, M.**; Eggert, L.; Tejada, A.; Camargo, M.; Grieseler, R.; Rumiche, F.; Díaz, I.; Bund, A.; Guerra, J. A. Analysis of the Physical and Photoelectrochemical Properties of C-Si(p)/a-SiC:H(p) Photocathodes for Solar Water Splitting. J. Phys. D. Appl. Phys. 2021, 54 (19). https://doi.org/10.1088/1361-6463/abdb69.

4) Mulyaningsih, S.; Klemke, B.; Siemensmeyer, K.; Fritz, M.; **Kurniawan, M.**; Ispas, A.; Bund, A. Influence of Thermal Treatment on the Magnetic Properties and Morphology of Electrodeposited Fe-Co Films. J. Magn. Magn. Mater. 2020, 513 (July), 167204. https://doi.org/10.1016/j.jmmm.2020.167204.

5) Behúl, M.; Vojs, M.; Marton, M.; Michniak, P.; Mikolášek, M.; **Kurniawan, M**.; Honig, H. L.; Zyabkin, D. V.; Ramirez, M. O.; Spieß, L.; Flock, D.; Bund, A.; Papula, M.; Redhammer, R. Nanostructured Boron Doped Diamond Enhancing the Photoelectrochemical Performance of TiO2/BDD Heterojunction Anodes. Vacuum 2020, 171 (October 2019). https://doi.org/10.1016/j.vacuum.2019.109006.

6) Vlaic, C. A.; **Kurniawan, M.**; Peipmann, R.; Lalău, C. C.; Stich, M.; Schmidt, U.; Bund, A. Improved Wear Resistance of Alternating Amorphous and Crystalline Layers in Electrodeposited NiP Multilayers. Surf. Coatings Technol. 2020, 386 (June 2019). https://doi.org/10.1016/j.surfcoat.2020.125470.

7) Leimbach, M.; Tschaar, C.; Zapf, D.; **Kurniawan, M.**; Schmidt, U.; Bund, A. Relation between Color and Surface Morphology of Electrodeposited Chromium for Decorative Applications. J. Electrochem. Soc. 2019, 166 (6), D205–D211. https://doi.org/10.1149/2.0871906jes.

8) Schoetz, T.; **Kurniawan, M.**; Stich, M.; Peipmann, R.; Efimov, I.; Ispas, A.; Bund, A.; Ponce De Leon, C.; Ueda, M. Understanding the Charge Storage Mechanism of Conductive Polymers as Hybrid Battery-Capacitor Materials in Ionic Liquids by: In Situ Atomic Force Microscopy and Electrochemical Quartz Crystal Microbalance Studies. J. Mater. Chem. A 2018, 6 (36), 17787–17799. https://doi.org/10.1039/c8ta06757k.

9) Stich, M.; Göttlinger, M.; **Kurniawan, M.**; Schmidt, U.; Bund, A. Hydrolysis of LiPF6 in Carbonate-Based Electrolytes for Lithium-Ion Batteries and in Aqueous Media. J. Phys. Chem. C 2018, 122 (16), 8836–8842. https://doi.org/10.1021/acs.jpcc.8b02080.

10) Behul, M.; Vojs, M.; Marton, M.; Michniak, P.; **Kurniawan, M.**; Peipmann, R.; Vlaic, C. A.; Bund, A.; Redhammer, R. Electrodeposition of Cuprous Oxide on Boron Doped Diamond Electrodes. Adv. Electr. Electron. Eng. 2018, 16 (2), 239–245. https://doi.org/10.15598/aeee.v16i2.2778.

11) Steinhauer, M.; Stich, M.; **Kurniawan, M.**; Seidlhofer, B. K.; Trapp, M.; Bund, A.; Wagner, N.; Friedrich, K. A. In Situ Studies of Solid Electrolyte Interphase (SEI) Formation on Crystalline Carbon Surfaces by Neutron Reflectometry and Atomic Force Microscopy. ACS Appl. Mater. Interfaces 2017, 9 (41), 35794–35801. https://doi.org/10.1021/acsami.7b09181.

Supervision of Master thesis

1) Marimon M.; The influence of the crystal orientation of Copper (I) oxide on the performance for photoelectrochemical water splitting, Master Thesis, Tu Ilmenau 2019.

2) Ostheimer, D.; Lichtinduzierte Herstellung Von Nickelpartikeln Auf P-Si (111) Und Charakterisierung der Photoelektrokatalytischen Eigenschaften des Systems. Master Thesis, Tu Ilmenau, 2019.

Appendix

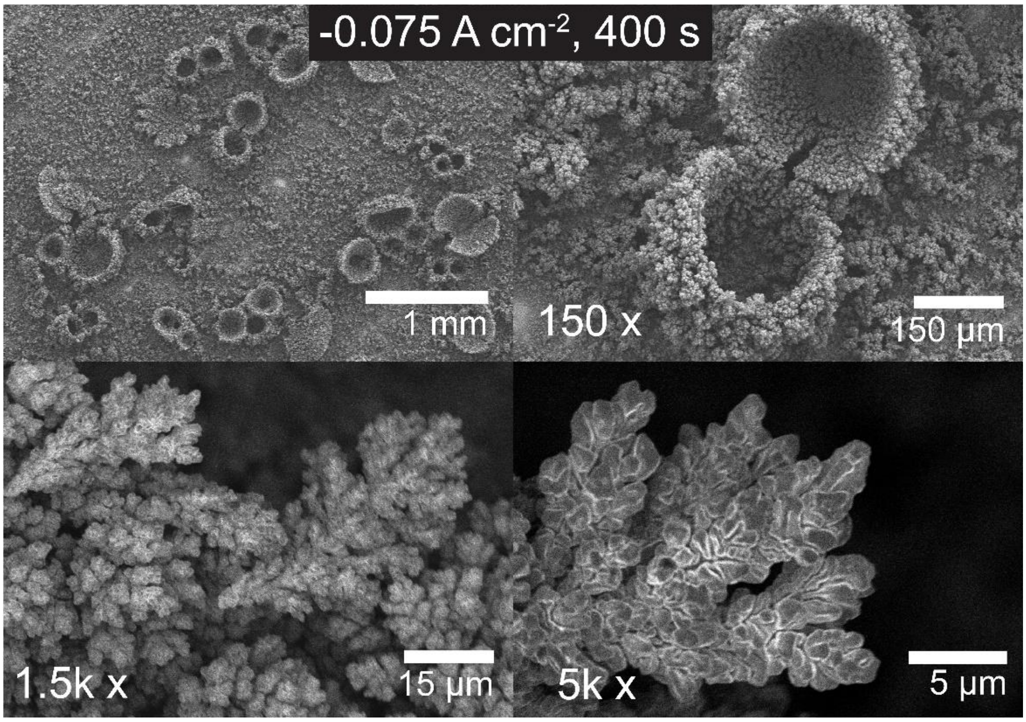

Figure A. 1 Surface morphology of dendritic porous Cu deposited at -0.075 A cm-2 for 400 s with different magnifications

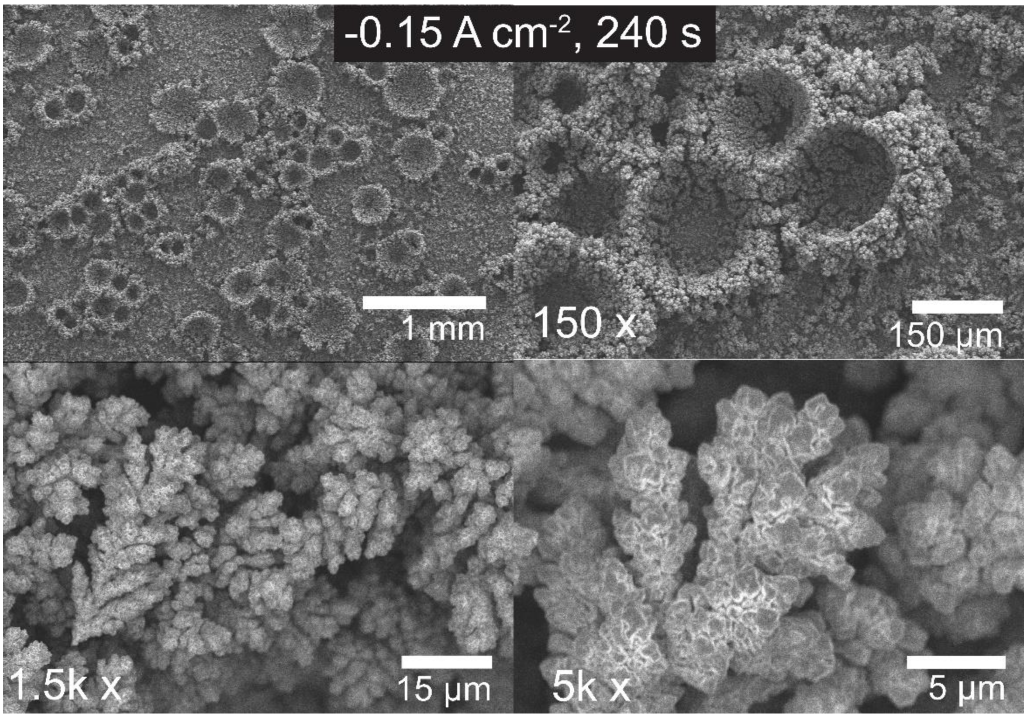

Figure A. 2 Surface morphology of dendritic porous Cu deposited at -0.15 A cm-2 for 240 s with different magnifications

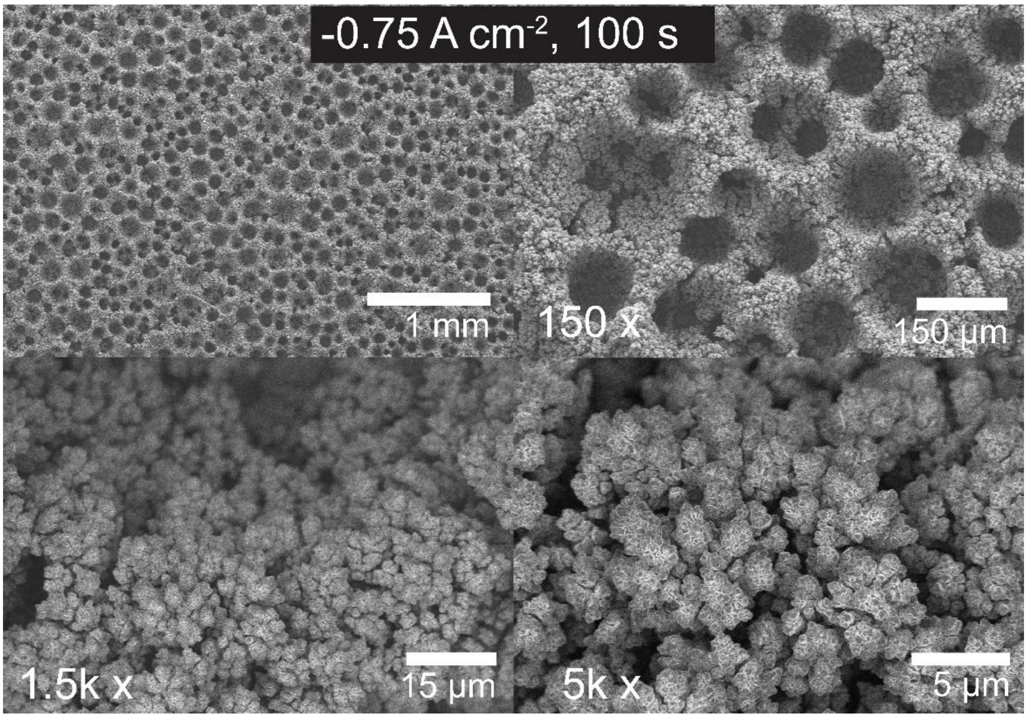

Figure A. 3 Surface morphology of dendritic porous Cu deposited at -0.75 A cm-2 for 100 s with different magnifications

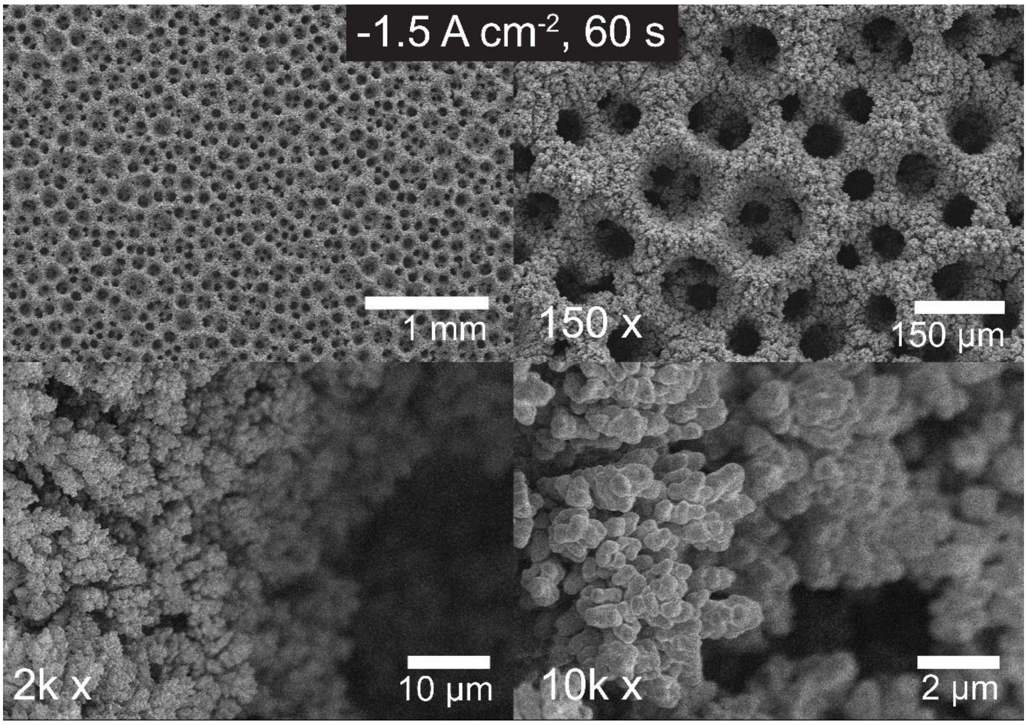

Figure A. 4 Surface morphology of dendritic porous Cu deposited at -1.5 A cm-2 for 60 s with different magnifications

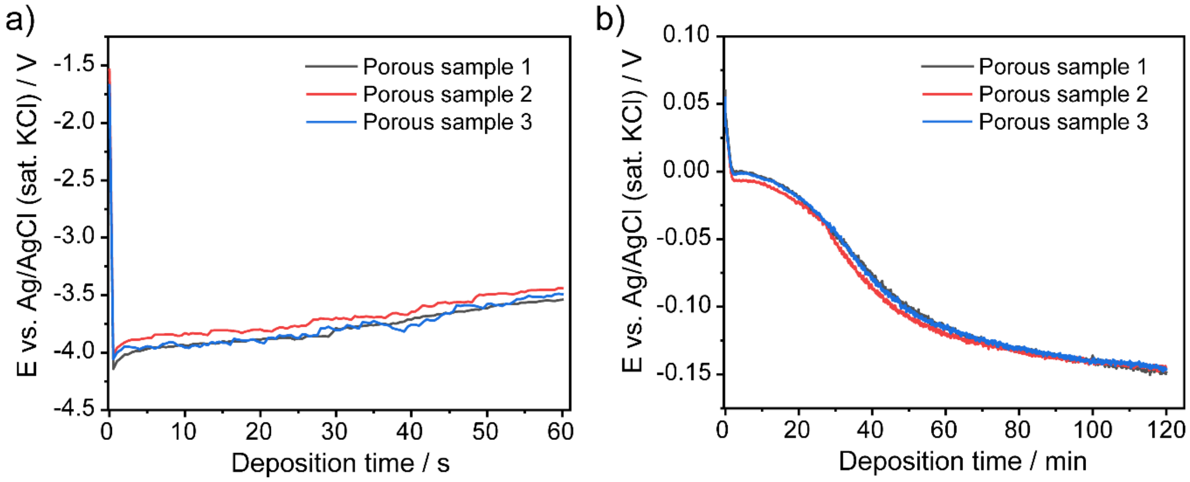

Figure A. 5 Galvanostatic chronopotentiometry curve of a) electrodeposited porous Cu at -1.5 A cm^{-2} and b) reinforcement procedure with -20 mA cm^{-2}. The three samples were used to analyze the reproducibility of the experiment.

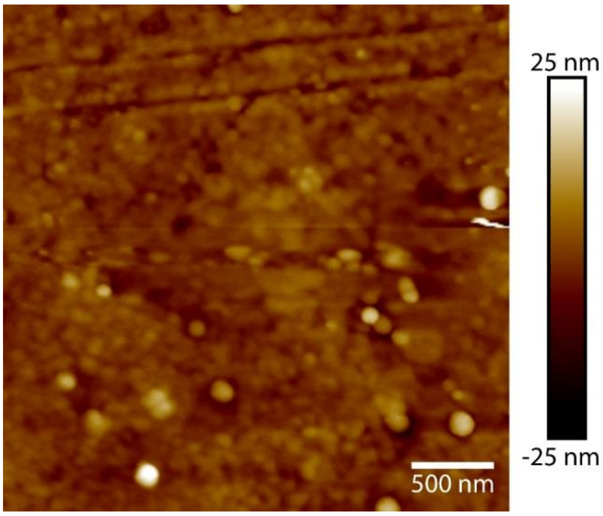

Figure A. 6 Height topography of the electropolished flat Cu substrate with a root-mean-squared roughness, Rq, of ~3 nm

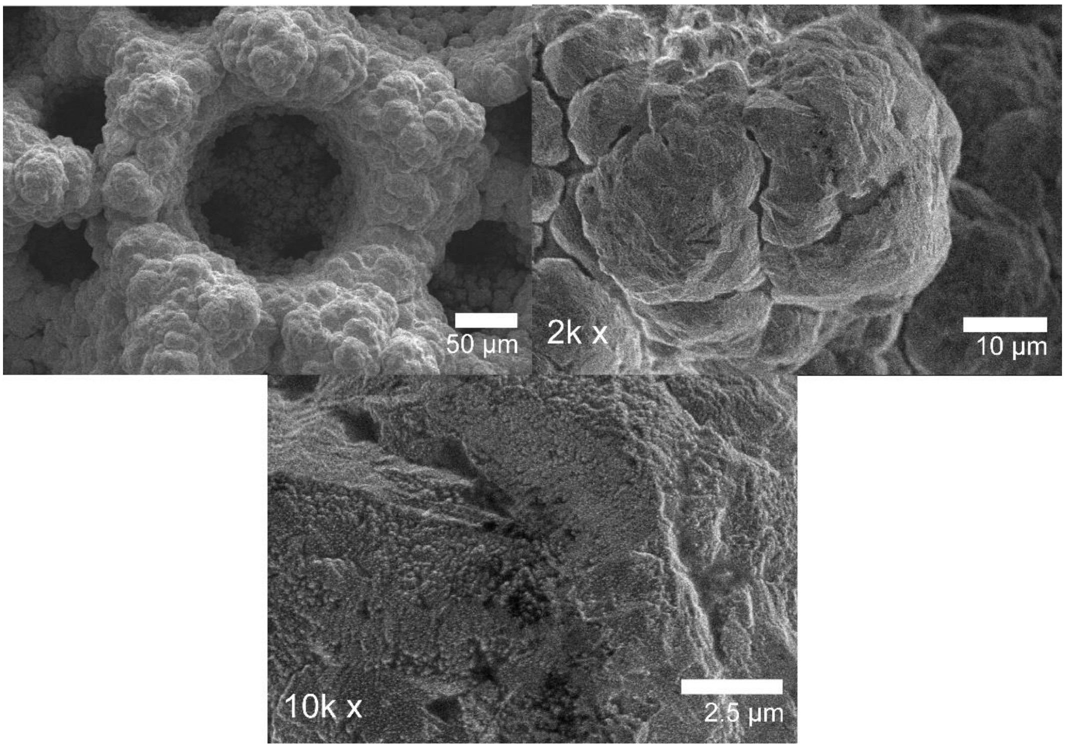

Figure A. 7 Surface morphology of reinforced porous Cu electrodeposited at -1.5 A cm^{-2} for 60 s and undergo reinforcement procedure at -20 mA cm^{-2} for 120 min. No Cu_2O crystals are presence, and the surface is relatively smooth.

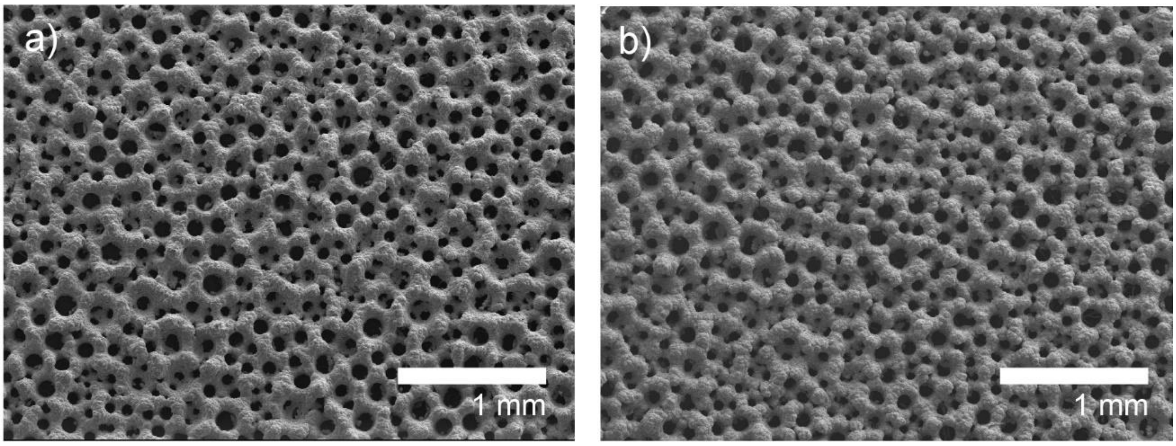

Figure A. 8 Morphological images of two free-standing porous Cu_2O samples electrodeposited at -1.5 A cm^{-2} for 60 sec and reinforced with another electrodeposition process at -20 mA cm^{-2} for 120 min.

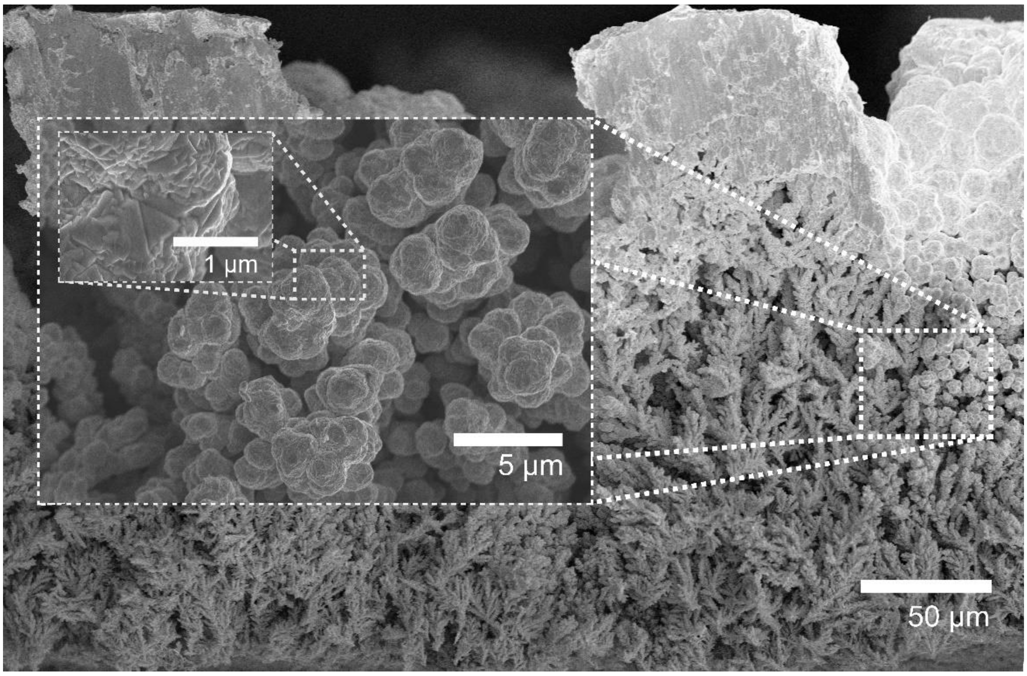

Figure A. 9 Cross-sectional analysis of reinforced porous Cu sample coated with Cu_2O film that was electrodeposited for 5 min deposition time. Cu_2O crystals can be observed growing on the Cu dendrites at the middle region of the samples.

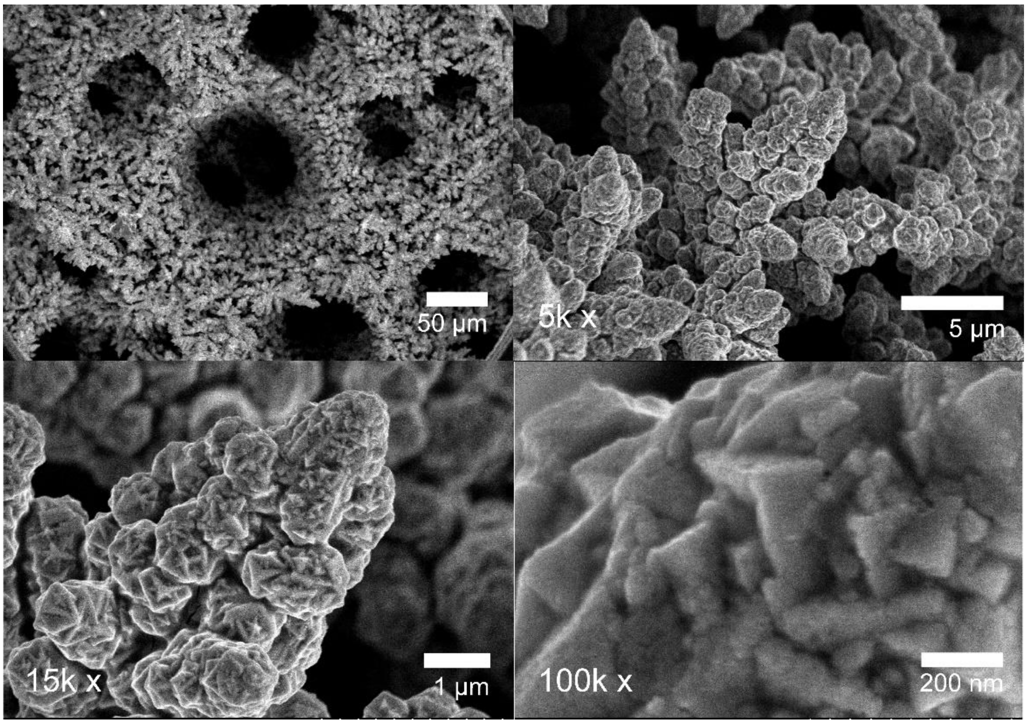

Figure A. 10 Morphological analysis of Cu_2O film on dendritic porous Cu with different magnifications. The Cu_2O was electrodeposited at -0.4 V vs. Ag/AgCl (sat. KCl) for 20 min.

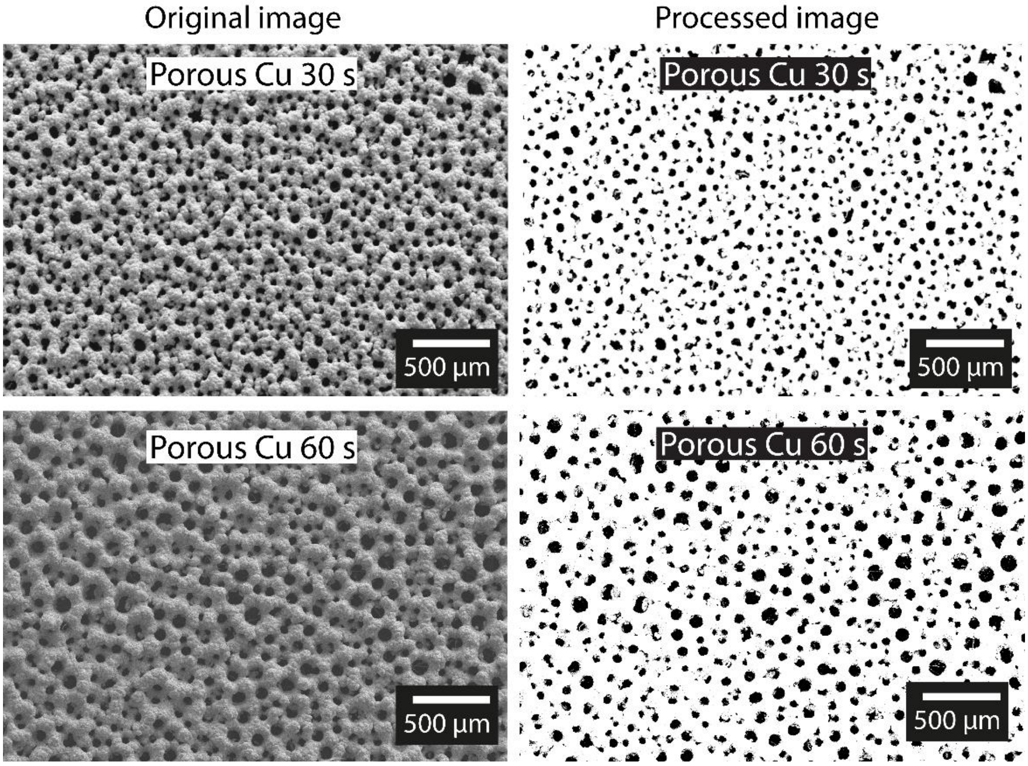

Figure A. 11 Pore analysis by using ImageJ software. The black contrast in the processed image represents the pore holes and the white contrast belongs to the pore walls.

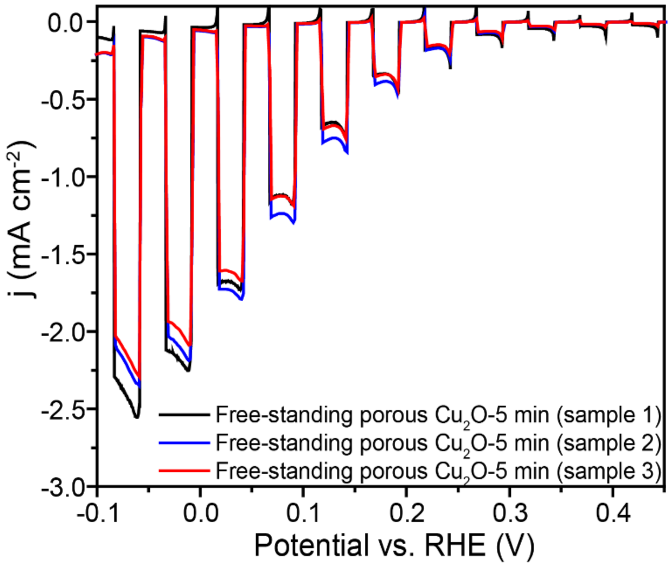

Figure A. 12 Linear sweep voltammogram of electrodeposited Cu_2O film on three different free-standing porous Cu substrates synthesized with the same parameters (60-sec dendritic deposition and 120 min reinforcement procedure) in an aqueous electrolyte of 0.5 M Na_2SO_4 under chopped illumination

The reproducibility of the free-standing porous Cu_2O samples electrodeposited with 5 min deposition for the PEC water splitting performance can be observed in Figure A. 12 Linear sweep voltammogram of electrodeposited Cu_2O film on three different free-standing porous Cu substrates synthesized with the same parameters (60-sec dendritic deposition and 120 min reinforcement procedure) in an aqueous electrolyte of 0.5 M Na_2SO_4 under chopped illumination. At the potential of 0 V vs. RHE, the current densities of the three samples are -2.2, -2.22, and -2.25 mA cm^{-2} for sample 3, sample 2, and sample 1, respectively. The small variation from the current densities shows that the samples can be easily reproduced.

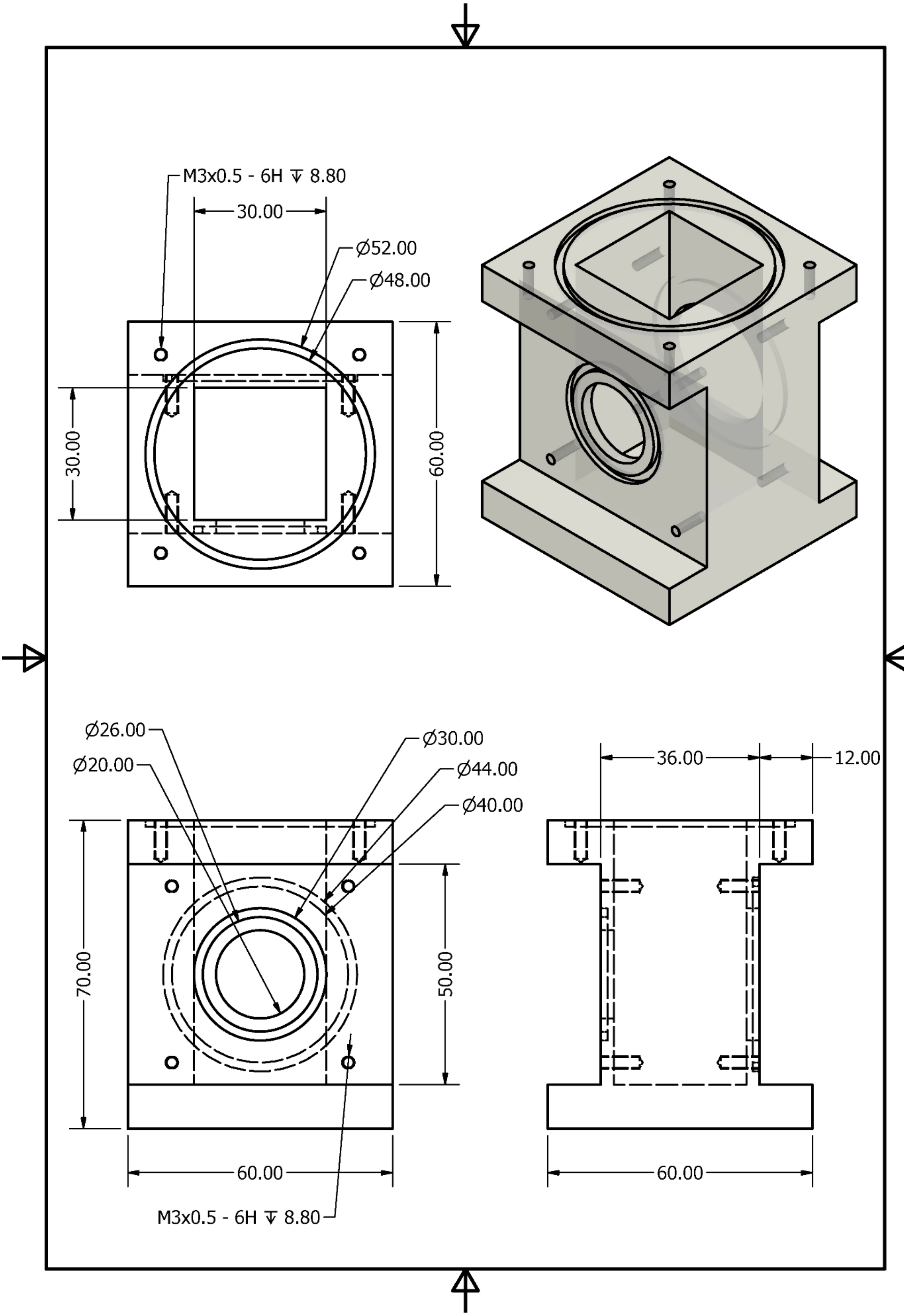
M3x0.5 - 6H ↧ 8.80
30.00
Ø52.00
Ø48.00
30.00
60.00
Ø26.00
Ø20.00
Ø30.00
Ø44.00
Ø40.00
36.00
12.00
70.00
50.00
60.00
60.00
M3x0.5 - 6H ↧ 8.80

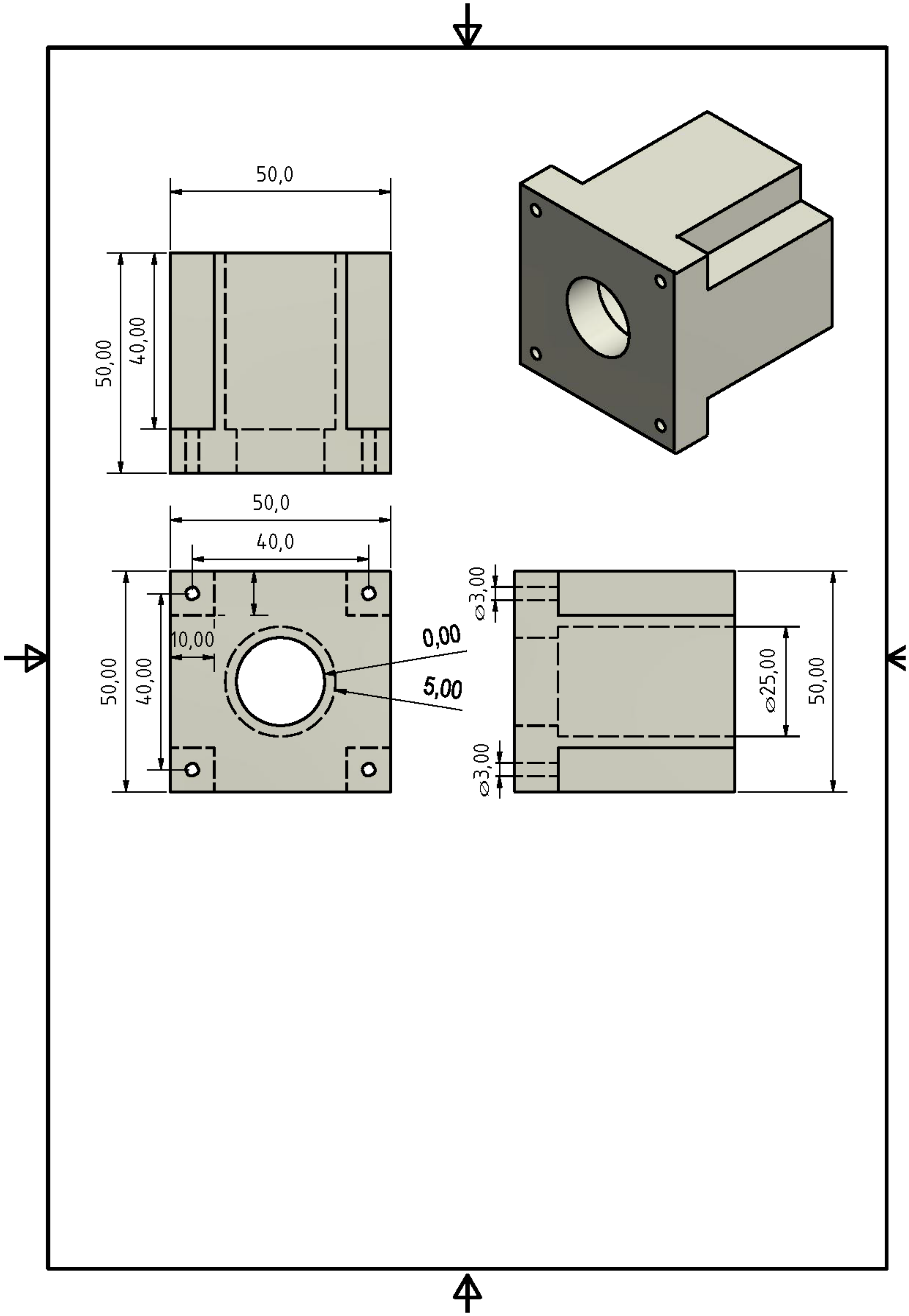
50,0
50,00
40,00
50,0
40,0
10,00
0,00
5,00
⌀3,00
⌀25,00
50,00
⌀3,00

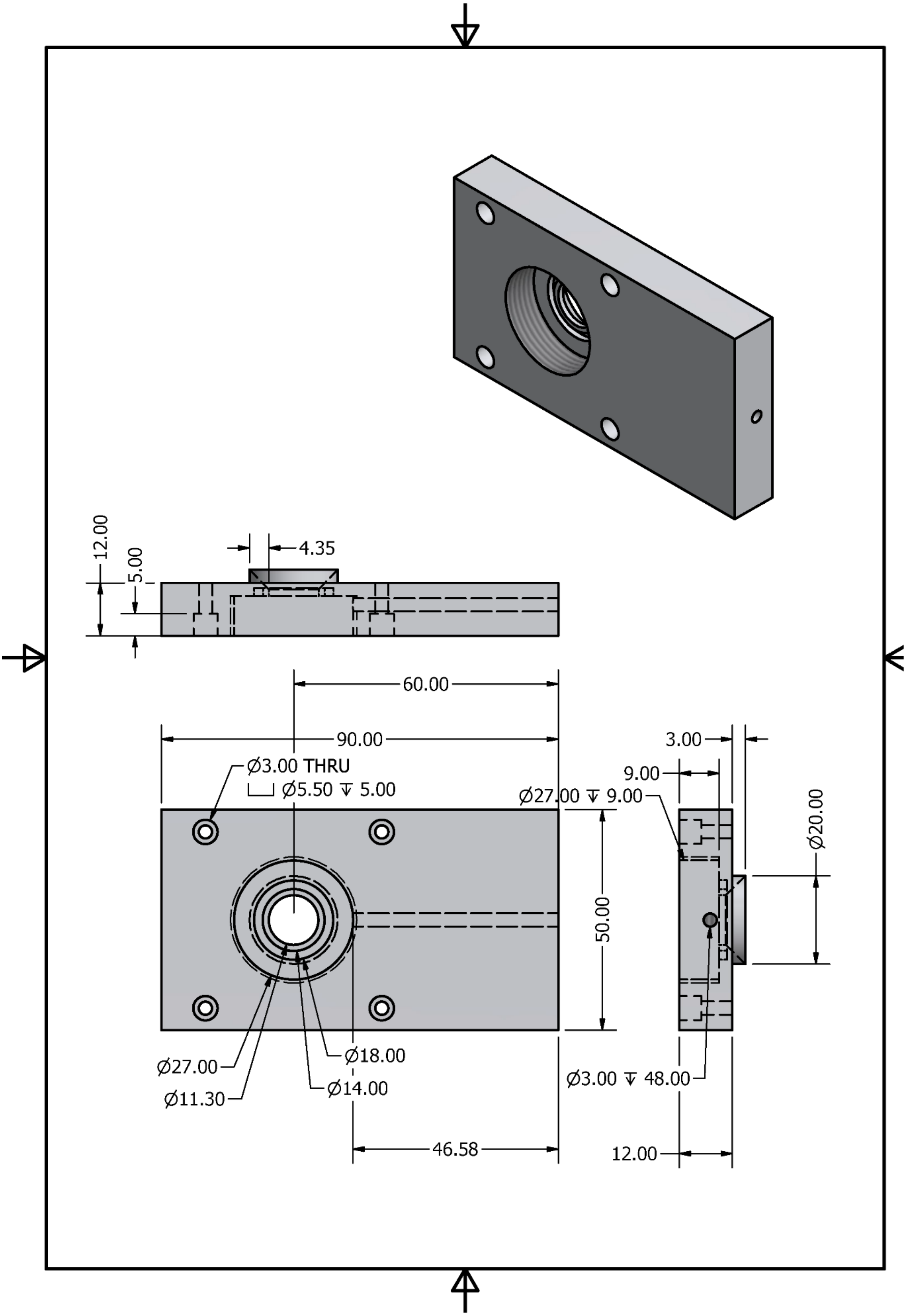

4.35
12.00
5.00
60.00
90.00
Ø3.00 THRU
⌴ Ø5.50 ↧ 5.00
Ø27.00 ↧ 9.00
50.00
3.00
9.00
Ø20.00
Ø27.00
Ø11.30
Ø18.00
Ø14.00
Ø3.00 ↧ 48.00
46.58
12.00

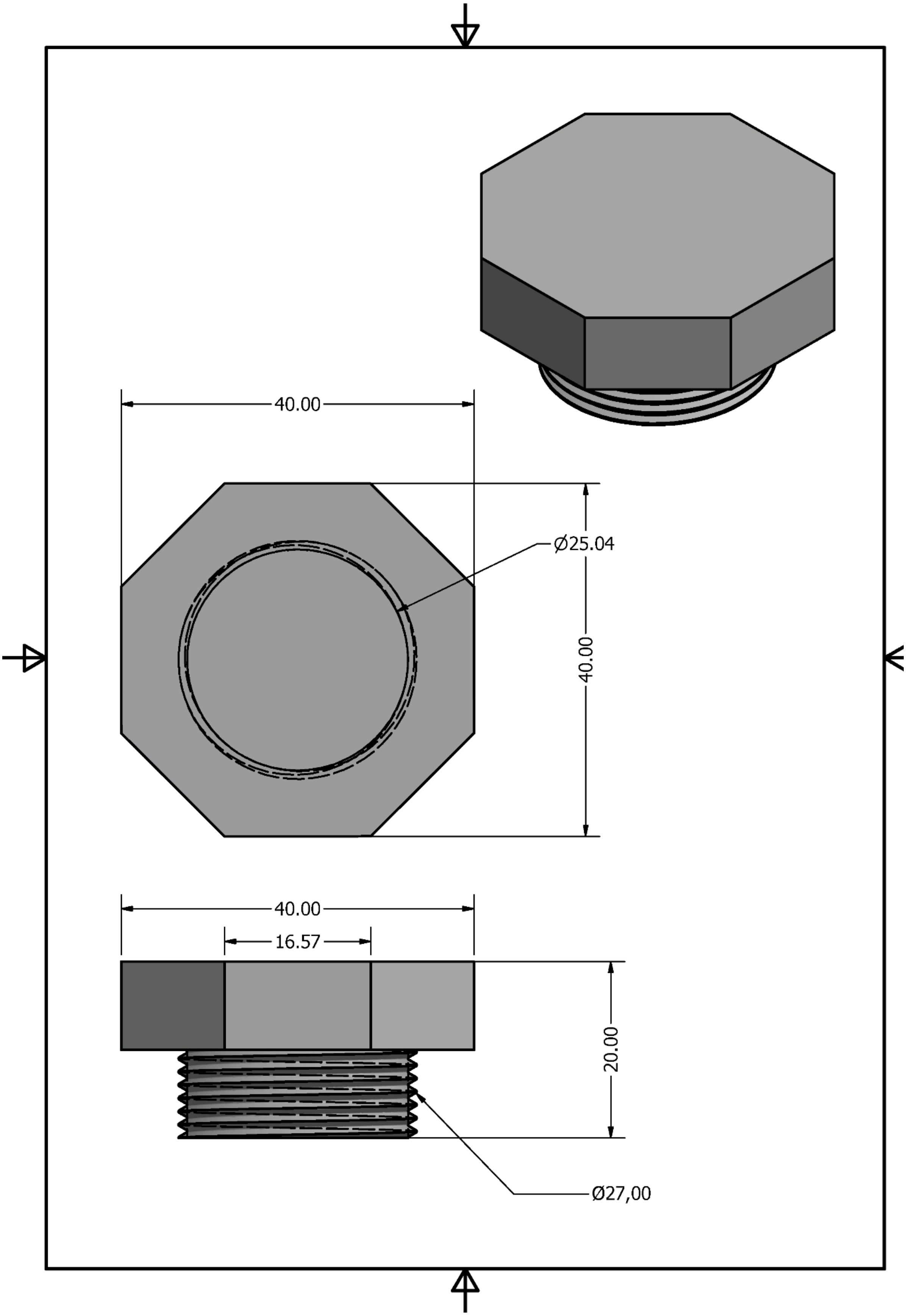
40.00
Ø25.04
40.00
40.00
16.57
20.00
Ø27,00

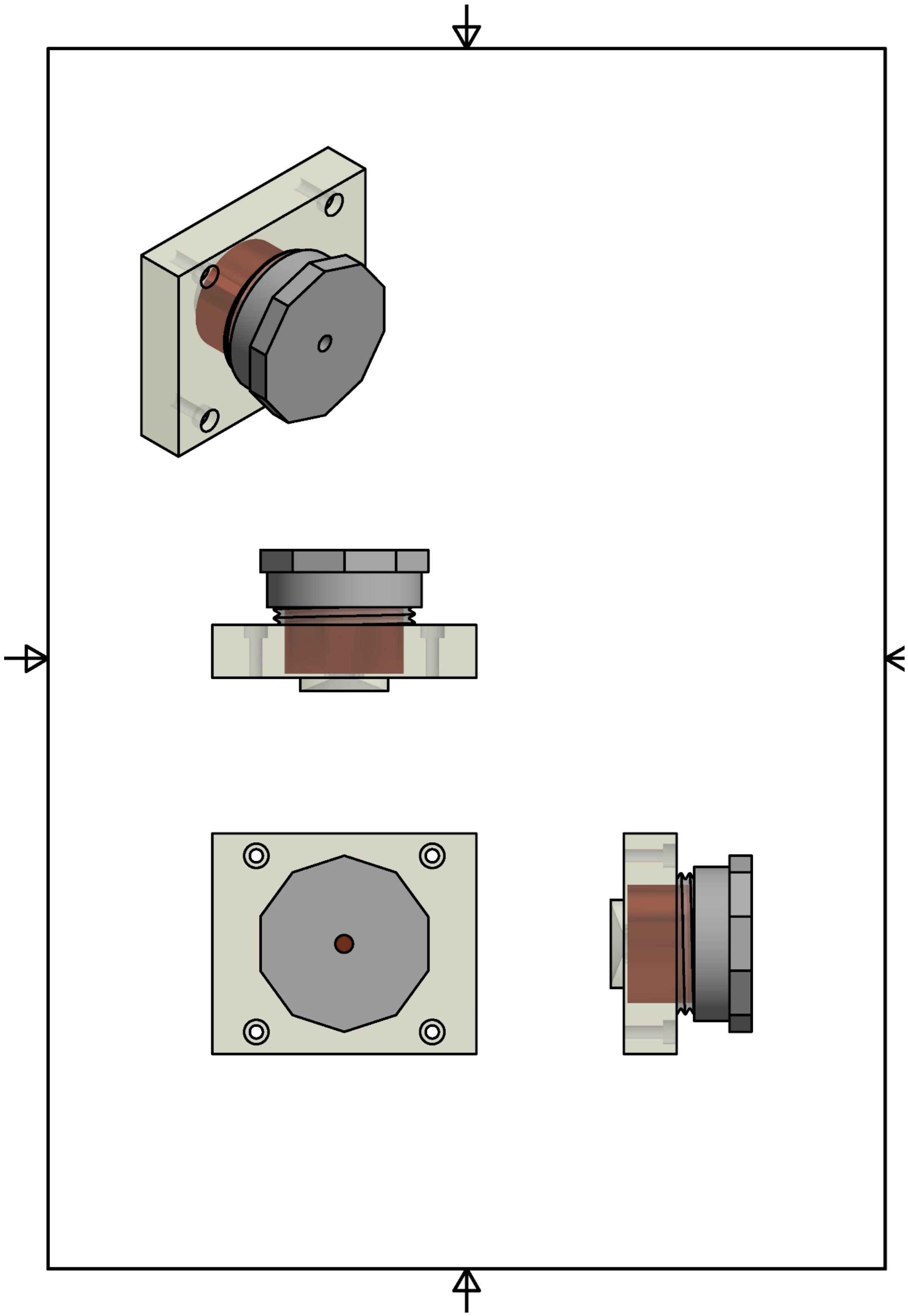

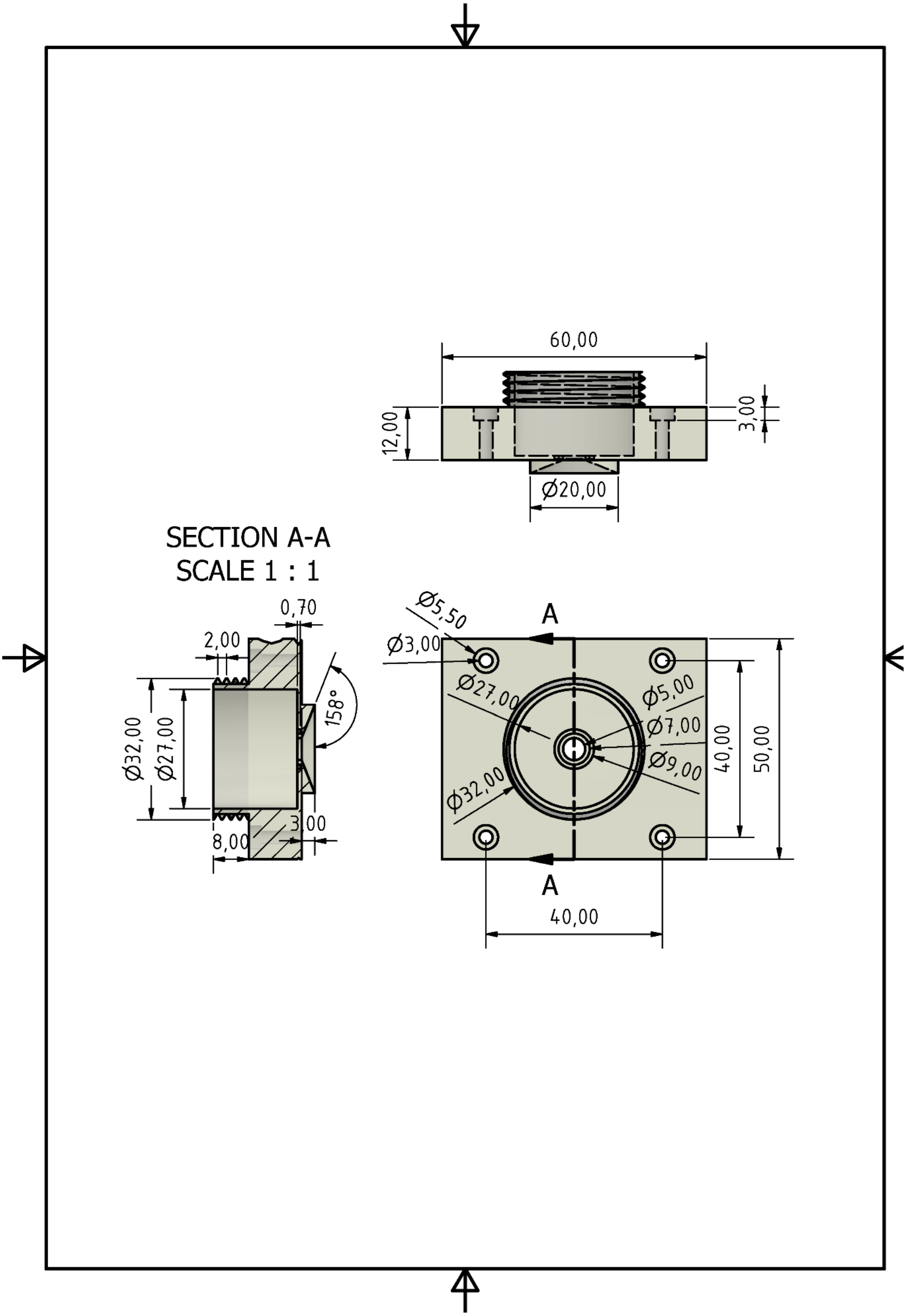
60,00
3,00
12,00
Ø20,00
SECTION A-A
SCALE 1 : 1
0,70
2,00
158°
Ø32,00
Ø27,00
3,00
8,00
Ø5,50
Ø3,00
A
Ø27,00
Ø5,00
Ø7,00
Ø9,00
Ø32,00
40,00
50,00
A
40,00

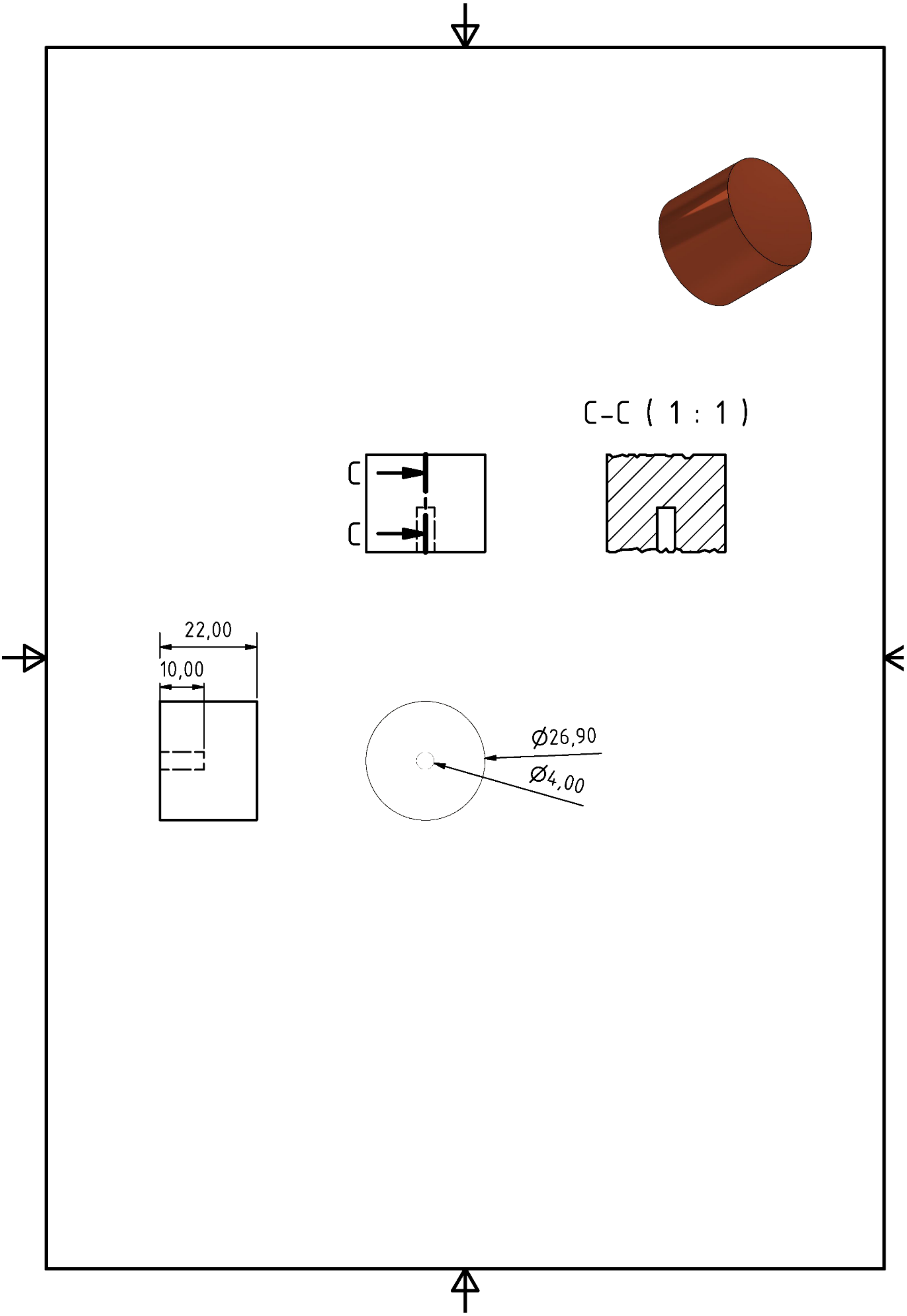
C-C (1 : 1)
C
C
22,00
10,00
Ø26,90
Ø4,00

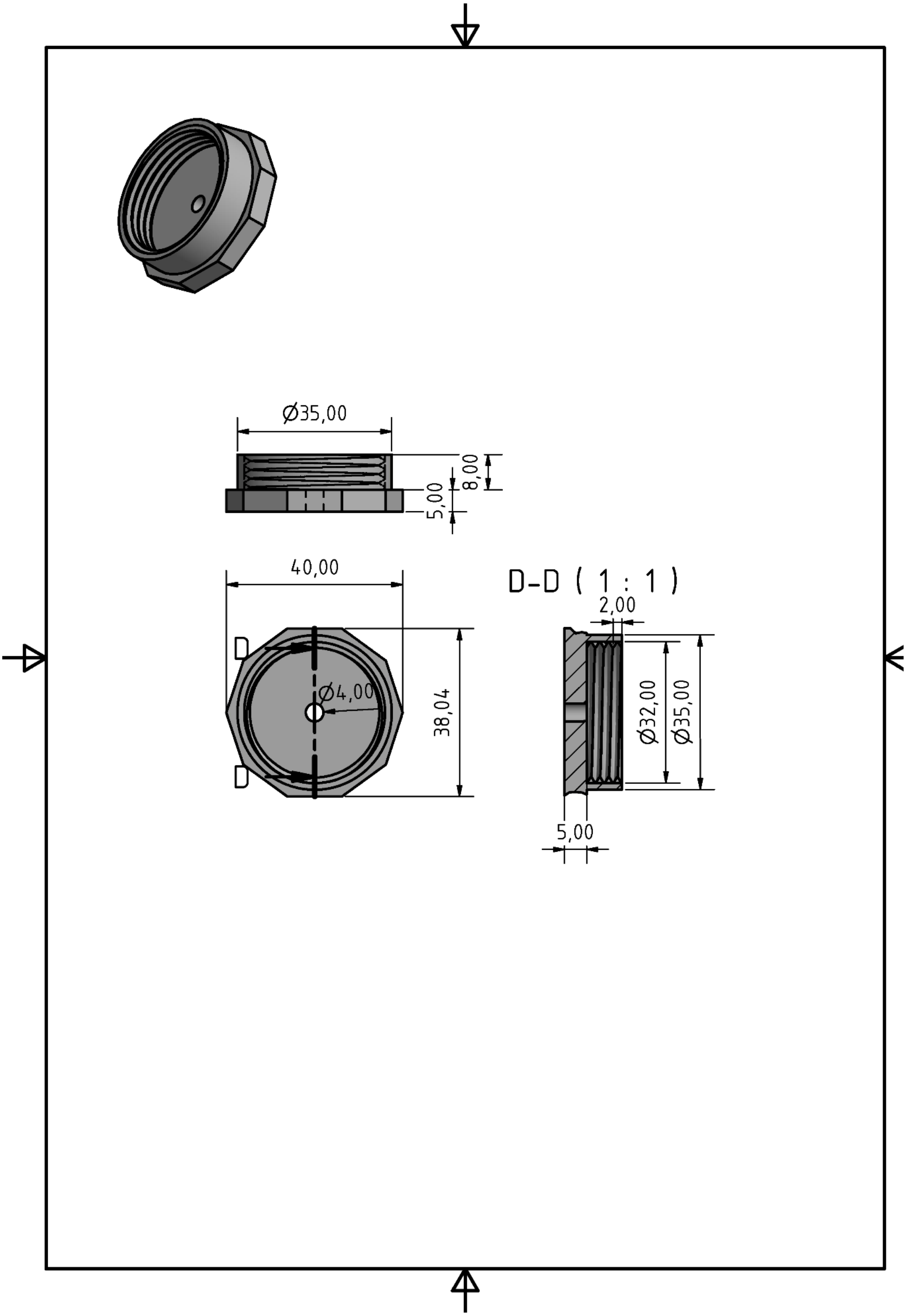
Ø35,00
8,00
5,00
40,00
D
D
Ø4,00
38,04
D-D (1 : 1)
2,00
Ø32,00
Ø35,00
5,00